



**HAL**  
open science

# Experimental and numerical study of blood flow in cerebral aneurysms treated with endovascular coils

Julia Romero Bhathal

► **To cite this version:**

Julia Romero Bhathal. Experimental and numerical study of blood flow in cerebral aneurysms treated with endovascular coils. Other [cond-mat.other]. Université Grenoble Alpes [2020-..], 2022. English. NNT : 2022GRALI028 . tel-03685280

**HAL Id: tel-03685280**

**<https://theses.hal.science/tel-03685280v1>**

Submitted on 2 Jun 2022

**HAL** is a multi-disciplinary open access archive for the deposit and dissemination of scientific research documents, whether they are published or not. The documents may come from teaching and research institutions in France or abroad, or from public or private research centers.

L'archive ouverte pluridisciplinaire **HAL**, est destinée au dépôt et à la diffusion de documents scientifiques de niveau recherche, publiés ou non, émanant des établissements d'enseignement et de recherche français ou étrangers, des laboratoires publics ou privés.

## THÈSE

Pour obtenir le grade de

### DOCTEUR DE L'UNIVERSITÉ GRENOBLE ALPES

Spécialité : 2MGE : Matériaux, Mécanique, Génie civil,  
Electrochimie

Arrêté ministériel : 25 mai 2016

Présentée par

**Julia ROMERO BHATHAL**

Thèse dirigée par **Christian Geindreau**, Université Grenoble Alpes,  
et codirigée par **Alberto Aliseda**, Université de Washington

préparée au sein du **Laboratoire 3SR (Grenoble)**, et à l'**Université de Washington (Seattle)**  
dans l'**École Doctorale I-MEP2 - Ingénierie - Matériaux, Mécanique, Environnement, Energétique, Procédés, Production**

### **Étude numérique et expérimentale du flux sanguin dans des anévrismes cérébraux après déploiement de coils**

### **Experimental and numerical study of blood flow in cerebral aneurysms treated with endovascular coils**

Thèse soutenue publiquement le **23 mars 2022**,  
devant le jury composé de :

**Monsieur Franck Nicoud**

Professeur à l'Université de Montpellier, Rapporteur

**Monsieur David Steinman**

Professeur à l'Université de Toronto, Rapporteur

**Madame Sylvie Lorthois**

Directeur de recherche à l'Institut de Mécanique des Fluides de Toulouse,  
Présidente

**Monsieur Nicolas Mordant**

Professeur à l'Université Grenoble Alpes, Examineur

**Madame Fanette Chassagne**

Maître de Conférence à l'École des mines de Saint-Etienne, Examinatrice

**Monsieur Christian Geindreau**

Professeur à l'Université Grenoble Alpes, Directeur de thèse

**Monsieur Alberto Aliseda**

Professeur Université de Washington, Directeur de thèse





# Remerciements

Je voudrais dans un premier temps remercier mes directeurs de thèse Christian Geindreau et Alberto Aliseda. Merci à eux pour leur disponibilité malgré la distance et pour leur soutien tout le long de cette thèse. Merci d'avoir créé une ambiance de travail très agréable et optimiste. J'ai beaucoup appris à vos côtés pendant ces trois dernières années.

Merci aux rapporteurs Franck Nicoud et David Steinman pour leur analyse approfondie du manuscrit ainsi que pour leur commentaires et suggestions. Merci aussi aux autres membres du jury qui ont participé à la soutenance pour leurs questions: Sylvie Lorthois, Fanette Chassagne et Nicolas Mordant.

Je tiens aussi à remercier les personnes impliquées dans le projet à différents niveaux. Merci à Mike Levitt et à l'ensemble de l'équipe de neurochirurgie pour nous avoir aidé et avoir répondu à toutes nos questions. Merci à Fanette et à Laurel pour m'avoir aidé dans la reconstruction des modèles, je vous suis énormément reconnaissante de m'avoir apporté votre expérience. Merci aussi à Faisal sans qui la partie expérimentale n'aurait pas vu le jour. Merci d'avoir partagé avec moi de longues heures de frustration mais aussi de bonheur, et surtout merci pour ta bonne humeur.

Merci à mes collègues du Fluids Lab, à mes collègues de 3SR, à mes amis et à ma famille. Ces années ont été un peu "spéciales" mais je me suis sentie soutenue et vous m'aurez même convaincue que j'étais capable de mener à bien cette thèse! Je suis très heureuse de vous avoir.



# Résumé

Une des complications fréquentes des anévrismes cérébraux après traitement par déploiement de coils est la recanalisation. Etudier l'hémodynamique dans les anévrismes traités avec des coils et définir les paramètres liés à la recanalisation peut permettre de prévenir la rupture de l'anévrisme. C'est dans ce but que des modèles numériques ont été développés, comme le « coil-resolved model » à l'Université de Washington. Ce modèle utilise la géométrie complète des coils pour reproduire un modèle d'anévrisme traité bio-fidèle. Néanmoins, en raison de l'opacité des coils, le processus pour recréer la géométrie des coils est très complexe, et le temps de calcul est très long. Modéliser le flux sanguin dans les anévrismes avec coils avec un modèle poreux permettrait de résoudre ce problème. Dans les études précédentes, les modèles poreux développés ne prennent pas en compte la distribution hétérogène de la porosité des coils et les résultats montrent que ces modèles ne peuvent pas être considérés comme bio-fidèles. En effet, dans ces études, la perméabilité et le facteur d'inertie sont estimés uniquement à partir de la porosité moyenne. Par conséquent, l'objectif de ce travail est de développer un modèle poreux bio-fidèle et qui peut être utilisé pour évaluer l'efficacité du traitement avant sa mise en oeuvre. Afin d'atteindre cet objectif, nous avons tout d'abord créé un dispositif expérimental innovant pour étudier le temps de séjour dans les anévrismes avec coils en utilisant la PLIF (planar laser-induced fluorescence). Les résultats de cette étude expérimentale ont été utilisés pour valider le modèle « coil-resolved ». Pour cela, nous avons comparé le temps de séjour mesuré expérimentalement et le temps de séjour obtenu avec des simulations avec un scalaire passif (modèle coil-resolved). Cette comparaison a montré que le modèle « coil-resolved » peut être considéré comme bio-fidèle. Il a été, par la suite, utilisé pour valider les modèles poreux. Afin d'améliorer les modèles poreux, nous avons dans un second temps caractérisé la distribution de porosité des coils en utilisant des images de huit anévrismes fantômes traités avec des coils. Ces modèles physiques ont été scannés à haute résolution. Les résultats de cette analyse montrent que la distribution de porosité est très hétérogène mais présente la même tendance pour tous les patients : la porosité est très élevée près de la paroi de l'anévrisme et est homogène au centre. Ces gradients de porosité ne sont donc pas négligeables et doivent être inclus dans la définition du modèle poreux. Les images 3D ont également été utilisées pour calculer la perméabilité et le facteur d'inertie des coils. Sur la base de ces résultats, nous avons proposé deux modèles poreux. Ces modèles sont homogènes isotropes et prennent en compte la distribution hétérogène de la porosité dans la définition de la perméabilité et du facteur d'inertie : le « porous crown model » et le « bilinear model ». Les deux modèles reposent sur l'hypothèse selon laquelle le flux sanguin s'effectue principalement parallèlement à la paroi de l'anévrisme (selon des couronnes). Cependant, le « porous crown model

» nécessite de connaître la géométrie des coils pour évaluer la perméabilité et le facteur d'inertie. Le « bilinear model » ne nécessite que la géométrie de l'anévrisme, la porosité cible par le chirurgien, et l'approximation bilinéaire du profil de porosité. Ces deux modèles ont été validés numériquement avec des conditions aux limites spécifiques à chaque patient. Les résultats montrent que les deux modèles sont précis, et en particulier que le « bilinear model » pourrait être utilisé dans l'avenir pour évaluer l'efficacité du traitement dans des conditions patient-spécifiques avant sa mise œuvre.

# Abstract

Recanalization is a common complication after treating cerebral aneurysms with endovascular coiling. Studying hemodynamics in coiled aneurysms and relating them with recanalization can help in preventing aneurysm rupture. Numerical models, such as the University of Washington's coil-resolved model, have been developed to simulate this problem. Nevertheless, due to the radio-opacity of the coils, the process to recreate the geometry of the coils is very complex, and due to the small scales involved, the computational requirements are high. Modeling blood flow in aneurysms with coils using a porous model would avoid these shortcomings. In previous studies, the porous models developed did not include the heterogeneous distribution of the porosity of the coils and weren't accurate. Indeed, the permeability and the inertial factor were only based on the mean porosity. Therefore, the objective of this work was to develop a porous model that would capture the anatomy and physiology, and that could be used for the prediction of treatment outcomes. First, we created an innovative experimental setup to study residence time in coiled aneurysms using Planar Laser-Induced Fluorescence. The results of this experimental study were used to validate the coil-resolved model. We compared the residence time measured experimentally and that obtained with passive scalar transport simulations with the coil-resolved model. This comparison showed that the coils resolved model is accurate within certain limits. This model was used to validate the porous models developed later. Second, to improve porous models, we first characterized the porosity distribution of the coils using images of eight phantom aneurysms treated with coils. These physical models were scanned at high resolution with synchrotron microtomography. The porosity distribution was highly heterogeneous but presented a pattern: the porosity is very high near the wall and homogeneous in the bulk. These porosity gradients are not negligible and need to be included in the definition of the porous model. The 3D images were also used to compute the permeability and the inertial factor of the coils. Based on these results, we then proposed two homogeneous isotropic porous models that took into account the heterogeneity of the porosity distribution in the definitions of permeability and inertial factor: the crown porous model and the bilinear model. Both models shared the hypothesis that blood flows mainly tangential to the aneurysm sac wall. However, the crown porous model needs the geometry of the coils to calculate the permeability and inertial factor of these spherical crowns, while the bilinear model only requires the geometry of the aneurysm, the target porosity elected by the surgeon in the treatment, and a bilinear approximation of the porosity profile. These two models were validated numerically with patient-specific boundary conditions. The results show that both models are accurate and, in particular, the bilinear model could be used in the future to predict

patient-specific treatment outcomes in the neuro-suite.

---

# Contents

<b>1</b>	<b>Introduction</b>	<b>2</b>
1.1	Introduction . . . . .	2
1.2	Objectives . . . . .	4
1.3	Organisation of the manuscript . . . . .	4
<b>2</b>	<b>State of the art</b>	<b>8</b>
2.1	Cerebral aneurysm treated with coil embolization . . . . .	9
2.1.1	Cerebral aneurysm and clinical management . . . . .	9
2.1.2	Coil embolization . . . . .	14
2.2	Hemodynamics in aneurysm with coils . . . . .	17
2.2.1	Modeling blood flow in cerebral aneurysm . . . . .	17
2.2.2	Modeling blood flow in coiled aneurysm : the coil-resolved model	18
2.2.3	Modeling blood flow in coiled aneurysm : the porous model .	24
2.3	Concluding remarks . . . . .	40
<b>3</b>	<b>Residence time analysis on cerebral aneurysms treated with coils using planar-laser-induced fluorescence and computational fluid dynamics</b>	<b>42</b>
3.1	Introduction . . . . .	43
3.2	Methods . . . . .	44
3.2.1	Model creation . . . . .	44
3.2.2	Planar-laser-induced fluorescence . . . . .	46
3.2.3	Computational Fluid Dynamics . . . . .	49
3.3	Results . . . . .	52
3.3.1	PLIF results . . . . .	52
3.3.2	Comparison with coil-resolved simulations results . . . . .	56
3.4	Discussion . . . . .	59

3.5	Conclusion . . . . .	61
<b>4</b>	<b>Modeling flow in cerebral aneurysm after coils embolization treatment: A realistic patient-specific porous model approach</b>	<b>64</b>
4.1	Introduction . . . . .	65
4.2	Method . . . . .	67
4.2.1	Image acquisition . . . . .	67
4.2.2	Porosity distribution . . . . .	69
4.2.3	Flow through the porous medium . . . . .	71
4.2.4	CFD validation . . . . .	72
4.3	Results . . . . .	76
4.3.1	Porosity distribution . . . . .	76
4.3.2	Permeability and inertial factor . . . . .	77
4.3.3	CFD simulations . . . . .	80
4.4	Discussion . . . . .	83
4.5	Conclusion . . . . .	85
<b>5</b>	<b>Towards prediction of blood flow in coiled aneurysms before treatment</b>	<b>86</b>
5.1	Introduction . . . . .	87
5.2	Methods . . . . .	89
5.2.1	Model creation . . . . .	89
5.2.2	Definition of the porous model . . . . .	90
5.2.3	Computational fluid dynamics: comparison of the coil-resolved and porous medium models . . . . .	97
5.3	Results . . . . .	105
5.4	Discussion . . . . .	111
5.5	Conclusion . . . . .	115
<b>6</b>	<b>Conclusion and perspectives</b>	<b>116</b>
6.1	Main results . . . . .	117
6.2	Perspectives . . . . .	119
	<b>Bibliography</b>	<b>122</b>

---

## List of Figures

2.1	Saccular (left) and fusiform (right) aneurysms. . . . .	10
2.2	Circle of Willis, from The Children’s hospital of Wisconsin [ <i>Chiu et al.</i> , 2019] . . . . .	10
2.3	A) Healthy vessel wall. B) Arterial wall histology following aneurysm initiation and growth: disruption of the IEL, thinning of the medial layer. Figure is taken from <i>Etminan and Rinkel</i> [2016] with the adaptation made by Barbour’s work [ <i>Barbour</i> , 2018]. . . . .	11
2.4	Treatment methods for cerebral aneurysm: a) Endovascular coiling b) Surgical clipping c) Stent-assisted coiling d) Flow diversion. Source: [ <i>Perrone et al.</i> , 2015] . . . . .	14
2.5	Illustration of the coils being deployed (up) and set (down) in a cerebral aneurysm. Source: <i>Brisman et al.</i> [2006]. . . . .	15
2.6	A) Untreated internal carotid artery (ICA), B) Coil mass deployed in the cerebral aneurysm, C) Total occlusion. Source : <i>Seibert et al.</i> [2011]. . . . .	15
2.7	Sampler Doppler velocity from ComboWire (left). Phase average velocity (top) and pressure (bottom), the dotted lines present two standard deviation. The source is <i>Barbour</i> [2018] . . . . .	21
2.8	Summary of the reconstruction of the vessel surface, from left to right: raw DICOM images, initial surface segmentation, cleaned/clipped surface. Source Barbour’s work [ <i>Barbour</i> , 2018] . . . . .	21
2.9	Full process of the coil-resolved model: From the data acquisition, to the computational model generation and finally the computational simulation. . . . .	25
2.10	Scheme of fluid flow through a porous media up the microscopic scale . . . . .	26
2.11	Schematic of separation of scale and the representative elementary volume (REV) . . . . .	28

2.12	Normalized intrinsic permeability of an array of parallel cylinders in the (a) transverse and (b) longitudinal directions, i.e. $\mathcal{K}/R_s^2$ , as a function of the porosity: the self-consistent estimates P (continuous line) and V (dotted line) are compared with with the numerical results obtained by finite element simulations on square (square) and triangular (black triangle) lattices of parallel cylinders. [Auriault et al., 2009]. . . . .	30
2.13	Comparison between the present numerical and experimental results for Forchheimer coefficient (F) with experimental and numerical data of others. The figure shows the evolution of the Forchheimer coefficient (F) with the porosity ( $\epsilon$ ). Source: Tamayol et al. [2012]. . . . .	31
2.14	Schematic representation of the coupling methods: (left) The two domains approach with interface boundary conditions, (right) the single domain approach with a transition zone for the physical parameters. Source: Rybak [Rybak, 2016] . . . . .	33
2.15	Left: Idealized in aneurysm models with diameters varying from 4 to 8mm and treated with different coils (Orbit Codman Neurovascular, Cosmos and Hypersoft Microvention Terumo, Axium Bare and PGLA Covidien Medtronic, and Penumbra Coil 400).Right: Permeameter used in the experiment. Source: C.Sadasivan et al. [2018]. . . . .	35
2.16	Up: Flow loop to measure the permeability. Down: coils deployed in hte sample chamber. Source: Muschenborn et al. [2013] . . . . .	36
2.17	Measured permeability in embolic coils (MECs) compared to the calculated with Kozeny’s model in Kakalis et al. [2008]. Source: Muschenborn et al. [2013] . . . . .	36
2.18	Levitt et al results of streamlines at systole: comparison between porous model and coil-resolved model for two patients [Levitt et al., 2016] . . . .	39
2.19	Yadollahi-Farsani et al porous map at different resolutions for 3 patients [Yadollahi-Farsani et al., 2019]. The first column presents the coil-resolved model. The three right colums present the porous map at different resolution with the number on each column being the number of hexahedra in each axial direction. . . . .	40
3.1	Main steps of the image acquisition: from the angiographic image on the top, to the coils ESRF scans. . . . .	45
3.2	3D models of the patients after coils reposition. . . . .	46
3.3	Schematics of the optical set up and the flow loop . . . . .	48
3.4	Silicone model patient G. . . . .	48

3.5	Patient H image treatment: on the top, the 3D model of Patient H with the green plane that is equal to the images obtained through PLIF. On the bottom left the images (raw and binary) before starting the pulsatile pump, when the aneurysm is filled with rhodamine B ( $c=100\%$ ). On the middle, at $c=25\%$ , and on the right (raw and binary) at the end of washout ( $c=0\%$ ). . . . .	50
3.6	Evolution of the concentration during time for each patient over three run for the PLIF analysis. . . . .	53
3.7	3D numerical model vs image obtained through PLIF technique for each patient. In each numerical model, the green plane shows region observed in the images obtained through PLIF techniques, which correspond to the area illuminated with the laser. The PLIF image used is when the rhodamine concentration in the aneurysm is at 100%. The 3D models are positioned as they were in front of the camera. . . . .	54
3.8	Evolution of the concentration over time normalized by the aneurysm volume for each patient. Patient G was excluded from this figure as the high variations of the concentration over time made it impossible to compare with the other patients (Figure 3.6G). . . . .	55
3.9	Comparison between the CFD and the PLIF study: evolution of the concentration of rhodamine B for the CFD model in orange and the experimental model in blue over pushed volume normalized by the pore volume. The results are shown for each patient. For each patients two captions of the evolution of concentration over time are shown: at the beginning of the washout (1), and at the end of the three cardiac cycles (2). . . . .	58
4.1	Aneurysmal anatomy: Patient A (left) and B (right). The arrows present the direction of flow: blue is the inlet and red the outlet. $L$ is a characteristic length, defined as the length of the longest inertial axis (Table 4.1). . . . .	68
4.2	Main steps of the image acquisition: from the angiographic image on the left, to the positioning of the coils in the aneurysm. The results of this process is shown for Patient A. . . . .	68
4.3	Definition of the porous medium for patient A: The aneurysm containing the exact coil geometry as obtained from synchrotron microtomography (top left). Cross-section of the aneurysm with coils (top right). Cube porosity map with the 2 cube sizes: $2d$ (middle left) and $4d$ (bottom left), and in red the centered cubes. The crown porosity model, with two different crown sizes $0.25d$ (middle right) and $1d$ (bottom right). The colors vary with the porosity, as seen in the color bar. . . . .	70

4.4	Modeling aneurysms with coils as a homogeneous porous media, demonstrating blood flow through the crown model: red arrow shows flow moving along the crowns and the blue arrow shows the blood flow perpendicular to the crowns. . . . .	75
4.5	Histogram of the porosity of the cubes for two sizes of cube's side: $2d$ (left) and $4d$ (right) for patient A. . . . .	77
4.6	Porosity along the crowns for the two patients studied (patient A in the left and patient B in the right). The x-axis represents the center point of the crown, with $x = 0$ mm being the aneurysm's wall. . . . .	78
4.7	Dimensionless permeability results versus porosity on each cube for a $4d$ cube size for patient A and B. The blue line and the red line represent the estimates (SCE) given by equations (4.2) and (4.3) respectively. . . . .	79
4.8	Figure (a) shows the evolution of the ratio between the mean velocity in the $x$ direction and the gradient of pressure for each cube with the pore Reynolds number for Patient A. Dashed lines represent the Darcy-Forchheimer equation (4.1) adjusted on the numerical results (symbols). Figure (b) shows, for Patients A and B, the evolution of the inertial factor with the porosity deduced from the computations on each cube. The continuous line represents the adjusted equation (4.4) . . . . .	80
4.9	(a, b): Porosity profiles for the two patients (Number of crowns = 16, crown's size = $0.25d$ ), corresponding permeability (c,d) and inertial factor (e,f) profiles given by equations (4.3) and (4.4) respectively. The bulk is separated from the crowns by a grey vertical dashed line. The horizontal dashed lines represent the permeability values $K_m$ , $K_{op}$ and $K_p$ ; and the inertial factor values $C_{2m}$ , $C_{2op}$ , $C_{2p}$ of the three different porous models. . . . .	81
5.1	3D models of the patients after coils positioning. For each patient, the longest side of the parent vessel is the inlet, and the shorter side the outlet. The number of outlets vary from one patient to the other depending on the original location of the aneurysm. . . . .	91
5.2	Porosity analysis process for patient A: from the 3D numerical model to the porosity profile. . . . .	92
5.3	Porosity along the crowns for eight patients. The x-axis represents the center point of the crown, with $x = 0$ mm being the aneurysm's wall. The four crown sizes are presented $0.25d$ , $0.5d$ , $1d$ and $2d$ . . . . .	93
5.4	Full process to build the bilinear porous model: from the data available in the neuro-suite to the numerical model. . . . .	98
5.5	Comparison between the aneurysm volume and the ellipsoid volume approximation for the eight patients. . . . .	98

5.6	Radial porosity profile for the eight patients. The porosity is measured along the crowns, when the crown size is 0.25d (d is the diameter of the coil). The bilinear porosity profiles for t= 0.5mm, t= 0.75 mm, t= 1 mm.	99
5.7	Permeability profile for each patient: crown and bilinear model. The equivalent permeability models are plotted in dotted line: mean ( $K_m$ ), optimal ( $K_{op}$ ), crowns ( $K_p$ ) and bilinear model ( $K_{bi}$ ).	100
5.8	Inertial factor profile for each patient: crown and bilinear model. The equivalent inertial models are plotted in dotted line: mean ( $C_{2m}$ ), optimal ( $C_{2op}$ ), crowns ( $C_{2p}$ ) and bilinear model ( $C_{2bi}$ ).	101
5.9	Percentage change for the mean velocities, the coil-resolved model is considered the gold standard. The error is defined as $(\langle \mathbf{u}_{coil-resolved} \rangle - \langle \mathbf{u}_{porous} \rangle) / \langle \mathbf{u}_{coil-resolved} \rangle \times 100$ .	108
5.10	Permeability and inertial factor comparison between the optimal values and the parallel and perpendicular flow for patients A to G. Patient H was excluded for visibility of the results.	109
5.11	Percentage of error mean velocities versus difference between bilinear model and optimal model (right), and the porous crown model and optimal model (left), for the permeability values for patients A to H.	110
6.1	Comparison between the process to create the coil-resolved model and the bilinear porous model. On the left, the full process of the coil-resolved model: from the data acquisition to the computational model generation and finally the computational simulation. In the right, the full process to the bilinear porous model.	119



### 1.1 Introduction

Cerebral aneurysms are deformations of the artery wall in the arteries located in the brain, and represent a common neurovascular disease impacting 1 to 5% of the adult population. The origin of this deformation is a combination of environmental factors and genetic predisposition. However, it is known that hemodynamics are linked with aneurysm growth. Cerebral aneurysms present a danger for the patient as some of them might rupture. Indeed, the wall of the aneurysm is thinner than the normal artery wall, and there is a risk of tearing leading to subarachnoid hemorrhage with very high mortality and morbidity for the patient.

There are different methods to treat cerebral aneurysms. Traditionally, it was done using the clipping technique, which consists of performing a craniotomy on the patient and placing a clip at the neck of the aneurysm, isolating it from the blood flow and avoiding rupture. While effective, this technique is very invasive, creating complications during the surgical procedure. Endovascular techniques are preferred nowadays, due to the effectiveness of the results and being less invasive. One of the techniques, that this thesis focuses on, is endovascular coiling, which consists of deploying a number of coils inside the aneurysmal sac. The blood flow in the aneurysm decreases due to the presence of the coils, leading to thrombus formation. The aneurysm is isolated from the blood flow stresses and the wall is protected, avoiding aneurysm rupture.

However, the treatment is not always effective. Indeed, there is a risk of recanalization when the thrombus formed does not fill the entire aneurysmal sac, which happens in around 20% of the cases. Recanalization can lead to rupture and internal hemorrhage. The packing density of the aneurysm is linked with the risk of recanalization. Increasing the number of coils increases the chances of complete thrombus formation. However, there is a limit in the packing density, around 30% of the aneurysmal volume filled with coils, and above that value, the coils might

interfere with blood flow in the parent vessel or damage the aneurysm wall. Even at a packing density of 30%, recanalization can still appear. Therefore, the ultimate goal of the research presented in this thesis is to determine the factors that promote recanalization and create a method to predict the treatment outcome for endovascular coiling of intracranial aneurysms.

Hemodynamics have been related to the growth and rupture of cerebral aneurysms in previous research, therefore there is an interest in defining hemodynamics factors related to recanalization. To achieve this, there is an interest in modeling blood flow in treated aneurysms and analyzing it through computational fluid dynamic techniques (CFD). However, this presents a difficulty because the geometry of the coils cannot be extracted from clinical imaging.

One of the possible solutions for this problem has been developed at the University of Washington. A methodology has been proposed to create a numerical model of the aneurysm treated with coils that mimics the actual deployed coils in the patient aneurysm: the coil-resolved model. This model consists in creating a phantom artery of the aneurysm from patient CT scans, treating it with actual coils, and scanning it via synchrotron microtomography at high-energy. The coil geometry is then recreated from those scans and included in the computational model of the flow in the patient-specific vasculature that includes the aneurysm. The coil-resolved model can be used to understand how the hemodynamics evolve after coil deployment, and also as the “gold standard” or “true” reference to validate other simpler numerical models. However, this model presents four main disadvantages: (i) it requires the geometry of the coils and, therefore, there is a complex process to create it and study the hemodynamics, (ii) it cannot be used for prediction before treatment, (iii) it cannot be implemented in a large cohort of patients, and (iv) is very expensive in computational resources. The coil-resolved model should be validated experimentally before being used as the “gold standard” for validation and verification of other models. This experimental validation is very challenging due to the opacity of the coils.

To study hemodynamics in treated aneurysms without requiring the geometry of the coils, one possible solution is to model the volume of the treated aneurysmal sac as a porous medium. Using this model, it is possible to analyze the velocities and other parameters in the treated aneurysms. The process to create the porous medium numerical model is much simpler than the coil-resolved, as it only requires the aneurysm anatomy. Having a faster process opens the door to model blood flow in treated aneurysm in large cohorts of patients. The flow in treated aneurysm modeled as a porous media is defined by Forchheimer’s law, which has two parameters to quantify the porous medium properties: permeability and inertial factor. The porous models developed up to date to model blood flow in treated aneurysms with coils are simplistic and have shown to not accurately reproducing the results from the

coil-resolved model. This is due to the simplification in defining the porous medium: defining the flow permeability and inertial factor as isotropic scalars, homogeneous in space. There is a need to improve the porous medium model, including the information available on the structure of the coils deployed in the aneurysm, to define the hemodynamics parameters that lead to recanalization and, thus, be able to predict endovascular coiling treatment.

## 1.2 Objectives

The main objective of this study is to develop a model to better reproduce blood flow in cerebral aneurysms treated with endovascular coils. This model should be accurate to the configuration of the coils inside the patient-specific aneurysm anatomy, and capture the heterogeneous and anisotropic nature of the coil mass interacting with the blood flow inside the aneurysmal sac. Thus, this simplified porous medium computational model could be used for the prediction of treatment outcome, incorporating it in computational fluid dynamics simulations with patient-specific boundary conditions. This objective was completed in different steps:

- First, to verify that coil-resolved simulations reproduced well the flow within the aneurysmal sac. To validate the coil-resolved simulations is essential for it to be considered as the reference model to validate the porous model.
- Second, to characterize the heterogeneity of the coils within the aneurysmal sac, and to take into account such heterogeneity in the definition of the permeability and inertial coefficients involved in Forchheimer's law.
- Third, to propose a porous model which can be used for prediction in clinical practice before the coiling procedure. This model must be as simple as possible and based on basic information available in clinical practice, such as the size and the shape of the aneurysm from CT scan imaging, and the target volume fraction of coils in the aneurysm determined by the surgeon.

## 1.3 Organisation of the manuscript

This manuscript is divided in four chapters:

- **Chapter 2.** In this chapter, we review the state of the art in research around cerebral aneurysms, focusing on modeling blood flow in aneurysms treated with coils. First, we present the pathophysiology of the aneurysm, the existing treatments and, in particular, aneurysm treatment with endovascular coiling. Then, we discuss the state of the art in methods to model blood flow in cerebral

aneurysms treated with coils. There are two types of numerical models. The coil-resolved models reproduce the complete anatomy of the aneurysm with the coils deployed in it (considered accurate patient-specific models). However, they haven't been validated experimentally, and the process to build these models is complex and can not be used prospectively in clinical practice to determine the treatment outcome. Porous medium models, on the other hand, are based on upscaling methods. These methods present several advantages. In particular, the simplicity of the model enables it to be used to study large cohorts of patients, and because it does not require sophisticated information that is not available in clinical practice, it can be used to predict treatment outcomes. However, the most commonly used models in the literature define the porous medium in a very simplistic way and have been shown to not reproduce blood flow in aneurysms accurately.

- **Chapter 3.** In this chapter, the first objective of this thesis is achieved: the coil-resolved model is validated experimentally. The planar-laser induced fluorescence (PLIF) technique is used to calculate the residence time of blood in the aneurysmal sac, from experiments conducted in silicone models built from patients' anatomies extracted from medical imaging. These silicone transparent models were treated with the exact same sequence of endovascular coils used in the actual patients, by the same neurosurgeon who treated the patients in real life. This is, to our knowledge, the first time that the hemodynamics in aneurysms treated with endovascular coils are experimentally imaged at high resolution. Passive scalar transport computations are performed within CFD simulations to calculate residence time in the coil-resolved model. The residence time results obtained numerically and experimentally are compared to validate the coil-resolved model.
- **Chapter 4:** In this chapter, we present the work to achieve the second objective of this thesis. 3D synchrotron x-ray images of coils deployed in silicone patient-specific aneurysm models are used to estimate the porosity distribution and porosity gradient in crowns along the aneurysm wall. Based on these results, a new porous model is proposed, where the permeability and inertial factor are defined to take into account the heterogeneity of the coil mass. The validity of the model has been assessed through comparisons with coil-resolved simulations for two patients.
- **Chapter 5.** In this chapter, we propose a porous medium model that can be used for the prediction of treatment outcomes (without requiring the geometry of the coils deployed inside the aneurysm), while considering the coils heterogeneity in the porous medium model. In this model, the permeability

and inertial factor are defined only from data available in the neuro-suite (i.e. the dimensions of the aneurysm and the volume fraction of coils inside the aneurysmal sac). This model was validated through CFD by comparing it with the coil-resolved simulations for a cohort of eight patients.

In the Conclusions Section, I discuss the main results of this thesis, as well as potential future work in the short and long terms. Chapters 3, 4, and 5 are presented as papers. Chapter 4 was submitted to a journal (Cardiovascular Engineering and Technology) and is currently under review, and Chapters 3 and 5 will be submitted soon. Due to this organisation, there might be some repetition of the description of the methodology among several chapters.



---

## State of the art

### Contents

---

2.1	Cerebral aneurysm treated with coil embolization . . . . .	<b>9</b>
2.1.1	Cerebral aneurysm and clinical management . . . . .	9
2.1.2	Coil embolization . . . . .	14
2.2	Hemodynamics in aneurysm with coils . . . . .	<b>17</b>
2.2.1	Modeling blood flow in cerebral aneurysm . . . . .	17
2.2.2	Modeling blood flow in coiled aneurysm : the coil-resolved model . . . . .	18
2.2.3	Modeling blood flow in coiled aneurysm : the porous model	24
2.3	Concluding remarks . . . . .	<b>40</b>

---

### Abstract

A leading treatment method to avoid rupture of the cerebral aneurysm wall is to fill the aneurysmal sac with metal coils introduced in the vasculature through a catheter that is placed inside the aneurysm. This treatment is often referred to as the coil embolization technique. A number of coils are introduced inside the aneurysmal sac, slowing down the flow of blood, and inducing thrombus formation. This technique is minimally invasive and has been proven to be very effective. However, there is a risk of recanalization. In that case, the thrombus formed does not completely fill the aneurysmal cavity and there persists a risk of rupture. Understanding the hemodynamics inside cerebral aneurysms would help predict the treatment parameters related to complete thrombosis and successful treatment. Due to the opacity of the coils, studying hemodynamics in treated aneurysms experimentally is very

challenging. Therefore, the goal of this thesis is to develop an accurate patient-specific numerical model that captures the true anatomy and physiology of the patient and the treatment medical devices. Coil-resolved models have been developed in the literature, where the geometry of the coils is reconstructed either from microtomography images, or using software to deploy the coils numerically. These methods can be considered as highly accurate, but would not be useful to predict patient-specific treatment outcomes, due to the need of highly sophisticated data, that is not available in clinical practice, to reproduce the coils deployed inside the aneurysm in vivo. A solution to this problem is to model the coils inside the aneurysmal sac as a porous medium. Many such models have been developed in the literature, but they don't accurately reproduce the hemodynamics of coiled aneurysms. The main objective of this thesis is to propose a porous model that is complex enough to capture the anatomy and physiology of blood flow in coiled-treated aneurysms, but simple enough that it could be used in clinical practice to predict patient treatment outcomes.

## 2.1 Cerebral aneurysm treated with coil embolization

### 2.1.1 Cerebral aneurysm and clinical management

#### 2.1.1.1 Cerebral aneurysm disease and its significance

A cerebral aneurysm (CA) is a deformation of the vascular wall in the cerebral arteries. Aneurysms can be categorized into different categories. First, there are two main morphologies: saccular and fusiform aneurysms (Figure 2.1). Saccular aneurysms represent 90% of all cerebral aneurysms [D'Souza, 2015] and are the focus of the aneurysms studied in this thesis. The location of the aneurysm is also an important defining factor. CAs appear on the arteries that form the circle of Willis, with 80-85% of them being on the anterior circulation [Schievink, 1997]. The circle of Willis is a circular manifold that distributes blood to the two hemispheres of the brain (Figure 2.2). The four main arteries that irrigate the brain meet at the circle of Willis: two internal carotid arteries (ICA) constituting the anterior circulation, and two basilar arteries, constituting the posterior circulation. Saccular aneurysms can also be differentiated according to their size: small (where the aneurysm diameter is below 10 mm), large (aneurysm diameter is below 25 mm) and giant (aneurysm diameter above 25 mm) [Seibert et al., 2011]. They can also be identified as ruptured vs non-ruptured. Most aneurysms do not rupture (50-80% according to literature [Brisman et al., 2006]). However, aneurysm rupture leads to subarachnoid hemorrhage (SAH) with very high mortality and morbidity. SAH affects 1/10000 persons with poor outcomes for 35% of patients [Brisman et al., 2006; D'Souza, 2015; Etminan and Rinkel, 2016; Johnston et al., 1998].

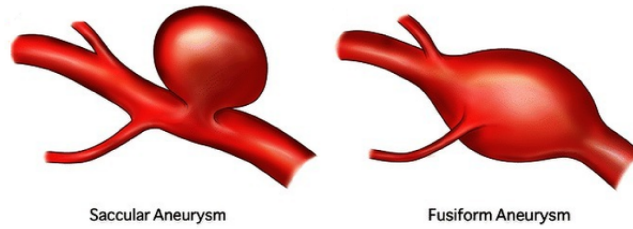


Figure 2.1: Saccular (left) and fusiform (right) aneurysms.

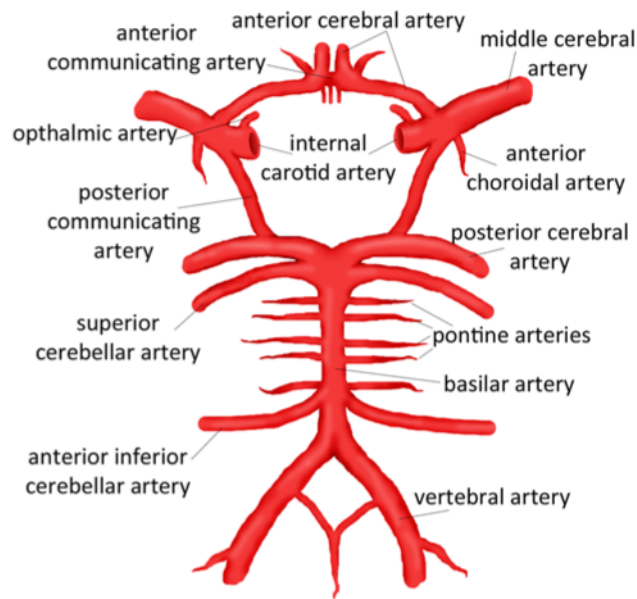


Figure 2.2: Circle of Willis, from The Children’s hospital of Wisconsin [Chiu et al., 2019]

Cerebral aneurysms affects 1 to 5% of the adult population [Brisman et al., 2006; Vlak et al., 2011], and mostly develop after the second decade of life [Etminan and Rinkel, 2016], with 5-15% of strokes related to their rupture [Brisman et al., 2006; D’Souza, 2015]. The disease is caused by a combination of environmental factors as hypertension, smoking, heavy alcohol consumption, as well as genetic factors and hemodynamics [Brisman et al., 2006; Etminan and Rinkel, 2016; Schievink, 1997; Vlak et al., 2011]. Most of the patients are asymptomatic, with the only symptoms possibly being cranial nerve palsies [Brisman et al., 2006]. Diagnosis is done by medical imaging: existing options are Computed Tomography Angiography (CTA) after venous injection of contrast agent, Magnetic Resonance Angiography (MRA), or catheter angiography [Brisman et al., 2006; Schievink, 1997].

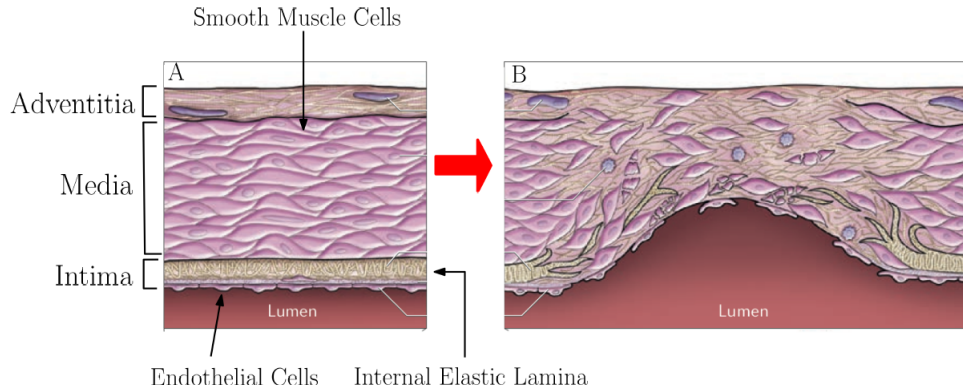


Figure 2.3: A) Healthy vessel wall. B) Arterial wall histology following aneurysm initiation and growth: disruption of the IEL, thinning of the medial layer. Figure is taken from *Etminan and Rinkel* [2016] with the adaptation made by Barbour's work [Barbour, 2018].

### 2.1.1.2 Aneurysm pathophysiology

Vascular vessel walls are constituted by three distinct layers: the intima, the media, and adventitia (see Figure 2.3). The adventitia is constituted mostly of collagen fibers, and forms a protective layer for the vessel structural integrity. The media is formed of smooth muscle cells, embedded in a network of elastin and collagen, and macromolecules that constitute the extracellular matrix. The intima layer is composed of two layers: a thin elastic membrane called the internal elastic lamina (IEL) and a monolayer of endothelial cells.

The origin of aneurysm formation is the interaction of the arterial wall mechanobiology and the hemodynamics stresses that cause functional and morphological changes on the arterial wall [Sforza *et al.*, 2009]. Endothelial cells respond to hemodynamics stresses, elongating and changing their alignment, including apoptosis, migration of the cells and a change in density [Chalouhi *et al.*, 2012; Seibert *et al.*, 2011]. Patients' environmental and genetic factors, in addition to hemodynamics stresses on the vessel wall, can lead to changes on the vessel wall constituents, through endovascular cell dysfunction. Changes in the vessel wall cause an inflammatory response and therefore an immunological reaction. The interaction of the immune system and the vessel wall cells leads to extracellular matrix remodeling and vessel degeneration mainly characterized by the loss or disruption on the IEL [Chalouhi *et al.*, 2012; Etminan and Rinkel, 2016]. The once organized and structured layered wall vessel becomes disorganized, with fewer layers in the aneurysm wall. These changes constitute the frame to develop a cerebral aneurysm, and its progression [Chalouhi *et al.*, 2012; Etminan and Rinkel, 2016; Seibert *et al.*, 2011]. The growth of the aneurysm is discontinuous and non-linear [Etminan and Rinkel, 2016]. The

process is summarized in Figure 2.3.

Cerebral arteries have certain characteristics that make them susceptible to develop an aneurysm. The vessel wall is composed of a sparse tunica adventitia and has a lower proportion of fibers than normal arteries, which promotes disruption [Etmnan and Rinkel, 2016]. Cerebral arteries are immersed in cerebrospinal fluid of the subarachnoid space, without any fibers or muscle tissue to support the arterial wall [Etmnan and Rinkel, 2016; Seibert et al., 2011]. The anatomical variations in the circle of Willis are considered to be an important factor in aneurysm formation. In that anatomical structure, the vasculature presents bifurcations and sharp angles [Etmnan and Rinkel, 2016; Seibert et al., 2011]. The complexity of the anatomy in this area and the lack of support of the vessel wall promotes aneurysm formation and non physiological growth in cerebral arteries.

### 2.1.1.3 Clinical management

As discussed previously (see section 2.1.1.1), SAH has poor outcomes, therefore, ruptured aneurysms need to be treated immediately. SAH can be detected with CT angiography or cerebral angiography [D'Souza, 2015]. Surgical clipping, endovascular coiling or stent flow diversion are treatments used to stop the growth of aneurysms and prevent a rupture and subsequent subarachnoid hemorrhage [D'Souza, 2015]. The endovascular coiling technique to treat ruptured aneurysms is suggested to present the best primary outcome [D'Souza, 2015]. One of the important advantages of this technique is that the duration of the surgical intervention is shorter than the clipping surgery [Bederson et al., 2009]. Surgery time is crucial when dealing with SAH to ensure a better outcome for the patient.

The clinical management of unruptured aneurysm patients is also complex. Risk factors for CA include patient's general health and environmental aspects, such as hypertension or smoking, and also whether the patient has a previous history of CA. Larger aneurysms have higher risk of rupture, as do aneurysms located in the posterior circulation [Etmnan and Rinkel, 2016; Seibert et al., 2011; D'Souza, 2015; Vlák et al., 2011]. However, rupture can happen even when these conditions aren't present in the patient. There are different outcome scenarios for the evolution of the aneurysm: stochastic growth until rupture, growth without rupture (stable aneurysm), stability without growth but rupture, and fast development of a small CA and rupture [Etmnan and Rinkel, 2016]. Therefore, even if most of aneurysms do not rupture [Brisman et al., 2006], treatment is recommended for most aneurysms [Brisman et al., 2006] due to the poor outcomes after rupture and the inability to predict if or when rupture will happen.

#### 2.1.1.4 Treatment methods for unruptured aneurysms

Different treatment methods exist for unruptured aneurysms. The most conservative method is observation, which consists of a follow-up of the evolution of the aneurysm. However, if the surgeon decides that the aneurysm presents a danger of rupture, the treatment options are surgical clipping or endovascular techniques [Brisman *et al.*, 2006].

In both treatments, the purpose remains to remove the cerebral aneurysm from the circulation. The surgical clipping technique consists of placing a clip at the neck of the aneurysm after performing a craniotomy (Figure 2.4B). The main risk associated with this practice is the surgical procedure itself, since it is very invasive with overall morbidity of the procedure approximately 6.7% [Etminan and Rinkel, 2016]. This technique cannot be used to treat all cerebral aneurysms as some of them are difficult to access, in particular those in the posterior circulation [Seibert *et al.*, 2011; Bederson *et al.*, 2009].

Endovascular coiling consists of deploying coils in the aneurysm to create a thrombus isolating it from hemodynamics stresses [Bederson *et al.*, 2009], see Figure 2.4A. This technique has proven to have similar rates of success as surgical clipping. However, being less invasive, the procedure presents a lower risk for the patient, which translates in lower mortality and morbidity, as well as shorter hospitalization stays [Seibert *et al.*, 2011].

However, not all aneurysms can be treated with platinum coils. Deploying coils in an aneurysm with a wide neck or a difficult shape can present a danger of the coils moving into the parent vessel and disturbing blood flow there. In those situations, a stent-assisted coiling technique is preferred: a stent is placed in the parent vessel where the aneurysm is placed, establishing a scaffold for coiling [Seibert *et al.*, 2011], see Figure 2.4C.

When there is no possibility of treating the aneurysm with coils (with or without stent) as can happen for giant aneurysms, the flow diversion technique is used. Flow diversion devices are similar to stents, however their mesh coverage is higher, ensuring that blood flow is impeded as it tries to cross the diversion device walls and enter the aneurysm [Seibert *et al.*, 2011], see Figure 2.4D.

Currently, there is no agreement on a particular technique as the best treatment, however endovascular techniques are encouraged due to the safety for the patient during the procedure and its positive impact on hospitalization stays. The management choice remains based on the decision of the surgeon that estimates the risk of rupture, risk of complications, life expectancy of the patient, and other related factors. This thesis is focused exclusively on cerebral aneurysms treated with endovascular coiling. The coil embolization treatment and the outcomes of this treatment are described in the following sections.

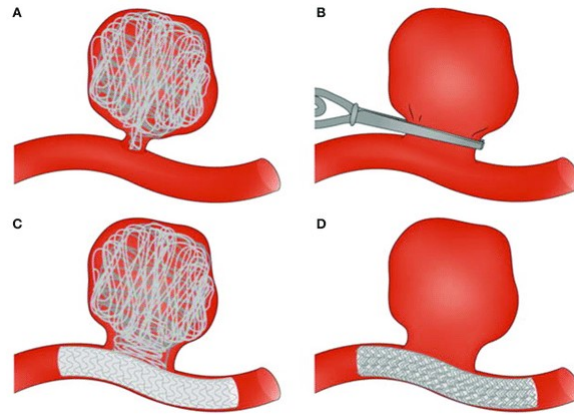


Figure 2.4: Treatment methods for cerebral aneurysm: a) Endovascular coiling b) Surgical clipping c) Stent-assisted coiling d) Flow diversion. Source: [Perrone *et al.*, 2015]

## 2.1.2 Coil embolization

### 2.1.2.1 Description of the technique

The purpose of the surgical and endovascular treatment techniques is to isolate the aneurysm from the circulation. Embolization means blocking a blood vessel using an external body, which in this case are the coils. To achieve this, the objective of the coil embolization technique is to decrease the blood flow in the aneurysm by deploying coils inside. As the velocity decreases, being a non-Newtonian fluid, the blood's viscosity increases and ensuring coagulation [Piotin *et al.*, 2007]. The platinum coils have a thrombogenic surface and trigger the coagulation cascade ensuring fibrin coagulation and the formation of a thrombus [Wootton and Ku, 1999].

The procedure is described in Seibert *et al.* [2011]. The patient goes under general anesthesia or conscious sedation. Biplane fluoroscopy ensures visualization of the devices and the aneurysm once in the patient. The catheter penetrates into the femoral artery and navigates through the internal carotid or the vertebral artery until reaching the circle of Willis and the specific location of the aneurysm. Once the microcatheter is in the aneurysm, platinum coils of various configurations and sizes are deployed. The first coils deployed are sized as the maximum diameter of the coils. Once those framing coils are placed filling coils are detached. Figure 2.5 illustrates the process. Figure 2.6 shows the procedure seen by the surgeons, in particular in C) we can see the total occlusion after coil embolization and how the aneurysm is isolated from the main blood flow circulation.

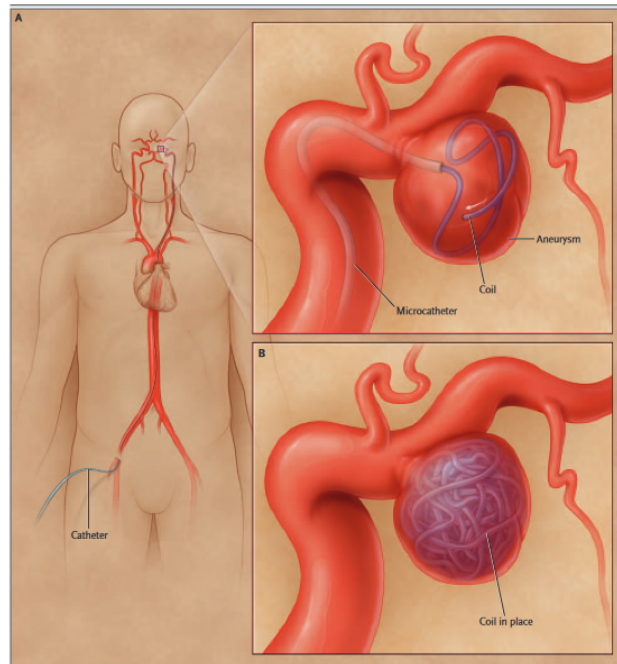


Figure 2.5: Illustration of the coils being deployed (up) and set (down) in a cerebral aneurysm. Source: *Brisman et al.* [2006].

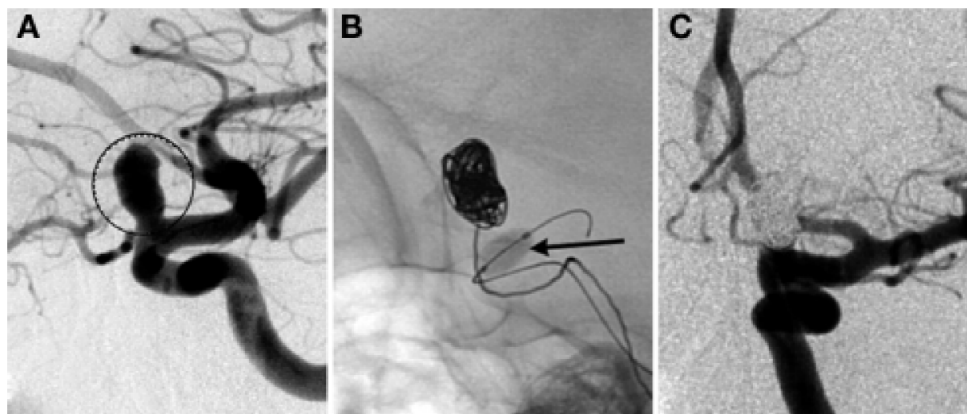


Figure 2.6: A) Untreated internal carotid artery (ICA), B) Coil mass deployed in the cerebral aneurysm, C) Total occlusion. Source : *Seibert et al.* [2011].

### 2.1.2.2 Treatment outcome

There are risks associated with the procedure itself. There is a 2.4% risk of aneurysm perforation and 8.5% risk of ischemic complication. However, these complications are only permanent in 3.7% of the cases [Bederson *et al.*, 2009].

Recurrence affects 21-24% [Etminan and Rinkel, 2016; Seibert *et al.*, 2011] and rebleeding (SAH) after recurrence concerns 0.2–7.9% of the cases [Abdihalim *et al.*, 2014]. Recurrence leads to a modification of hemodynamics stress and encouraging aneurysm growth in 49% of the cases [Bederson *et al.*, 2009; Grunwald *et al.*, 2007]. The initial angiographic assessment after treatment is not enough to evaluate the state of the occlusion of the embolized aneurysm [Tamatani *et al.*, 2002]. However, an assessment after 6 months can predict the treatment outcome as 93.8% of aneurysms that show occlusion tend to be stable long term [Jeon *et al.*, 2016].

Large aneurysms and aneurysms with wide necks are more prone to not fully occlude [Bederson *et al.*, 2009; Tamatani *et al.*, 2002; Piotin *et al.*, 2007; Abdihalim *et al.*, 2014; Grunwald *et al.*, 2007]. As studied in the literature, small aneurysms with a small necks ( $< 4$  mm) recurred in 5% of the cases, but when they have wide necks it increases up to 20%. Large aneurysms (10 – 25 mm) present a recurrence rate of 30 – 50%, and giant aneurysms ( $> 25$  mm) a rate of 59 – 87% [Crobeddu *et al.*, 2013]. The location of the aneurysm has also an impact as aneurysms in bifurcations present more risk of recurrence than side walls aneurysms [Jeon *et al.*, 2016].

Recanalization is due to coil compaction and insufficient packing combined with hemodynamic stresses [Seibert *et al.*, 2011; Jeon *et al.*, 2016]. Studies have shown that when embolization is above 25% the rate of recurrence events improves [Tamatani *et al.*, 2002]. However, maximizing packing can lead to aneurysm perforation or the coils might disturb the flow in the parent vessel [Crobeddu *et al.*, 2013]. Coil compaction is a consequence of poor packing or cerebral aneurysm growth [Crobeddu *et al.*, 2013]. The water hammer effect of the pulsatile blood flow and the new space created promotes coil compaction [Abdihalim *et al.*, 2014]. There are more risks of coil compaction for larger aneurysm [Sluzewski *et al.*, 2004]. Improving the packing can avoid the coil compaction: the embolization volume should be between 25 and 33% to ensure full occlusion and avoid overpacking the aneurysm [Satoh *et al.*, 1997; Sluzewski *et al.*, 2004].

### 2.1.2.3 Prediction of treatment outcome

To avoid recanalization, research is turning towards predicting numerically through computational fluid dynamics the treatment outcome. Hemodynamics of blood flow in the aneurysm have been studied to analyze the development of the aneurysm. Finding the relation between recanalization rate and hemodynamic parameters can help to understand and predict the risk of recanalization.

Hemodynamics have been related to aneurysm growth and rupture in the literature. They can help determining the location of the aneurysm: bifurcation areas and curved arterial segments present more risk of aneurysm growth. Those areas are subject to high-pressure impacts, being more than two times higher than the maximal luminal pressure in the parent artery [Foutrakis *et al.*, 1999]. In these areas, the wall is not only exposed to high pressures but also high wall shear stress gradient (WSSG). Destructive remodelling are associated with high WSSG and wall shear stress (WSS) values [Meng *et al.*, 2007; Sforza *et al.*, 2009; Metaxa *et al.*, 2010]. The areas of bifurcation present complex flow patterns: an oscillatory flow appears in those areas leading to a change in WSS that triggers the inflammatory response and the destructive remodeling [Meng *et al.*, 2014; Hahn and MA.Schwartz, 2009].

The aneurysm's anatomy is strongly related to hemodynamics as well: it determines the flow conditions and the flow drives the remodeling of the aneurysmal wall [Milner *et al.*, 1998]. The aneurysm is shaped with the flow as it leans in its direction [Foutrakis *et al.*, 1999].

For cerebral aneurysms treated with endovascular coiling, preliminary studies show that future aneurysm recanalization is related to high WSS areas of remanent neck [Li *et al.*, 2012]. Therefore hemodynamic parameters can help in determining the risk of recurrence. Studies show also that hemodynamics are linked with patients specificities [Sforza *et al.*, 2009]. Therefore, hemodynamics related to aneurysm recanalization need to be studied in patient-specific configuration [Milner *et al.*, 1998].

Previous research has been already working in associating hemodynamics with recanalization risk. However, the first difficulty is to model blood flow in a coiled aneurysm. Several approaches have been developed which are presented in the next section.

## 2.2 Hemodynamics in aneurysm with coils

### 2.2.1 Modeling blood flow in cerebral aneurysm

Hemodynamics has been related to the growth and rupture of the aneurysm and can be a valuable tool in understanding the thrombus formation in treated aneurysms (see section 2.1.2.3). They can be identified through medical imaging, for example, Milner *et al.* [1998] propose a non-invasive MRI protocol to determine hemodynamics in cerebral aneurysms. Other invasive techniques to measure velocity and pressure are explained in the following sections.

Computational fluid dynamics is a numerical tool used to study hemodynamic parameters. Developing blood flow in the aneurysm models presents an important step towards predicting the treatment outcome. These computational models have

proved to improve the results by considering patient-specific data: the anatomy of the aneurysm, and the inflow and outflow parameters [McGah *et al.*, 2014; Venugopal *et al.*, 2007; Karmonik *et al.*, 2009]. In this section, we will present some of the hypotheses of the computational models that will be used in our study based on literature results.

First, the vessel wall can be considered rigid since cerebral aneurysms and parent vessel's walls are less distensible than normal extracranial aneurysms and parent vessel walls [Foutrakis *et al.*, 1999]. This has been proved by comparing hemodynamics on both rigid and compliant tubes, and finding little difference between the two models [Foutrakis *et al.*, 1999].

Studies have compared non-Newtonian and Newtonian rheology models for the blood, but the differences in WSS magnitude and flow patterns in the results were not significant [Gambaruto *et al.*, 2011; Fisher and Rossmann, 2009; Castro *et al.*, 2014]. Therefore for modeling blood flow in the aneurysm, the blood is assumed Newtonian and incompressible.

Concerning the studied parameters, the mean velocity remains an important parameter when studying blood flow in an aneurysm as it can be related to thrombus formation [Seibert *et al.*, 2011]. WSS is also a studied parameter, however, it remains very controversial. Both high and low WSS has been related in the literature with aneurysm growth and rupture [Meng *et al.*, 2014]. However, the variability of cerebral aneurysm pathophysiologies shows the difficulty in the interpretation of these parameters [Meng *et al.*, 2014].

Most of the models available in the literature have been developed for aneurysms without coils [Khan *et al.*, 2015; Valen-Sendstad and Steinman, 2014; Sanchez *et al.*, 2013], however, to study the risk of recurrence, blood flow in coiled aneurysms must be investigated. We can distinguish two main approaches: the first one is the coil-resolved model (a biofidelic model) and the second one is based on a porous model. These two approaches are presented more in details in the following.

## **2.2.2 Modeling blood flow in coiled aneurysm : the coil-resolved model**

### **2.2.2.1 Existing biofidelic numerical model for treated aneurysms with coils**

Modeling blood flow in cerebral aneurysms with coils can help in the prediction of treatment outcomes, although it presents one main challenge: the coil mass cannot be reconstructed from clinical images. CT images present artifacts, and MRI resolution is too low, therefore the geometry of the coil cannot be extracted.

To address this problem, studies have developed methodologies to reproduce the geometry of the coils by microtomography methods [Levitt *et al.*, 2016; Yadollahi-Farsani *et al.*, 2019]. If we focus on Levitt *et al.* [2016] research at the University

of Washington, their approach consists of scanning at high energy, to avoid beam hardening effects, in a Synchrotron 3D printed aneurysmal phantoms containing the coils. This allowed creating a 3D patient-specific numerical model of the aneurysm with coils. Then the hemodynamics in the coiled aneurysm has been studied assuming that the wall and the coil are rigid and the blood is Newtonian. Navier Stokes equations were solved using patient-specific boundary conditions at the inlet and outlet of the parent vessels, and metrics as mean velocity, WSS, oscillatory shear index (OSI) were studied. This approach presents one main advantage, the geometry of the coils is biofidelic as the deployments are performed by the same surgeon who performed the procedure in the patient. With this methodology, patient's treatment outcome could be related with hemodynamic parameters deduced from studying blood flow with this coil-resolved model. However, with this methodology, blood flow simulations cannot be used for prediction, and it needs a high computational time to be applicable in the treatment decision making [Augsburger *et al.*, 2011]. Moreover, up to now, to the best of our knowledge, these types of simulations have been performed for only a few patients.

The second technique developed to model blood in the treated aneurysm is to use software to deploy coils virtually in the aneurysm [Yadollahi-Farsani *et al.*, 2019; Babiker *et al.*, 2013; Morales *et al.*, 2013]. If we focus Morales *et al.* [2013] work, they have developed an algorithm to deploy coils in the aneurysm and it has been validated in patient-specific anatomies by comparing packing density, the general shape of the coils (visual assessment), and hemodynamic data with clinical data. This method only takes a couple of minutes to be deployed, which presents an advantage when being compared with the microtomography methods. With this method, there is no need of the CT scan of the coils to reconstruct the coils geometry. However, the validation was not complete, the deployment was only validated visually and did not pursued a deep comparison with microtomography studies. Therefore, this model do not ensure clinical reproduction and therefore relating hemodynamics with success of treatment becomes unpredictable.

Both coil-resolved methods based on microtomography or virtual coils deployment can be used for modeling blood flow in treated aneurysms but couldn't be used to predict the treatment outcome for the patients. These coil-resolved models could be used as a reference for the development of other more efficient models, such as the porous model presented in the following section. Up to date, there hasn't been any experimental validation of these models. Studying hemodynamics in the coils aneurysm experimentally presents an important challenge due to the opacity of the coils. However, the coil-resolved models need to be experimentally validated to use as references for other models, or just to confirm their biofidelity. In this study, we will focus on the coil-resolved model where the geometry of the coils is obtained through microtomography. This method developed by Barbour [2018] is described

in the following paragraph.

### 2.2.2.2 General method developed at the University of Washington to build the coil-resolved model

The objective is to create a patient-specific numerical model of aneurysm treated with coils (coil-resolved model). This model is based on medical imaging data and *in vivo* measurements. We will first present the data acquisition process, then the computational model generation, and finally the hypothesis for the computational model simulations. All these different steps are detailed in Michael Barbour's Ph.D. work [*Barbour, 2018*].

**Patient data acquisition.** The patients participating in this study were over 18 years old, presenting unruptured aneurysms which diameters were above 5 mm. The aneurysm was in the Circle of Willis, for the majority of the cases being in the ICA or basilar artery. All the aneurysms were treated with endovascular coiling. The patients were recruited and treated at the University of Washington's Harborview Medical center in Seattle.

The patients were not under general anesthesia inside the angiography suite. The catheter was inserted through the femoral artery and guided to the aneurysm. The catheter path is guided with fluoroscopy that allows the surgeon to follow the process. Images of the patients' arteries and aneurysms were acquired with 3D rotational angiography technologies. The catheter has multiple functions: it serves as a contrast vehicle, it measures blood flow and pressure, and it deploys the coils.

The blood flow velocity and pressure were measured using ComboWire and ComboMap (Volcano Corp, San Diego, CA). The wire contains a piezoresistive pressure sensor and a piezoelectric pulsed Doppler velocity sensor. The measurements were taken in four different locations around the aneurysm (neck, 5 mm proximal to the neck, petrous carotid, and 5 mm distal to the neck), and at the maximum velocity point, in the centerline of the parent vessel. Measurements were taken every 5 ms and were used to define inflow and outflow boundary conditions. The Doppler measurements can be visualized in Figure 2.7.

After collecting the velocity and pressure data, the coils were deployed: first, the large framing coils and then the filling coils. The coils were deployed until the dye could no longer enter the aneurysm or when the surgeons judge that adding coils could present a risk for the patient's health (obtrusion of the parent vessel or risk of aneurysm wall perforation).

**Computational model generation** The aneurysm and parent vessel were re-constructed using image segmentation of the 3D rotational angiography images.

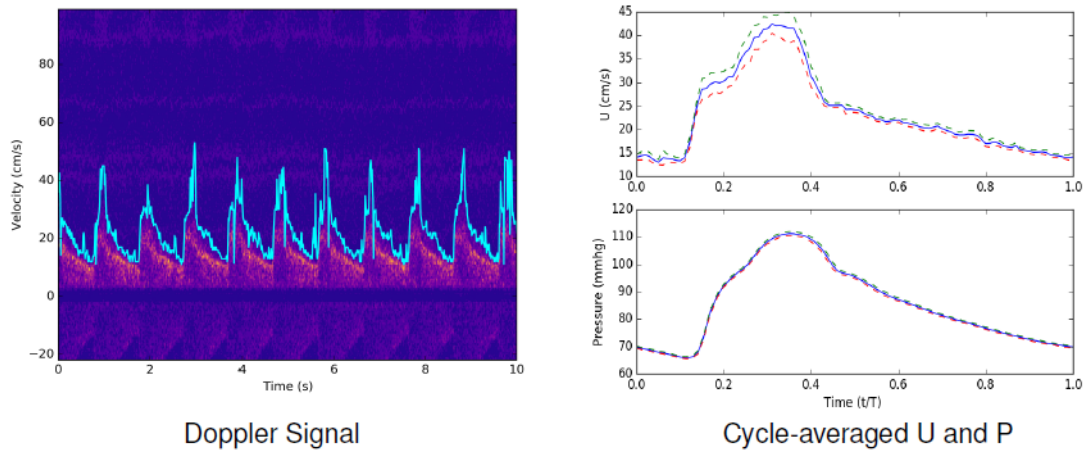


Figure 2.7: Sampler Doppler velocity from ComboWire (left). Phase average velocity (top) and pressure (bottom), the dotted lines present two standard deviation. The source is *Barbour* [2018]

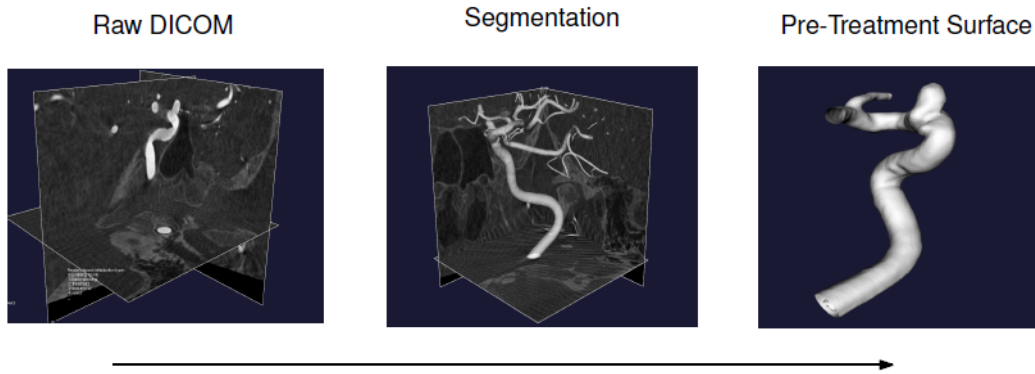


Figure 2.8: Summary of the reconstruction of the vessel surface, from left to right: raw DICOM images, initial surface segmentation, cleaned/clipped surface. Source *Barbour's* work [*Barbour*, 2018]

The segmentation was done using VMTK and following these steps: initializing the geometry using reconstruction methods, eliminating the small vessels that do not play a role in the hemodynamics of the aneurysm, and adding flow extensions. The summary of the generation of the computational model can be seen in Figure 2.8.

The models of the aneurysm and vessel were then created in transparent silicone for each patient and treated with the same number of coils, deployed in the same order, as it was done during the surgical procedure. The models were then scanned at the European Synchrotron Facility (ESRF) and from those images, after image treatment, the geometry of the coils was reconstructed. To ensure that the coils were placed in the exact location in the numerical model as they were in the physical model, the iterative closest point method was used [*Wilm*, 2020].

Once the coils were placed back, the mesh was generated using STARCCM+

(CD-adapco, Melville, New York, USA) to run CFD simulations with ANSYS FLUENT (Release 14.1; ANSYS, Canonsburg, Pennsylvania, USA). The aneurysm was separated from the parent vessel with a neck (surface defined as the envelope of the coils). The mesh was tetrahedral with a global element mesh size of 0.16 mm and 4 prismatic boundary layers. The mesh is refined in areas of high curvature, and at the neck interface where the element size can decrease until 0.06 mm. This level of discretization is enough according to the literature to describe the blood flow in the aneurysm [Valen-Sendstad and Steinman, 2014; Khan et al., 2015].

**Computational simulations.** In this part, we developed the hypothesis made at the boundary conditions for the computational simulations.

At the inlet, a Womersley profile was considered [Womersley, 1955]. The inlet was truncated at 5 mm, one of the locations of the Doppler velocity measurements (petrous segment near the base of the skull). The wire was placed at the maximum velocity in a section, for twenty cardiac cycles. The phase average generated a velocity waveform at the centerline:

$$U_{CL}(t) = A(\omega)e^{i\omega t} \quad (2.1)$$

where  $A$  are the Fourier modes and  $\omega$  the frequency. The Womersley profile [Womersley, 1955] is described as:

$$w(r, t) = A_0(1 - (r/R)^2) + \sum_{n=1}^N \tilde{A}_n \left[ 1 - \frac{J_0(i^{3/2}W_{on}r/R)}{J_0(i^{3/2})} \right] e^{i\omega_n t} \quad (2.2)$$

where  $r$  is the radius coordinate of the tube,  $R$  is the tube radius,  $J_0$  is the Bessels function of the first kind.  $W_o$  is the Womersley number, a non-dimensional parameter that relates the time-scales of the cardiac cycle to the time-scale of viscous diffusion and is defined as

$$W_{on} = R\sqrt{\frac{2\pi n}{T\nu}} \quad (2.3)$$

with  $T$  being the period of the cardiac cycle and  $\nu$  the viscosity. The Fourier coefficients are calculated based on this equation:

$$\tilde{A}_n = 2A_n / \left[ A - \frac{1}{J_0(i^{3/2}W_{on})} \right] \quad (2.4)$$

Eight to ten Fourier modes were chosen to reconstruct the waveform reproducing the phase average velocity obtain through *in vivo* measurements. The profile was implemented in the CFD program (Fluent, ANSYS) using a user-defined function.

The outlet boundary condition depends on the number of outlets in the model. If there is only one model, the pressure outlet condition is 0 Pa. However, if there

is more than one, the pressure outlet is calculated using a two-element Windkessel model.

The Windkessel model can be related to a simple RC circuit, with the pressure being the voltage and the blood flow the current. This model comes from the theory that the flow travels through a complete vessel system and that it distends the elastic artery wall. The flow rate through the peripheral system can be approximated by  $P/R$ , where  $P$  is the local arterial pressure, and  $R$  is the resistance of the distal vascular bed. The portion of the blood flow causing a volume change in the arterial wall is proportional to the rate of change in the arterial pressure. That proportional constant is compliance  $C$ . The flow rate through the arterial system can be written as:

$$Q(t) = C \frac{dP(t)}{dt} + P(t)/R \quad (2.5)$$

This equation allows us to determine the pressure outflow. For each of the boundaries, unique resistance and compliance are defined as each leads to a different vascular bed. The time average flow rate for each outlet, denoted  $i$ , is:

$$\bar{Q}_i = \bar{Q}_T (D_i/D_T)^2 \quad (2.6)$$

where  $\bar{Q}_T$  is the time average flow rate (ComboWire velocity),  $D_i$  the diameter of the outflow branch  $i$ , and  $D_T$  the summation of all outflow diameters. Therefore Resistance for each branch are:

$$R_i = \bar{P}/\bar{Q}_i \quad (2.7)$$

where  $\bar{P}$  is the mean arterial pressure proximal to the flow split. This equation was used to compute the pressure in each outlet. The compliance values were taken from Alastruey's study [Alastruey *et al.*, 2007] that computed arterial compliance of vascular beds distal to every main cerebral artery including the anterior cerebral artery (ACA), middle cerebral artery (MCA), and posterior cerebral artery (PCA).

The aneurysmal wall was considered as a solid wall having a non-slip boundary condition. The reasons to justify considering the wall as solid are defined in section 2.2.1.

The summary of the complete methodology from the patients arriving in the neuro suite to the coil-resolved model can be found in Figure 2.9. This figure highlights the complexity of the process and the number of phases necessary to create the coil-resolved model. This long process involves several actors from the surgeons to the researchers working on this project. The coil-resolved was used to compare hemodynamics between treated and non treated patients, also for the treated aneurysms, the successful versus failure treatment outcome [Barbour, 2018]. Some of the results obtained show that embolic coils modify the aneurysm hemodynamics.

In particular, for aneurysm where there has been a failed coil embolization, they present significantly higher neck shear stress in comparison with the neck shear stress of the successful treatment. Therefore there were some interesting results to start determining the parameters related with treatment success.

As previously explained, the coil-resolved model cannot be used for prediction, and modeling blood flow in treated aneurysms as a porous media would not solve this issue, it would also represent a saving in time and expenses as the computational model generation part would be simplified. Indeed, with a porous model, only the pre-treatment surface is needed to study hemodynamics (see Figure 2.9), simplifying significantly the process and promoting studies with a large cohort of patients.

### 2.2.3 Modeling blood flow in coiled aneurysm : the porous model

#### 2.2.3.1 Introduction

To overcome the drawbacks of coiled resolved models, numerical models have been recently proposed in the literature where the coil is replaced by a porous medium [Levitt *et al.*, 2016; Kakalis *et al.*, 2008; Mitsos *et al.*, 2008; Yadollahi-Farsani *et al.*, 2019]. By doing so, we can expect to perform simulations in a reasonable time without knowing the detailed geometry of the coil within the aneurysmal sac, but only the expected mean porosity after coiling and the coil diameter. The development of such numerical models requires (i) to model the blood flow within the coil using an equivalent model (such as Darcy's law) and (ii) to use specific methods to compute the flow in such fluid-porous medium. In the following, the main results concerning these two points are briefly recalled and finally, porous models applied to simulate blood flow in coiled aneurysms are presented.

#### 2.2.3.2 Modeling incompressible Newtonian flow in saturated porous media

In this section, the main results concerning the modelling of fluid flow through a saturated porous media are summarized.

**Fluid flow at the microscopic (pore) scale.** At the pore scale, the porous medium is constituted by a solid phase  $\Omega_s$  and a fluid phase  $\Omega_f$ , separated by an interface  $\Gamma$  as seen in Figure 2.10. This medium is characterized by its porosity, i.e. the ratio between the fluid volume and the total volume, and a characteristic length  $l_c$  which is typically the size of the pores. The solid phase is assumed to be rigid. At the pore scale, the flow of an incompressible Newtonian fluid in steady-state condition is described within  $\Omega_f$  by the Navier-Stokes equation and the incompressibility condition:

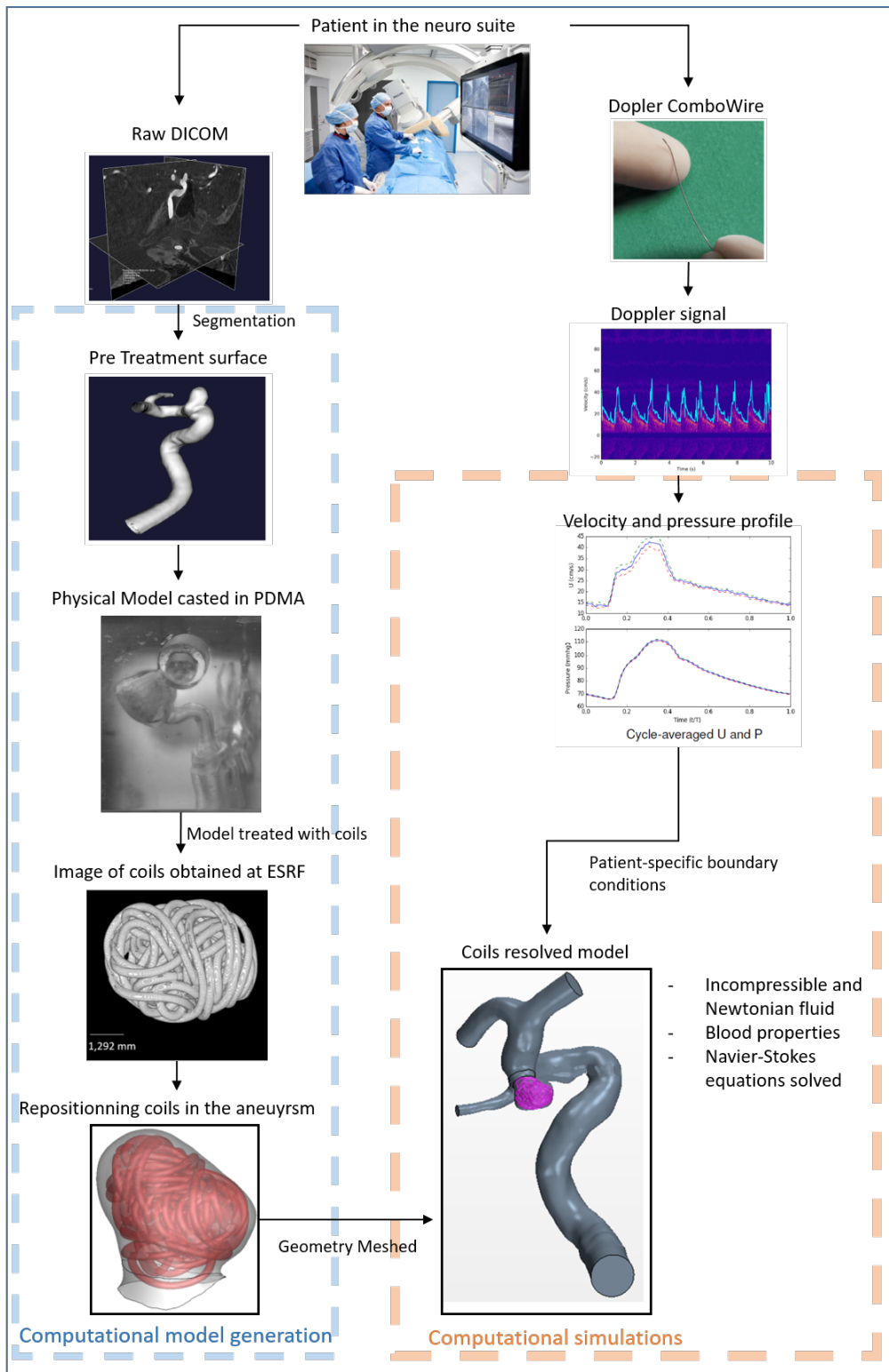


Figure 2.9: Full process of the coil-resolved model: From the data acquisition, to the computational model generation and finally the computational simulation.

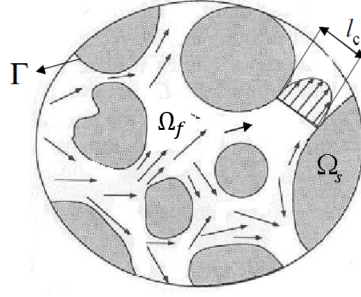


Figure 2.10: Scheme of fluid flow through a porous media up the microscopic scale

$$\rho(\mathbf{u} \cdot \nabla) \mathbf{u} = -\nabla p + \mu_0 \nabla^2 \mathbf{u} \quad \text{in } \Omega_f \quad (2.8)$$

$$\nabla \cdot \mathbf{u} = 0 \quad \text{in } \Omega_f \quad (2.9)$$

where  $p$  (Pa) is the pressure,  $\mathbf{u}$  (m/s) is the fluid velocity,  $\mu_0$  (Pa.s) is the dynamic fluid viscosity and  $\rho$  (kg/m<sup>3</sup>) is the fluid's density. On the interface  $\Gamma$ , the no-slip boundary condition is written:

$$\mathbf{u} = \mathbf{0} \quad \text{on } \Gamma \quad (2.10)$$

The fluid flow at the pore scale can present different regimes that are characterized by the Reynolds number at the pore scale defined as:

$$Re_p = \frac{\rho_c v_c l_c}{\mu_{0c}} \quad (2.11)$$

where the subscript  $c$  denotes characteristic values at the pore scale.

**Fluid flow at the macroscopic (porous medium) scale.** By using different upscaling methods, it can be shown that the above fluid flow at the pore scale can be modeled at the macroscopic scale (the scale of the sample) by a homogeneous description. This equivalent description exists if the separation of scales condition is satisfied [Auriault, 1991] (Figure 2.11). This condition is written:

$$\epsilon = \frac{l}{L} \ll 1 \quad (2.12)$$

where  $l$  is the characteristic length of the Representative Elementary Volume (REV) of the porous medium and  $L$  is the characteristic length of the sample. The REV must contain a sufficient number of heterogeneities to represent the material and the physical phenomena in the medium. In the present case, starting from the fluid flow description at the pore scale, it can be shown that the macroscopic flow law depends on the Reynolds number at the pore scale [Auriault et al., 2009]:

- When  $Re_p < 1$ , at the pore scale, inertial effects are negligible in front of the viscous effects. In this regime, Navier-Stokes equations are reduced to Stokes equations:

$$\nabla p = \mu_0 \nabla^2 \mathbf{u} \quad \text{in } \Omega_f \quad (2.13)$$

In that case, it can be shown that the fluid flow through the porous medium is described by the well known Darcy's law [Darcy, 1856]:

$$\nabla p = -\mu_0 \mathbf{K}^{-1} \mathbf{u}_p \quad (2.14)$$

where  $\mathbf{u}_p$  is Darcy's velocity of the fluid through the porous media (i.e. the volume average of  $\mathbf{u}$  over the REV) and  $\mathbf{K}$  [ $m^2$ ] is the intrinsic permeability tensor (2nd order tensor) which depends on the porous medium microstructure. In the case of an isotropic porous media, Darcy's law is written:

$$\nabla p = -(\mu_0/K) \mathbf{u}_p \quad (2.15)$$

where  $K$  is a scalar.

- When  $Re_p > 1$ , at the pore scale, inertial effects are no more negligible in front of the viscous effects [Mei and Auriault, 1991; Skjetne and Auriault, 1999]. In the case of an isotropic porous medium, the macroscopic flow law, also called the Forchheimer's law, is now written [Forchheimer, 1901; Ergun, 1952]:

$$\nabla p = -\frac{\mu_0}{K} \mathbf{u}_p - (1/2) \rho C_2 \mathbf{u}_p^2 \quad (2.16)$$

where  $\rho$  is the fluid density ( $\text{kg/m}^3$ ) and  $K$  ( $m^2$ ) is permeability and  $C_2$  ( $1/m$ ) is the inertial factor coefficient, also called the Forchheimer factor, which characterized inertial effects at the macroscopic scale and which depends on the porosity at the first order. Let us remark that the generalization of this flow law in the case of anisotropic porous media is not straightforward due to the strong coupling between the microstructure of the porous medium and non-linear effects induced by the inertial term in Navier-Stokes equations [Lasseux et al., 2011; Auriault et al., 2007].

**Determination of the permeability  $\mathbf{K}$  and the inertial parameter  $C_2$ .** In general, at the macroscopic scale, the fluid flow law through of porous medium requires the knowledge of two material parameters: the intrinsic permeability tensor  $\mathbf{K}$  and the inertial coefficient  $C_2$ . In practice, these parameters can be

- determined experimentally by performing well-designed experiments, such as Darcy's ones [Darcy, 1856].

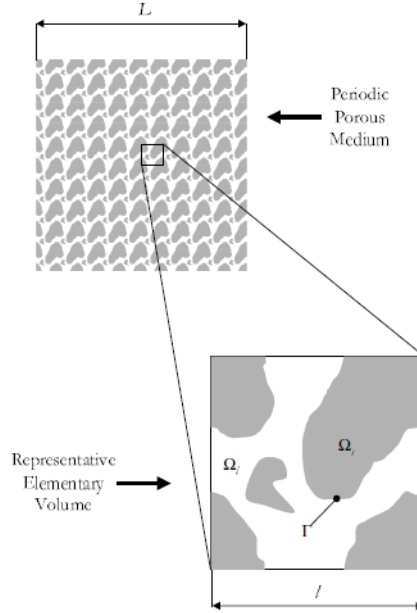


Figure 2.11: Schematic of separation of scale and the representative elementary volume (REV)

- computed from 3D images, by solving on a REV of the porous medium boundary value problems arising from upscaling techniques (see for example [*Boutin and Geindreau, 2010; Barbour, 2018; Auriault et al., 2009*]).
- estimated analytically by doing some hypothesis on the microstructure and using an upscaling method such as the self-consistent method (see for example [*Boutin and Geindreau, 2010*]).

In the context of coiled aneurysms treated as porous medium, the coils can be assimilated to a fibrous medium. We present here classical results concerning the permeability and inertial factor for fibrous media.

For example, Figure 2.12 shows the normalized intrinsic permeability of an array of parallel cylinders in the (a) transverse and (b) longitudinal directions, i.e.  $\mathcal{K}/R_s^2$ , as a function of the porosity.  $R_s$  is the radius of the cylinders. The self-consistent estimates P (continuous line) and V (dotted line) proposed by Boutin [*Boutin, 2000*] are compared with the numerical results obtained by finite element simulations on square (square) and triangular (black triangle) lattices of parallel cylinders [*Auriault et al., 2009*]. These two estimates are given by:

- in the longitudinal direction (subscript  $L$ )

$$\mathcal{K}_{pL} = -\frac{1}{2}[\log(\beta) + \frac{1}{4}(1 - \beta^2)(3 - \beta^2)](R_s/\beta)^2 \quad \text{P - estimate}$$

$$\mathcal{K}_{vT} = -\frac{1}{2}[\log(\beta) + \frac{1 - \beta^2}{1 + \beta^2}](R_s/\beta)^2 \quad \text{V - estimate}$$

- in the transversal direction (subscript  $T$ )

$$\mathcal{K}_{pT} = -\frac{1}{4} \left[ \log(\beta) + \frac{1 - \beta^4}{2(1 + \beta^4)} \right] (R_s/\beta)^2 \quad \text{P - estimate}$$

$$\mathcal{K}_{vT} = -\frac{1}{4} \left[ \log(\beta) + \frac{1 - \beta^2}{1 + \beta^2} \right] (R_s/\beta)^2 \quad \text{V - estimate}$$

where  $\beta^2 = 1 - \phi$ . This figure shows that the permeability of such porous media varies over several decades in the whole porosity range. When the porosity is large, typically larger than 0.6, the permeability of both lattices (triangular and square) are similar and in agreement with the P estimates.

*Tamayol et al.* [2012] analyzed the inertial factor numerically and experimentally for a fibrous porous medium. They determined the inertial factor numerically by solving the Navier-Stokes equation (2.17). Also, the inertial factor was determined by measuring the pressure drop (inflow and outflow) for flow perpendicular to a cylindrical bundle.

The results are plotted in Figure 2.13: the experimental and the numerical data, as well as the previous inertial factor values extracted from previous literature studies, are plotted. The value calculated is actually the Forchheimer coefficient ( $F$ ) were  $C_2 = 2F/\sqrt{K}$ . The proposed correlation of the Forchheimer coefficient in the porous media for flow normal to squared arrays corresponds to  $F = (-5.32 + 18.42\phi)^{-1/0.532}$ , where  $\phi$  is the porosity.

The results show that the values obtained numerically and experimentally are consistent with the proposed correlation. Forchheimer's coefficients vary between 0.13 and 0.009 for a porosity varying between 0.45 and 0.95, which corresponds to an inertial factor ( $C_2$ ) value varying between 4475 and 13  $\text{m}^{-1}$ , for a normal flow to the squared arrays of fibers where their diameter is equal to 1.5 mm.

### 2.2.3.3 Coupling methods for fluid-porous medium

In the coil-resolved model, the Navier-Stokes equations are solved in the parent vessel either in the pores of the coil within the aneurysmal sac. When the coil is replaced by an equivalent porous medium, the numerical model is constituted by two different regions, the fluid zone (i.e the parent vessel) in which the flow is still described by Navier-Stokes equations, and the porous domain (the aneurysmal sac with the coil) in which the flow is now described by Darcy's Law (or Forchheimer's law). To solve such problems numerically, different methods have been proposed and are currently used: the first one is the two domains approach and the second one is a single domain approach. These two approaches are briefly presented in the following. To illustrate such approaches, we will consider a steady-state slow flow and an isotropic porous medium. In that case, the flow in the parent vessel is given by the Stokes equations, and Darcy's law is valid in the porous medium.

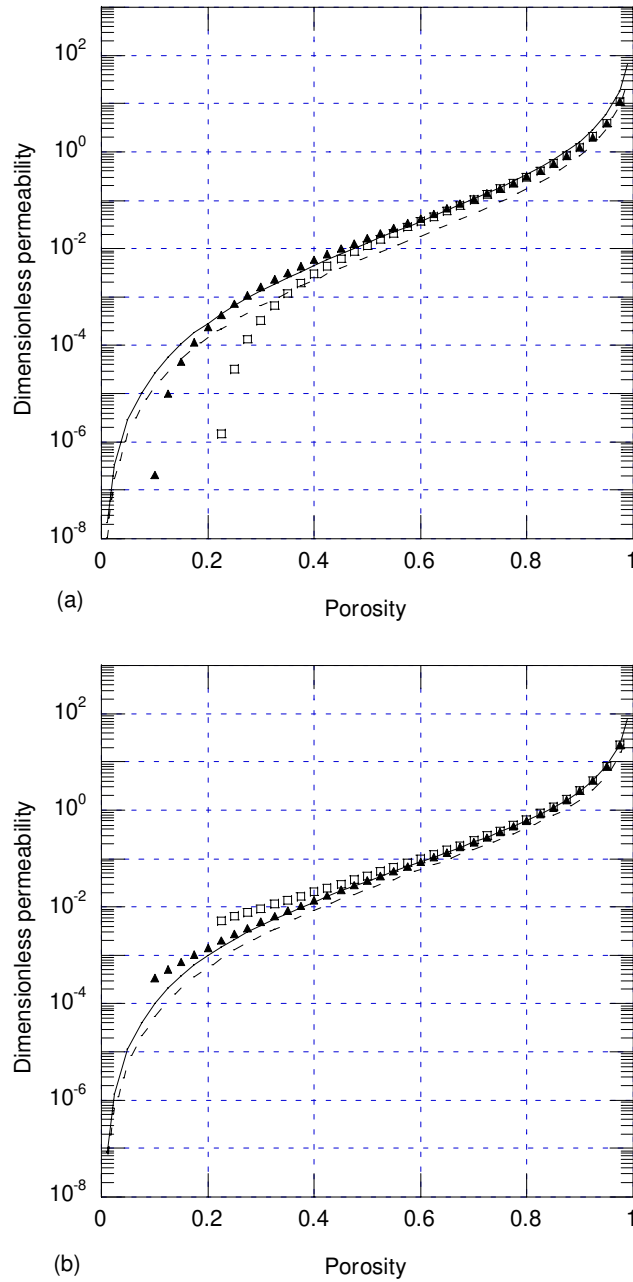


Figure 2.12: Normalized intrinsic permeability of an array of parallel cylinders in the (a) transverse and (b) longitudinal directions, i.e.  $\mathcal{K}/R_s^2$ , as a function of the porosity: the self-consistent estimates P (continuous line) and V (dotted line) are compared with the numerical results obtained by finite element simulations on square (square) and triangular (black triangle) lattices of parallel cylinders. [Auriault et al., 2009].

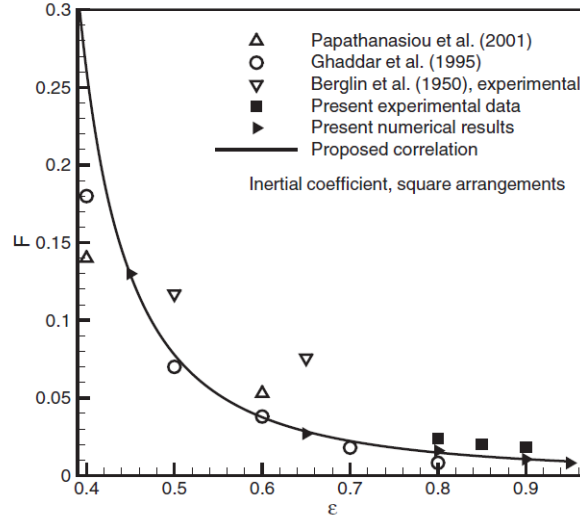


Figure 2.13: Comparison between the present numerical and experimental results for Forchheimer coefficient ( $F$ ) with experimental and numerical data of others. The figure shows the evolution of the Forchheimer coefficient ( $F$ ) with the porosity ( $\epsilon$ ). Source: *Tamayol et al.* [2012].

**Two-domains approach.** In this approach, the two different sets of equations for the fluid domain and the porous medium are solved and are coupled with suitable boundary conditions at the interface between the fluid domain and the porous domain (Figure 2.14). In the fluid domain, the fluid flow is described by the Stokes equations:

$$-\nabla p_f + \mu_0 \nabla^2 \mathbf{u}_f = 0 \quad \text{and} \quad \nabla \cdot \mathbf{u}_f = 0 \quad (2.17)$$

where  $p_f$  and  $\mathbf{u}_f$  are the fluid pressure and the fluid velocity respectively. In the porous domain, the flow is described by Darcy's law:

$$\nabla p_p = -\frac{\mu_0}{K} \mathbf{u}_p \quad (2.18)$$

where  $p_p$  and  $\mathbf{u}_p$  are the fluid pressure and fluid velocity (Darcy's velocity) respectively. At the fluid - porous domain interface, the conservation of mass across is written:

$$\mathbf{u}_f \cdot \mathbf{n} = \mathbf{u}_p \cdot \mathbf{n} \quad (2.19)$$

where  $\mathbf{n}$  is the normal vector to the interface. The only acting force at the interface from the porous medium is the fluid pressure. Therefore, the balance of normal forces can be read as:

$$p_f - \mathbf{n} \cdot (\mu_0 \nabla \mathbf{u}_f \cdot \mathbf{n}) = p_p \quad (2.20)$$

Beavers-Joseph, developed a velocity jump condition [*Beavers and Joseph, 1967*] and it is often used to connect the tangential free flow velocity and the seepage velocity in the porous medium:

$$(\mathbf{u}_f - \mathbf{u}_p) \cdot \mathbf{t} + \frac{\sqrt{K}}{\alpha_{BJ}} (\nabla \mathbf{u}_f \cdot \mathbf{n}) \cdot \mathbf{t} = 0 \quad (2.21)$$

where  $\alpha_{\text{BJ}}$  is the Beavers-Joseph parameter,  $\mathbf{t}$  is the unit vector tangential to the interface. This interface condition is required as an additional boundary condition for the Stokes domain because equations in two domains are in a different order.  $\alpha_{\text{BJ}}$  depends on the properties of the fluid and the structure of the permeable material. Saffman [*Saffman, 1971*] has proposed a modification of the Beavers-Joseph condition. The velocity in the fluid domain is higher than in the porous zone, therefore the velocity in the porous medium can be neglected in the jump velocity condition:

$$\mathbf{u}_f \cdot \mathbf{t} + \frac{\sqrt{K}}{\alpha_{\text{BJ}}} (\nabla \mathbf{u}_f \cdot \mathbf{n}) \cdot \mathbf{t} = 0 \quad (2.22)$$

Other coupling conditions have been investigated [*Hassanizadeh and Gray, 1989; Ochoa-Tapia and Whitaker, 1995; Chandesris and Jamet, 2006, 2009*], however, there isn't an agreement about the appropriate and definitive coupling conditions. The main challenge of this method is defining the coupling condition that represents the transport process at the interface.

**Single-domain approach** In this approach, only one set of equations is assumed valid in the whole domain (Figure 2.14). The coupling is done via a transition zone (either surface or zone) where the parameters are discontinuous or they vary. Brinkman's equation [*Brinkman, 1947*] is solved in the entire domain:

$$-\nabla \cdot (\mu_{\text{eff}} \nabla \mathbf{u}) + \frac{\mu_0}{K} \mathbf{u} + \nabla p = 0 \quad (2.23)$$

where  $\mu_0$  is the dynamic viscosity of the fluid and  $\mu_{\text{eff}}$  is the effective viscosity. This equation can be seen as a superposition of the Stokes equations and Darcy's law and needs to define the physical parameters inside the porous medium and the fluid domain. The advantage of this method is that no boundary conditions are required at the interface since the velocity and the stress continuity across the interface are satisfied with this method. In the fluid-porous transition, the physical parameters will vary (porosity and permeability), and the effective viscosity is introduced to ensure the transition between the two domains. Indeed, in the fluid domain, the permeability value  $K$  is infinite and  $\mu_{\text{eff}}$  tends towards  $\mu_0$ , whereas in the porous domain the permeability value  $K$  is finite and the term  $\nabla \cdot (\mu_{\text{eff}} \nabla \mathbf{u})$  becomes negligible. The challenge of this method is to determine the physical parameters in the transition zone, such as  $\mu_{\text{eff}}$  [*Goyeau et al., 2003; Rosenzweig and Shavit, 2007*]. Finally, let us remark that the Brinkman model is only applicable for high porosity ( $\phi > 0.6$ ) and is not valid in multiphase flows [*Rybak, 2016*].

### 2.2.3.4 Modeling aneurysm with coils as a porous medium

In the literature, few studies concern the modeling of aneurysm with coils as a porous medium [*Kakalis et al., 2008; Levitt et al., 2016; Mitsos et al., 2008; Yadollahi-Farsani et al., 2019*].

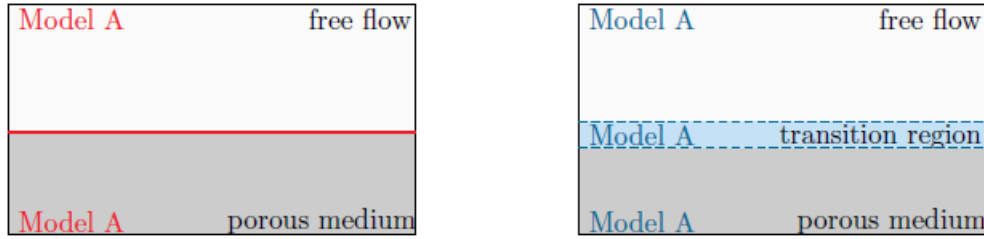


Figure 2.14: Schematic representation of the coupling methods: (left) The two domains approach with interface boundary conditions, (right) the single domain approach with a transition zone for the physical parameters. Source: Rybak [Rybak, 2016]

**Fluid flow law.** In some porous models, as in *Yadollahi-Farsani et al.* [2019], the non-linear effects were neglected and only Darcy’s law was considered for studying blood flow in treated aneurysms. However, in other studies, as in *Levitt et al.* [2016], *Kakalis et al.* [2008] and *Mitsos et al.* [2008], the fluid flow through the coils is described by Forchheimer’s law. This law seems appropriate since coil-resolved simulations have shown that the pore Reynolds number varies between 20 and 50 [Barbour, 2018], and for  $Re_p > 1$  the non-linear effects appear (see section 2.2.3.2). Up to date, due to the lack of knowledge about the coil microstructure (heterogeneity, anisotropy...) within the aneurysmal sac, coils are considered as homogeneous isotropic porous media where the permeability and inertial factors were calculated based on the mean porosity of the coil in the aneurysm.

**Permeability of the coil.** Concerning the permeability, *Levitt et al.* [2016] and *Kakalis et al.* [2008] used in particular a Kozeny Carman model to estimate the permeability:

$$K = \frac{\phi^3}{cS^2} \quad (2.24)$$

where  $c$  is the Kozeny coefficient, taken as 2 for cylinders,  $\phi$  the mean porosity, and  $S$  the specific surface area of the coil, i.e. the ratio of the interstitial surface area of the pores to the total volume. In *Levitt et al.*, the permeability values vary between  $3.02 \cdot 10^{-8} \text{ m}^2$  and  $2.4 \cdot 10^{-8} \text{ m}^2$  for a porosity varying between 0.797 and 0.818. In *Kakalis et al.* the permeability values vary between  $1.55 \cdot 10^{-8} \text{ m}^2$  and  $1.44 \cdot 10^{-6} \text{ m}^2$  for porosity values varying between 0.735 and 0.934. In these two works, they considered the diameter of the coils to be 0.25 mm. The majority of commercially available coils have a diameter of 0.25 mm and their length can strongly vary.

The permeability of the coils has been determined by using falling-head permeameter or fluorescent microspheres methods [*C.Sadasivan et al.*, 2018; *Chueh et al.*, 2015] and can be used to compare and validate the numerical models. In *Chueh et al.* [2015], the same aneurysm was printed in four silicone models and

each one was treated with the same number of coils, with a mean porosity of 0.657. The permeability was then measured with fluorescent microsphere techniques. It consisted on assessing the permeability values by measuring the ratio of microspheres passing through the coils over those in the fluid. The mean permeability values obtain for the four models was  $1.44 \cdot 10^{-8} \text{ m}^2$  for a mean porosity of 0.657. The values of permeability are consistent with the numerical Kozeny's Carman model. In *C.Sadasivan et al.* [2018], three idealized aneurysms with different diameters were treated with four different types of coils. The coils were made by different brands, they were done in different materials (three of them in bare metal and the forth in PGLA), and their diameters varied (0.254 mm to 0.508 mm). The permeability was measured using a permeameter, the models and the experimental setup can be found in Figure 2.15. The results show that the mean permeability is  $2.2 \cdot 10^{-10} \text{ m}^2$  for a mean porosity of 0.650. The permeability value is very low compared to the other studies. This deviation might be explained by the values used in their calculus of permeability. Sadasivan et al considered in the calculus of the permeability that the pore surface can be considered as the aneurysm surface. In the other numerical works, the permeability was calculated using the pore surface (see  $S^2$  in equation (2.24)). The pore surface is smaller than the aneurysm surface therefore the permeabilities values calculated using the aneurysm surface are smaller than the ones using the interstitial surface area of the pores. If we only focus on this study, Sadasivan et al show that for the same packing density different permeability values were obtained. Therefore the mean porosity in the aneurysm is not the only factor defining the permeability and the heterogeneity of the coils distribution needs to be considered for its calculus.

*Muschenborn et al.* [2013] compared experimental and numerical results by measuring the effective permeability and inertial factor experimentally for different packing levels. In this work, permeability values measured were compared with Kozeny Carman's model, and in particular, to the permeability used in *Kakalis et al.* [2008]. The experimental setup consists of a flow loop where a fluid circulates using a pump, and the permeability is calculated using the pressure gradient measured with two pressure transducers placed upstream and downstream of the sample chamber where the coils were deployed. The sample chamber is cylindrical. The experimental setup and the chamber can be found in Figure 2.16. The diameter of the coils was 0.1 mm. The permeability values vary between  $3 \cdot 10^{-7}$  and  $5 \cdot 10^{-6} \text{ m}^2$  for porosity values varying between 0.73 and 0.89. Figure 2.17 shows the results of the comparison: the experimental values of permeability are higher than the Kozeny Carman model. The difference between the experimental model can be due to the deployment of the coils creates randomness in distribution and it needs to be considered when calculating the permeability and inertial factor. Indeed, the diameter of the coils is not very small when being compared with the aneurysm dimensions, therefore the separation

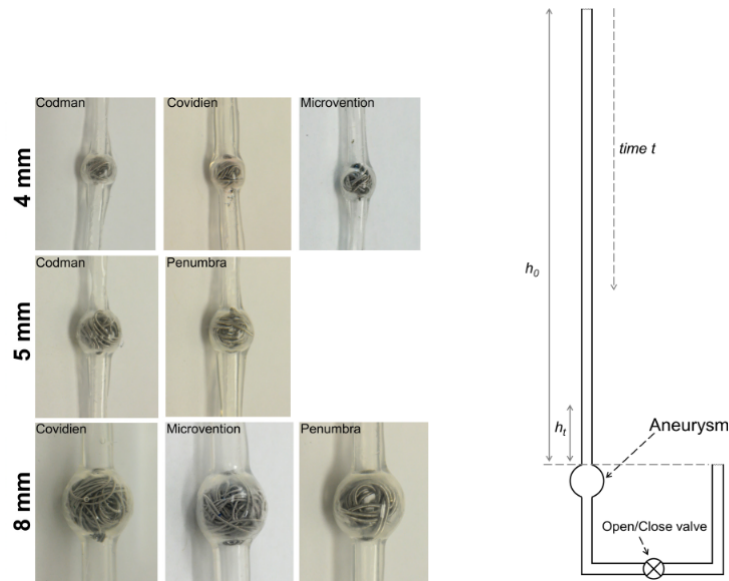


Figure 2.15: Left: Idealized in aneurysm models with diameters varying from 4 to 8mm and treated with different coils (Orbit Codman Neurovascular, Cosmos and Hypersoft Microvention Terumo, Axiom Bare and PGLA Covidien Medtronic, and Penumbra Coil 400).Right: Permeameter used in the experiment. Source: *C.Sadasivan et al.* [2018].

of scales law (2.12) is not well verified, and the border effect has a high impact on the blood flow in the treated aneurysms. Moreover, in this study, the sample chamber used is cylindrical and not representative of the aneurysm's anatomy. The coils used in the experiment are smaller than in Kakalis et al (0.1 mm versus 0.25 mm), which might impact the results too.

All these studies show that, up to date, there isn't any consistency between studies (numerical or experimental) in determining the permeability parameter to define the aneurysm treated with coils. Table 2.1 presents the permeability values obtained for each study and the associated porosity. Developing a methodology to define the permeability of the porous medium that considers the heterogeneity of the coils would be improve the numerical existing models. It is also necessary to create a methodology to validate the permeability value experimentally in the same conditions than in the numerical model.

**Inertial factor.** The non-linear part of the Darcy-Forchheimer law (2.16) is defined by the inertial factor. *Muschenborn et al.* [2013], estimated empirically the inertial factor using the setup presented before. They found that the inertial factor varies from 592 to 81.8  $\text{m}^{-1}$  for porosity values between 0.73 and 0.89. In *Levitt et al.* [2016], the values obtained experimentally were used. However in *Kakalis et al.* [2008] and *Mitsos et al.* [2008], the inertial coefficient was calculated as the ratio between  $C_D$  and  $\sqrt{K}$ , where  $K$  is the permeability and  $C_D$  is the drag factor. To calculate

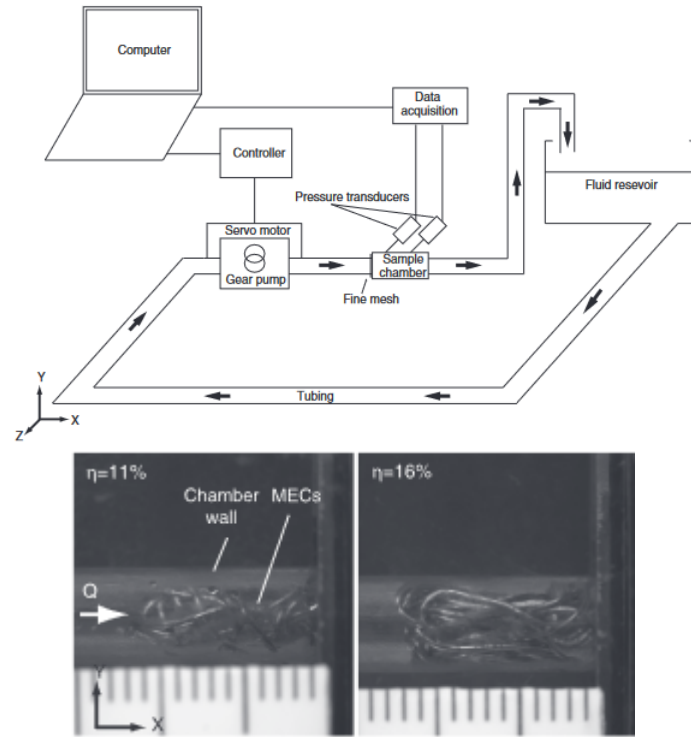


Figure 2.16: Up: Flow loop to measure the permeability. Down: coils deployed in the sample chamber. Source: *Muschenborn et al.* [2013]

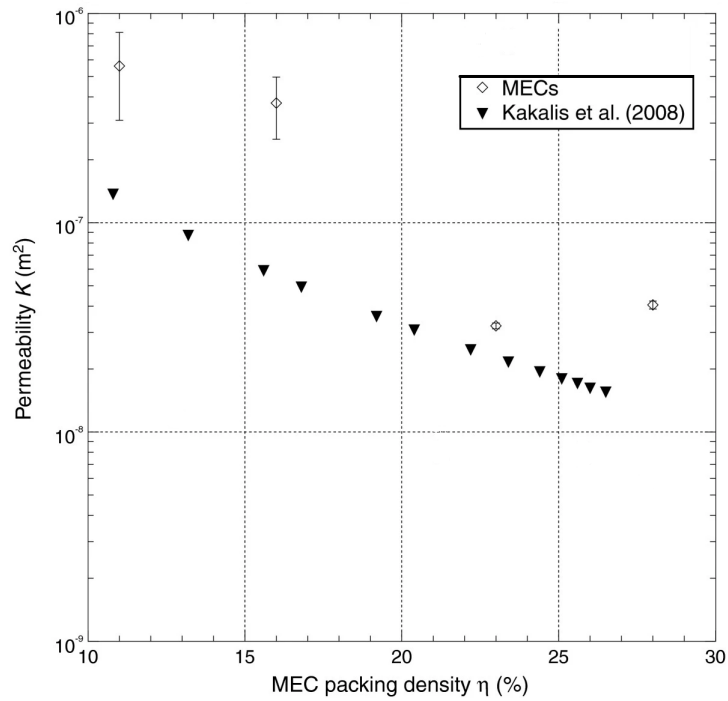


Figure 2.17: Measured permeability in embolic coils (MECs) compared to the calculated with Kozeny's model in *Kakalis et al.* [2008]. Source: *Muschenborn et al.* [2013]

Research group	Type of study	Coils diameter (mm)	Porosity (mean or range)	$K$ (m <sup>2</sup> ) (mean or range)	$C_2$ (1/m) (mean or range)
<i>Levitt et al.</i> [2016]	Numerical	0.250	[0.797,0.818]	[ $3.02 \cdot 10^{-8}$ , $2.4 \cdot 10^{-8}$ ]	[592,82]
<i>Kakalis et al.</i> [2008]	Numerical	0.250	[0.735,0.934]	[ $1.55 \cdot 10^{-8}$ , $1.44 \cdot 10^{-6}$ ]	[19093,3199]
<i>Chueh et al.</i> [2015]	Experimental	0.250	0.657	$1.44 \cdot 10^{-8}$	NA
<i>C.Sadasivan et al.</i> [2018]	Experimental	[0.254, 0.508]	0.650	$2.2 \cdot 10^{-10}$	NA
<i>Muschenborn et al.</i> [2013]	Experimental	0.1	[0.73,0.89]	[ $3 \cdot 10^{-7}$ , $5 \cdot 10^{-6}$ ]	[592,82]

Table 2.1: Summary of the permeability and inertial factor values obtained in the literature in numerical and experimental studies

$C_D$  the flow was assumed perpendicular to an infinite cylinder locally, and then  $C_D$  was determined with a standard  $C_D$  versus  $Re$  diagram [Achenbach, 1971], taken  $C_D = 2.2$ . The values of an inertial factor in those studies vary between 19093 and 3199 m<sup>-1</sup> for porosity values varying between 0.735 and 0.934. There is a factor of 100 between the experimental and the numerical results. In the numerical model, the heterogeneity of the porosity wasn't considered either in the calculus of the inertial factor. There is only a few studies on the topic and the values of the inertial factor taken are very different from one model to another. The results of the inertial factor are summarized in Table 2.1.

**Numerical methods.** All the porous model studied used the Finite Volume Method to model blood flow in cerebral aneurysms with different software in each case and all the cases solving the problem of porous/fluid coupling using a one domain approach [Yadollahi-Farsani et al., 2019; Levitt et al., 2016; Mitsos et al., 2008; Kakalis et al., 2008]. All the porous models consider that the blood is an incompressible and Newtonian fluid and the wall is considered rigid as the impact of the movement of the artery wall is minor for these problems.

All the models use patient-specific anatomies for the 3D geometry obtained from scans. However, the boundary conditions vary from one study to another. *Kakalis et al.* [2008] and *Mitsos et al.* [2008] used constant velocities in the inlet. For those studies, which objective was to assess hemodynamic impact when increasing the number of coils, the simplified boundary conditions were enough, however, it cannot be used to assess the validity of the porous model as it doesn't consider the variations of the cardiac cycle. *Yadollahi-Farsani et al.* [2019], present a variation of this

method: the velocity is constant at the inlet but different simulations were done varying the Reynolds number at the inlet from 0.5 to 10. These methods allow to include the variation of the inertial effect for different Reynold number values, however, it doesn't consider biofidelic inflow data.

*Levitt et al.* [2016] used patient-specific boundary, with the data acquired during the patients' surgery (see section 2.2.2.2). A Womersley profile was imposed at the inlet and a zero pressure condition at the outlet. Three cardiac cycles were run and only the last one was considered. This methodology is very complete as it combines velocities profiles varying from one patient to another which have been proved to improve the analysis.

Different hemodynamic factors have been studied from these numerical simulations. *Kakalis et al.* [2008] and *Mitsos et al.* [2008] analyzed the velocities distribution, the pressure distribution in the aneurysm walls, and the pathlines. *Levitt et al.* [2016] analyzed the mean blood flow in the aneurysm as well as the wall shear stress (WSS), the wall shear stress gradient (WSSG), and the oscillatory shear index (OSI). When modeling porous model, the parameters compared in the porous media versus at the resolved geometry need to be in the same scale. This means that, when the aneurysm with coils is assimilated to a homogeneous porous media, only the mean values at the aneurysm scale can be analyzed. Indeed, we cannot use WSS values to compared the coil-resolved simulations and the porous medium approximation. In these studies, they used local values to analyze the hemodynamic in the aneurysm, therefore the results might not be accurate to validate the biofidelic model. *Yadollahi-Farsani et al.*, on the other hand, calculated the pressure drop between the inlet and outlet of their system, and as well as the kinetic energy. These parameters evaluated can be used to analyze the blood flow in the aneurysm as they are mean vales that can be calculated at the aneurysm scale.

**Main results and conclusion.** In *Kakalis et al.* [2008] and *Mitsos et al.* [2008], the purpose was to analyze how the hemodynamics parameters were impacted a different number of coils in the aneurysm. The results show that the blood pathlines are modified when increasing the number of coils, as well as a reduction in the pressure in the aneurysmal wall and creating stagnation zones. This work presents a major advance in the understanding of blood flow in cerebral aneurysms treated with coils. However, the porous model wasn't validated using any coil-resolved or experimental model, therefore the validity of the porous model couldn't be evaluated.

In *Levitt et al.* [2016], the mean blood flow in the coiled aneurysm comparing the porous model with the coil-resolved model (see section 2.2.2) after running patient-specific simulations. The coil-resolved model was taken as a reference. The results show that, when comparing the mean blood flow between the coil-resolved and the porous model, there was a difference of 28.68% and 89.56% for the two patients.

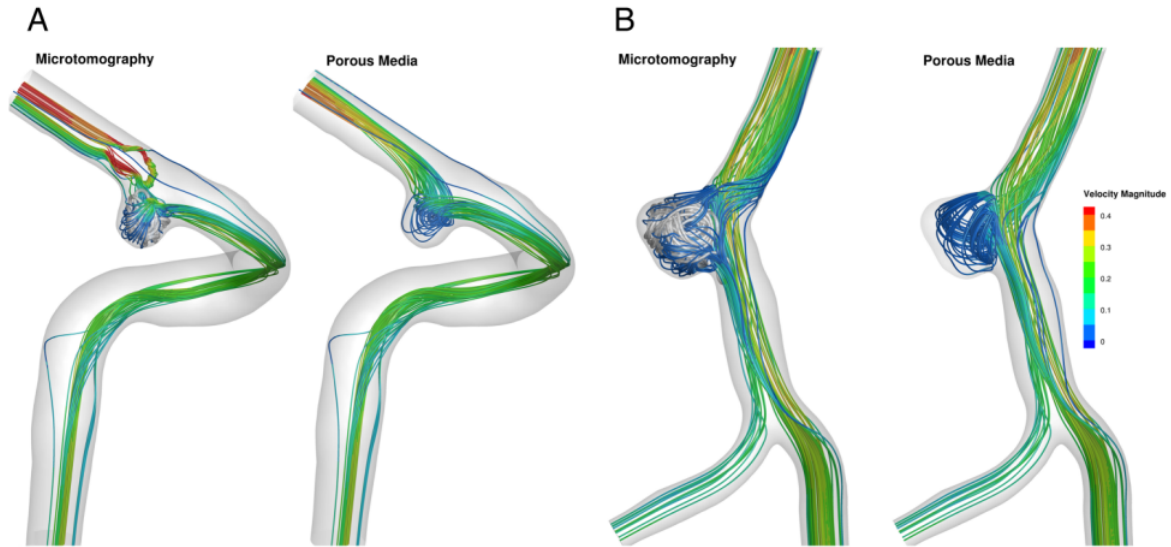


Figure 2.18: Levitt et al results of streamlines at systole: comparison between porous model and coil-resolved model for two patients [Levitt *et al.*, 2016]

In both cases, the homogeneous isotropic porous model developed overestimates the blood's velocity in the aneurysm. Some of the results of this study are illustrated in Figure 2.18 which shows that the coil-resolved model present more complex pathlines than in the porous model. These results show that the permeability and inertial factor model estimated from the mean porosity of the coils are not adapted to reproduce blood flow in the coiled aneurysm.

*Yadollahi-Farsani et al.* [2019] compared the homogeneous isotropic porous media to a biofidelic model using the geometry of the coils by being deployed in the aneurysm by software. The results show that the kinetic energy is overestimated in the homogeneous porous model by 268, 414, and 98.07% for the three patients studied. These results are consistent with the *Levitt et al.* [2016] study, therefore we can conclude that the porous media model where the permeability is based in the mean porosity using Kozeny Carman model overestimates the velocity and cannot be used to model blood flow in the treated aneurysm.

Including the heterogeneity of the porous media, the distribution would improve the porous model. The first steps have been done towards solving this problem in *Yadollahi-Farsani et al.* [2019]. In that work a porosity map was created: the aneurysm with coils was divided into a grid of different resolutions. The porosity and permeability were calculated for each one of those elements using the Kozeny Carman model. As for the homogeneous model, the kinetic energy was calculated in the different resolved porous models and compared to the biofidelic coil-resolved results. The porous map at different resolutions for three patients is illustrated in Figure 2.19. The results show that prediction improves when considering the

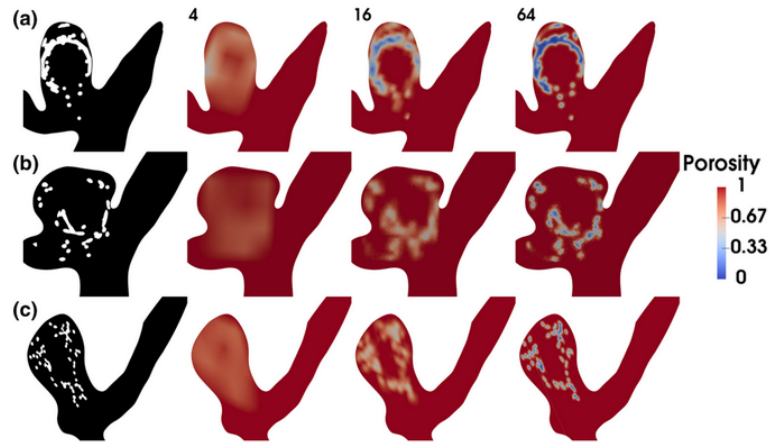


Figure 2.19: Yadollahi-Farsani et al porous map at different resolutions for 3 patients [Yadollahi-Farsani et al., 2019]. The first column presents the coil-resolved model. The three right columns present the porous map at different resolution with the number on each column being the number of hexahedra in each axial direction.

heterogeneity. Indeed the kinetic energy absolute errors, for the 64 hexahedra mesh each axial direction were 9.25, 1.87, and 1.92% for the three patients (see Figure 2.19 column in the right). This presents an improvement when compared to the homogeneous modeling approach. However, the porosity and permeability of this porous model were determined based on the coil-resolved geometry, therefore this model cannot be used for prediction since the geometry of the coils is necessary to define the heterogeneous porous model.

### 2.3 Concluding remarks

Here are some concluding remarks based on the literature review that is important for our study:

- Hemodynamics has been related to growth and rupture of the aneurysm. Therefore, modeling blood in the aneurysm treated with endovascular coils allows the study of hemodynamics, and it can be used to determine the parameters related to recanalization. The purpose is also to develop a numerical model that could be used for the prediction of the treatment outcome in the neuro suite.
- The existing numerical models using the geometry of the coils can be considered as the biofidelic models (coil-resolved model). However, the process to obtain the geometry of the coils is long and expensive, and the computational time of the computational fluid dynamic simulations is very high. Also, none of

the coil-resolved existing models have been validated experimentally. They couldn't be used for prediction.

- Modeling the aneurysm with coils as porous media could solve this problem. To define the porous media, the permeability and inertial factor need to be defined. There is high variability in the permeability for aneurysms treated with coils in the literature (experimental and numerical studies). Therefore, there is no agreement on how to define porous media nowadays.
- The numerical porous models developed up to date are simplistic: the permeability and inertial factor are only defined based on the mean porosity. The results of the comparison between porous media and coil-resolved have shown that the porous media which definition is only based on the mean porosity are not accurate enough.

The purposes of this work are to validate experimentally the coil-resolved model and to propose a biofidelic porous medium model that could be used for the prediction of the treatment outcome. This research is in continuity with the previous research work done at the University of Washington. The methods developed by *Barbour* [2018] were used in this study, for patient-specific data acquisition and developing a computational model.

---

## Residence time analysis on cerebral aneurysms treated with coils using planar-laser-induced fluorescence and computational fluid dynamics

### Contents

---

3.1	Introduction . . . . .	43
3.2	Methods . . . . .	44
3.2.1	Model creation . . . . .	44
3.2.2	Planar-laser-induced fluorescence . . . . .	46
3.2.3	Computational Fluid Dynamics . . . . .	49
3.3	Results . . . . .	52
3.3.1	PLIF results . . . . .	52
3.3.2	Comparison with coil-resolved simulations results . . . . .	56
3.4	Discussion . . . . .	59
3.5	Conclusion . . . . .	61

---

### Abstract

Biofidelic numerical models have been developed such as the coil-resolved model to study hemodynamics in the treated aneurysm. In this model, the geometry of the coils is recreated from high-resolution tomography scans of a phantom aneurysm treated with coils. However, this model hasn't been validated. The purpose of this work is to validate the coil-resolved model. To achieve this, we used the planar-laser induced fluorescence technique on phantom aneurysm treated with coils and measured the residence time and the evolution of rhodamine concentration during the washout. We run passive scalar simulations with the coil-resolved model and measured the evolution of concentration over time. The comparison of the numerical and the experimental results shows that the coil-resolved model reproduces the hemodynamics of

the experimental setup. Therefore it can be used as a reference to study hemodynamics in the treated aneurysm or to validate porous media models developed for treatment outcomes prediction.

### 3.1 Introduction

Cerebral aneurysms (CA) are often treated with endovascular coiling. This technique is preferred due to its non-invasiveness and shorter post-operative recovery time for patients, compared to craniotomy surgery. It consists of deploying platinum coils inside the aneurysmal sac, slowing down blood flow into the aneurysm and inducing thrombus formation. The aneurysm is then isolated from the stresses associated with blood flow, reducing the risk of wall rupture and subarachnoid hemorrhage [Guglielmi *et al.*, 1991; Piotin *et al.*, 2007]. The number of coils placed inside the aneurysm depends on the aneurysm anatomy, with the objective to fill 30% of the aneurysm volume. Thrombosis, however, is not always complete [Crobeddu *et al.*, 2013]. Recanalization can lead to high risk of continuous growth of the aneurysm and potential rupture. There are factors of the coil deployment inside the aneurysmal sac, like porosity, that have been investigated to define the probability of success of the treatment. However, these parameters do not provide a global predictive metric for stable thrombus formation after treatment, and there is currently no agreement on how to predict the success or failure of the treatment.

Research on this problem has focused on numerical modeling of blood flow in the cerebral aneurysm. Hemodynamics has been strongly connected with aneurysm growth and rupture [Meng *et al.*, 2007]. Determining which hemodynamics factors are involved in thrombus formation, and how it can be the first step towards prediction of treatment outcomes [Damiano *et al.*, 2015]. Numerical models of the coiled aneurysm, such as developed by Levitt *et al.* [2016], accurately represents the physiology, and can be used to determine parameters linked with recanalization. This coil-resolved model reproduces patient-specific boundary conditions, and uses the exact geometry of the coils, which cannot be obtained from a clinical scan. It represents an improvement on current numerical modeling that has been attempted to use in translational settings, but hasn't been validated experimentally (*in vivo* or *in vitro*). Studying hemodynamics experimentally in coiled aneurysms presents a significant challenge and hasn't been documented in the literature. Indeed, the coils produce artifacts on most imaging modalities and, due to its opacity, reduce the field of view and accuracy when visualizing blood flow *in vivo*.

Thrombus formation is linked with low blood velocity and stagnation in the aneurysmal sac. Residence time in the aneurysm can be a useful parameter to determine the future development of thrombosis. It is expected that a high residence time will lead to a stable thrombus formation, and better treatment outcomes.

Previous studies have used planar laser-induced fluorescence (PLIF) to measure concentration of species over time in *in vitro* experiments [Barbour *et al.*, 2015b, a]. This technique could allow to visualize the washout out in a aneurysm treated with coils, using a fluorence dye and following the evolution of its concentration in the aneurysm over time, and to measure residence time in the treated aneurysm.

The aim of the present work is to determine residence times for a small cohort of patients, both numerically through computational fluid dynamics and experimentally through planar laser-induced fluorescence (PLIF). The second objective is to evaluate the consistency of the results between the two methods, validating the coil-resolved computational model.

## 3.2 Methods

### 3.2.1 Model creation

Six patients were enrolled in this study at the University of Washington’s Harborview Medical Center in Seattle, WA, USA. They all presented cerebral aneurysms and were treated endovascularly with coils (Stryker Endovascular, Kalamazoo, Michigan, USA). All coils had the same diameter,  $240 - 250 \mu\text{m}$ , with lengths between  $2 - 30$  cm. Each patient received a different treatment (number of coils and lengths) based on the anatomy and the neurosurgeon’s judgment. For each patient, the parent vessel and the aneurysm were imaged using three-dimensional rotational angiography. After image segmentation, a numerical 3D model of the aneurysm and the parent vessel was created for each patient. A silicone model, at 1:1 scale, was built in acrylonitrile butadiene styrene with 3D printing technology. The silicone model was then cast in a clear polyester resin (PDMA, Clear-Lite; TAP plastics, San Leandro, California, USA) [Venkat *et al.*, 2019]. This transparent model was treated with the same set of coils as the patient; the same surgeon performing the surgery in the patient placed the coils in the models, in the same order and with the same specifications as those received by the patient. The aneurysm volumes can be found in Table 3.1: patients E and F present small volumes, C and D medium volumes and G and H large volumes. Having a large sample of aneurysm volume can help us understanding how the volume of the aneurysm impacts residence time.

Coils cannot be accurately imaged in a clinical scan, therefore, the coils placed in the silicone model were imaged with high-resolution tomography, avoiding beam hardening artifacts, at the European Synchrotron Radiation Facility (beamline ID19, ESRF, <http://www.esrf.eu>). The six models were imaged at a resolution of approximately  $13 \mu\text{m}$ . After the treated models were scanned, the coils were segmented from the reconstructed 3D images using ImageJ [Schindelin *et al.*, 2012], and the surface of the coils was extracted as a mesh (stl format). The process from

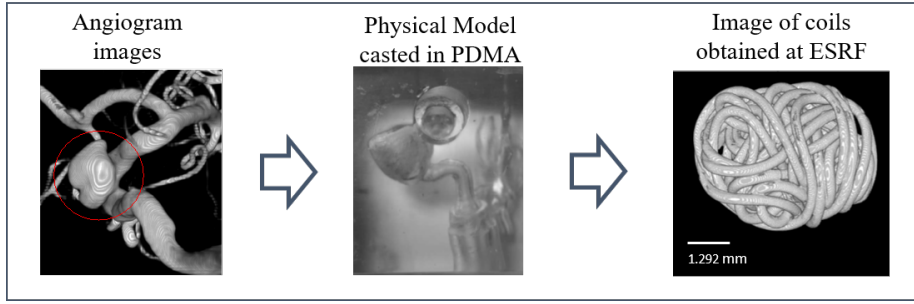


Figure 3.1: Main steps of the image acquisition: from the angiographic image on the top, to the coils ESRF scans.

the patients' medical images to coil surface Synchrotron images is shown in Figure 3.1.

The coils' surface geometry from the synchrotron images was used to create a numerical model of the aneurysm and parent vessel treated with coils for CFD analysis. The coil surface was positioned in the numerical 3D model of the aneurysm and parent vessel (from the CT scans). The process involved extracting the centerline of the parent vessel in the numerical 3D model and the 3D synchrotron images. The centerlines were extracted using Vascular Modeling Toolkit software (<http://www.vmtk.org>). The iterative closest point method [Wilm, 2020] allowed us to find the rotation and translation matrices between the centerlines of the parent vessels (numerical and synchrotron models). These same matrices were applied to the geometry of the coils, resulting in a numerical coil-resolved model that reproduced exactly the geometry of experimental model (phantom artery treated with coils) placed in the same reference frame as the pre-treatment scan of the parent vessel lumen. The coil-resolved models obtained in this study are shown in Figure 3.2.

Patient	Aneurysm volume (mm <sup>3</sup> )	$\phi_m$	$V_{pore}$ (mm <sup>3</sup> )
C	93.8	0.772	72.4
D	90.0	0.715	64.3
E	32.9	0.678	22.3
F	38.2	0.720	27.5
G	413.3	0.795	328.5
H	279.9	0.788	220.6

Table 3.1: Volume of the aneurysm, mean porosity ( $\phi_m$ ), pore volume for Patients C to H

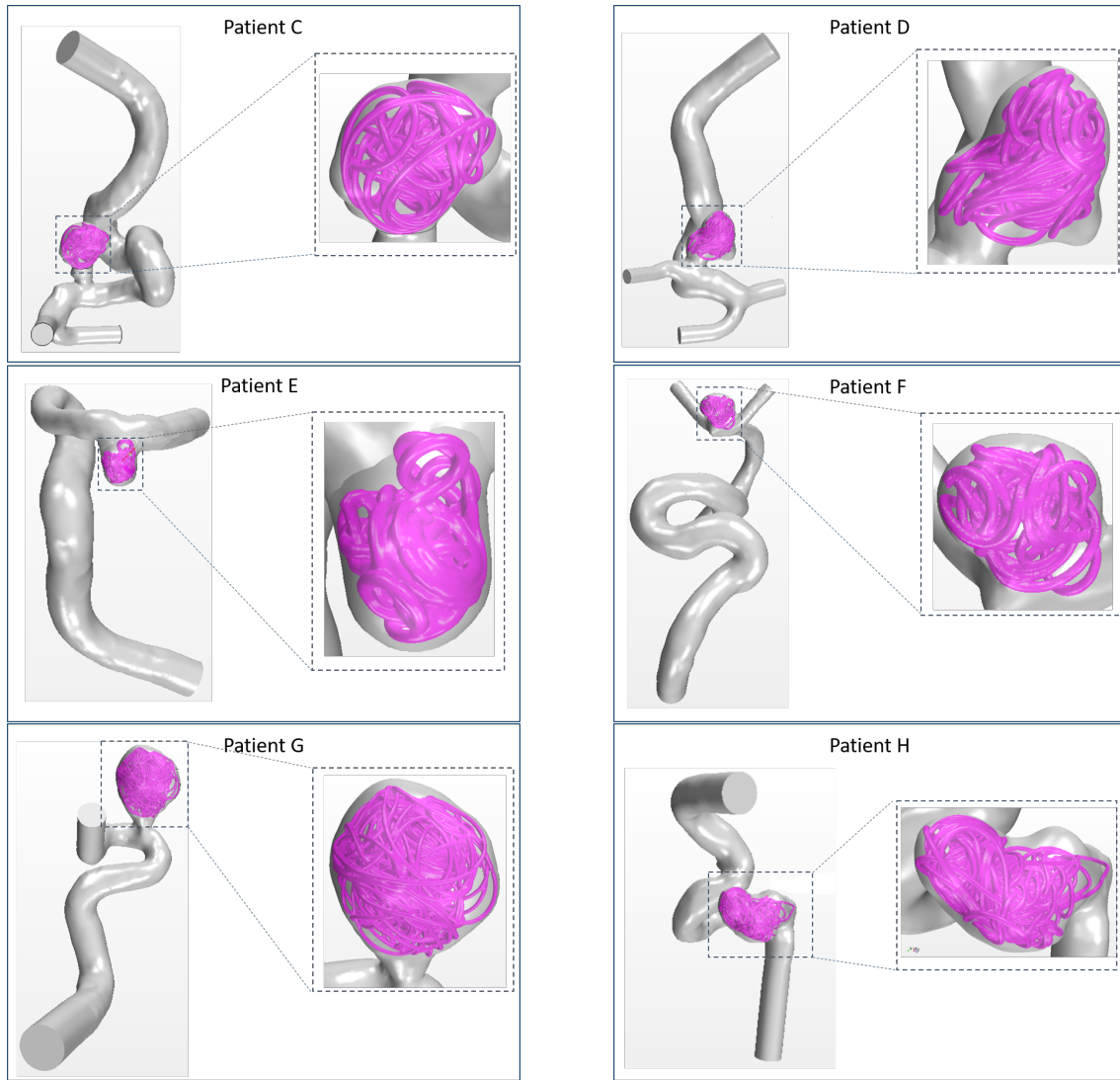


Figure 3.2: 3D models of the patients after coils reposition.

### 3.2.2 Planar-laser-induced fluorescence

#### 3.2.2.1 Experimental set up

For the experiment, the phantom artery was connected to a flow loop that reproduced the parent vessel hemodynamics (see Figure 3.3). The flow loop consisted of a reservoir placed above the experiment, to avoid air entrainment in the flow loop. A pulsatile pump (Harvard Apparatus, Boston, MA, USA), mimicking the waveform in the aneurysm parent artery, pumped the working fluid through the system. A resistance and capacitance were placed downstream from the pump to reproduce the effect of the cardiovascular system. The pump settings, resistance, and capacitance were adjusted so the volumetric flow rate at the parent vessel in the imaging test section was  $Q_{mean} = 200 \text{ mL/min}$  and  $Q_{systole} = 2Q_{mean}$  [Ford *et al.*, 2005]. The heart rate set for the pulsatile pump was 55 BPM, with a ratio of duration for systole/diastole

of 40/60. The flow rate was measured with an ultrasonic flow meter (Titan, Dorset, UK). The phantom artery was placed downstream from the flow meter. The tubes and fittings were adapted for each model depending on the patient's anatomy (one or multiple outlets). However, the rest of the boundary conditions were the same for all patients. The working fluid (a transparent solution of 47.5% water, 35.8% glycerol, and 16.7% NaCl) was chosen to match the viscosity of blood (3.8 cp) and the index of refraction of the silicone, avoiding any refraction artifacts in the images.

A solution of rhodamine B in the working fluid, at a concentration of 5 ppm, was created and injected in the aneurysmal sac prior to the start of the experiment. To visualize the initial fluid washout from the aneurysm sac, measuring the residence time of blood in the aneurysmal sac, the rhodamine B solution that filled the aneurysm was illuminated by a laser at the frequency of excitation of rhodamine B (Coherent Genesis STM CX Laser at 532 nm) and visualized with a high-speed camera. The laser light was shaped into a plane, focusing the beam into a thin beamline and expanding into a plane (1.1 mm thickness) using cylindrical and spherical lenses. The high-speed camera focal axis was perpendicular to the laser plane. Further details of the imaging technique are presented in the next section.

The experiment was primed by injecting the rhodamine B solution into the aneurysmal sac, slowly through a needle that was placed in the sac through the walls of the model (not the parent vessel) avoiding disturbances in the aneurysmal sac, confirmed by imaging prior to the start of flow. Once the aneurysm was filled, the pump was turned on and the physiological flow in the parent vessel was started, with some of it entering the aneurysmal sac and pushing out some of the dyed fluid that filled the sac initially. The full process of washout of the rhodamine solution was recorded by high-speed camera.

Figure 3.3 illustrates the flow loop and the optical setup, where the arrows illustrate the flow direction. Figure 3.4 shows the phantom artery for Patient G, with the arrows representing inflow and outflow, the aneurysm treated with coils, and the needle through which the rhodamine was injected.

### 3.2.2.2 Image acquisition and processing

A high-speed camera (Phantom v711, Vision Research, Trenton, NJ) captured the fluorescent light emitted by the rhodamine B dye after being excited by the laser light. A band-pass filter was placed between the camera and the artery phantom to remove the reflections of incident light. The rate of image acquisition and length of time captured in the experiments depended on the size of the aneurysm, varying between 70 seconds at 100 fps (for the largest aneurysm) and 14 seconds at 500 fps (for the smallest aneurysm).

The images recorded were treated with ImageJ [*Schindelin et al.*, 2012]. First, the

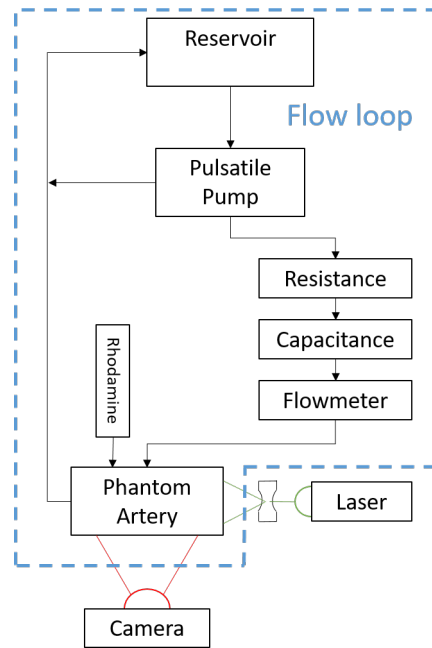


Figure 3.3: Schematics of the optical set up and the flow loop

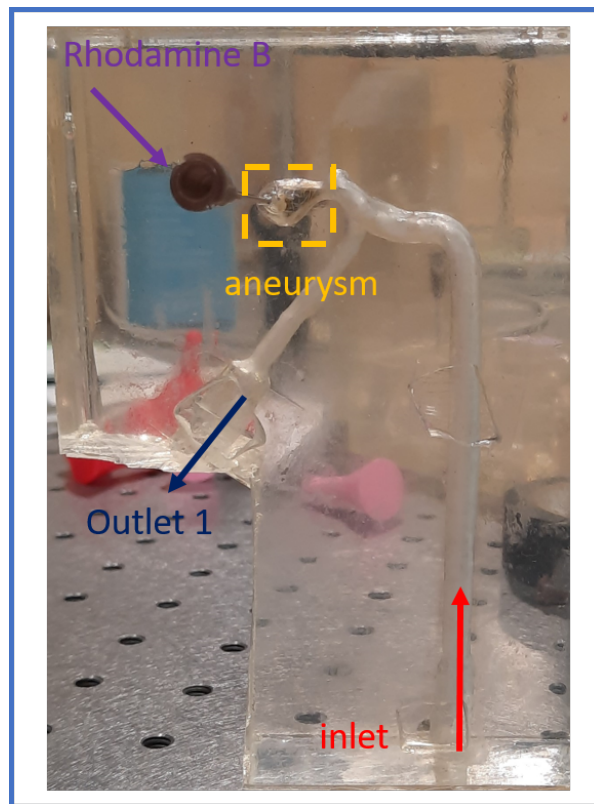


Figure 3.4: Silicone model patient G.

last image, for which the washout was completed, was subtracted from all the images to remove the signal from the coils and other spurious reflections that had gone through the band-pass filter. Then, the image intensity was thresholded to segment the sections where rhodamine B was present and those clear of fluorescent dye. This image-processing operation also limited the artifacts created by the presence of coils. The aneurysm was defined as the convex envelope of the coils. The rhodamine B that could have leaked into the parent vessel during injection was excluded from the analysis by the aneurysm envelope segmentation, before calculating the concentration of rhodamine. The analysis of the residence time was done using Matlab (Mathworks Inc., Natick, MA). The overall volume of rhodamine in the image sequence was calculated as the sum of the total pixel intensity values within the image, normalizing the overall intensity integrated value in the first image to 100%. The residence time was defined as the time at which the volume of rhodamine in the aneurysm first decayed by 99%, that is when it reached 1% in the normalized intensity integration. The process for image analysis is outlined in Figure 3.5.

### 3.2.3 Computational Fluid Dynamics

The coil-resolved computational model used the experimental study for validation. From each of the six patients, residence time was calculated using the finite volume flow simulation. The reconstructed geometry detailed in previous sections (see Figure 3.2), was meshed with a tetrahedral mesh. The element size of the parent vessel was  $200 \mu\text{m}$  and the element size at the surface of the coil was  $20 - 40 \mu\text{m}$ . This process was performed using StarCCM+ [Levitt *et al.*, 2016].

Blood was modeled as an incompressible Newtonian fluid, with viscosity equal to  $0.0035 \text{ Pa}\cdot\text{s}$  and density equal to  $1050 \text{ kg}/\text{m}^3$  [McGah *et al.*, 2011]. The software used for this analysis was Fluent (ANSYS, Release 17.1; ANSYS, Canonsburg, Pennsylvania, USA). In the following section, we describe the method for the numerical simulation of the physics and the boundary conditions used in the simulations.

#### 3.2.3.1 Physics

The Navier-Stokes equations were integrated numerically to simulate the blood flow in the aneurysms and the convective-diffusive transport of the dye:

$$\rho \left( \frac{\partial \mathbf{u}}{\partial t} + \mathbf{u} \nabla \mathbf{u} \right) = -\nabla p + \mu \nabla^2 \mathbf{u} \quad \text{and} \quad \nabla \cdot \mathbf{u} = 0 \quad (3.1)$$

where  $\rho$  is the blood density and  $\mu$  the blood viscosity,  $\mathbf{u}$  and  $p$  are the fluid velocity and the pressure respectively. To study residence time in the aneurysm treated with coils, the results of the experimental model were compared with the ones of the numerical model. In the experimental study, the aneurysm was filled with rhodamine,

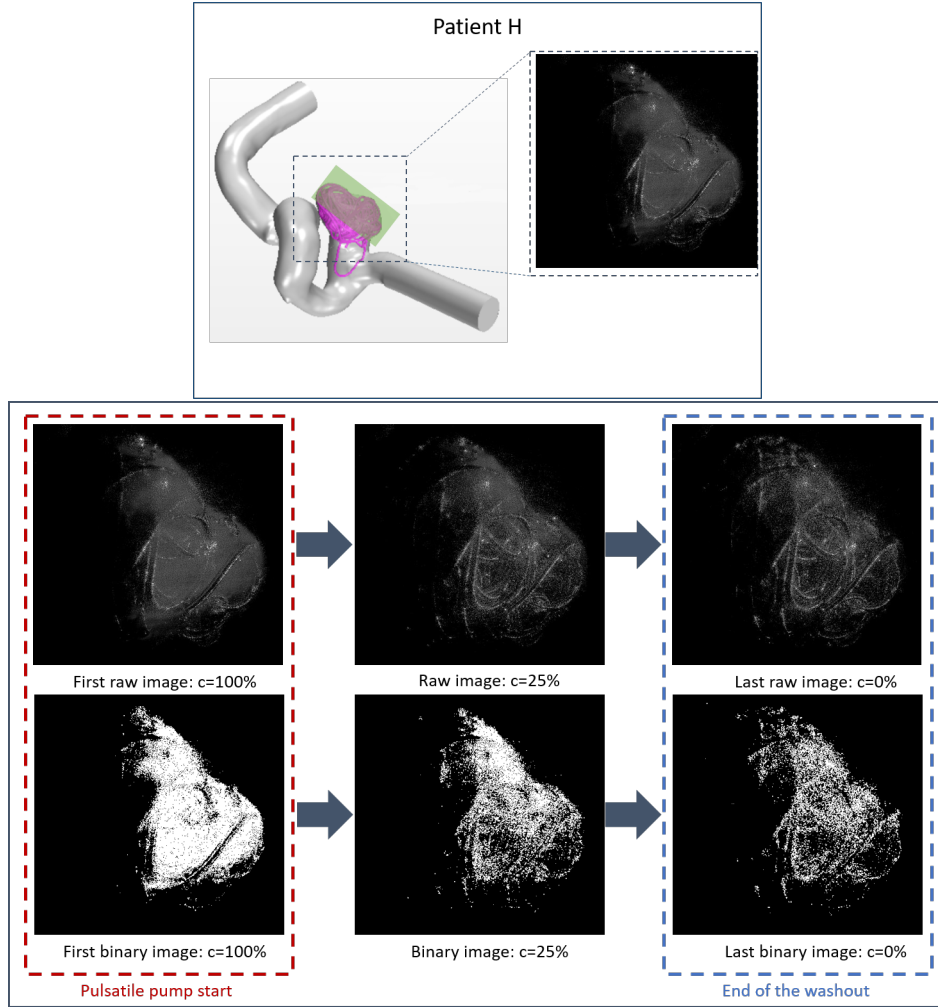


Figure 3.5: Patient H image treatment: on the top, the 3D model of Patient H with the green plane that is equal to the images obtained through PLIF. On the bottom left the images (raw and binary) before starting the pulsatile pump, when the aneurysm is filled with rhodamine B ( $c=100\%$ ). On the middle, at  $c=25\%$ , and on the right (raw and binary) at the end of washout ( $c=0\%$ ).

and to calculate the residence time, the concentration of rhodamine was calculated during the washout.

The concentration of rhodamine during the washout can be modeled with the transport equations for incompressible flow:

$$\frac{\partial c}{\partial t} = D\nabla^2 c - \mathbf{u} \cdot \nabla c \quad (3.2)$$

where  $c$  is the concentration of a passive scalar, and  $D$  its diffusivity. In Fluent (ANSYS, Release 17.1; ANSYS, Canonsburg, Pennsylvania, USA), the energy equation is used to model the mass transport of dye, with temperature playing the role of the dye as a passive scalar. This allowed the simulation to be compared with the experimental study. The diffusivity of rhodamine in water at  $21.5^\circ\text{C}$  is  $D_R = 3.6 \times 10^{-6} \text{ cm}^2 \cdot \text{s}^{-1}$ ,

and this value is used for the thermal conductivity in the CFD simulations.

The energy equation formulation solved in this work is:

$$\frac{\partial}{\partial t}(\rho(c_p(T - T_{ref}) + \frac{\mathbf{u}^2}{2})) + \nabla \cdot (\rho \mathbf{u}(c_p(T - T_{ref}) + \frac{p}{\rho} + \frac{\mathbf{u}^2}{2})) = \nabla \cdot (k_R \nabla T) \quad (3.3)$$

The term in the right part of the equation represents conduction (passive scalar diffusion). Viscous dissipation was not considered in the equation as there are no sources for the passive scalar in the experiments.  $T$  is the temperature, which plays the role of the dye concentration as the passive scalar in the aneurysm and  $T_{ref} = 100$  K. The thermal conductivity  $k_R$  ( $W/(m.K)$ ) was deduced from

$$D_R = \frac{k_R}{\rho c_p} = 3.6 \times 10^{-6} cm^2.s^{-1} \quad (3.4)$$

where  $\rho = 1050$  kg/m<sup>3</sup> and  $c_p$  the specif heat capacity of water  $c_p = 4184$  J.kg<sup>-1</sup>.K<sup>-1</sup>. The diffusivity is very low for the rhodamine B in water, resulting in very high Péclet number even in this moderately low Reynolds number flows ( $\approx 10$ ), therefore diffusive effects are minor for these simulations.

### 3.2.3.2 Boundary conditions and residence analysis

The boundary conditions in the CFD model were patient-specific. At the inlet, a pulsatile Womersley velocity flow was imposed, reconstructed from measurements performed *in vivo* by the surgeon using a dual-sensor Doppler guidewire (ComboWire and ComboMap; Volcano Corp, San Diego, California, USA). Those measurements were used to reproduce a pressure condition for the patients in the outlets. For patients with only one outlet, a zero-pressure condition was imposed in the outlet. For patients with multiple outlets, Resistance-Capacitance conditions were used. The arterial wall and the surface of the coils were considered rigid with a non-slip boundary condition.

In the experimental study, the boundary conditions were fixed for all the patients. However, in the CFD model, the boundary conditions varied from one patient to another. The comparison between CFD and experimental results was done by calculating the evolution of the rhodamine B concentration versus the inlet volume flow rate in the experimental study, and the evolution of temperature versus the inlet volume flow rate imposed for each patient in the numerical study.

Simulations ran for five cardiac cycles. The first two cycles were discarded as they are influenced by the transient effects on the simulation. The temperature was set to 400 K in the aneurysmal sac at the beginning of the third cycle and to 100 K in the parent vessel and the inlet. The washout was analyzed during the remaining three cardiac cycles. For some cases, due to the size of the aneurysm, the washout

wasn't complete at the end of the third cardiac cycles. However, due to the long computational time required to run the simulations, it was decided to only run three cardiac cycles for each patients, to have at least the trend of the evolution of the concentration of rhodamine.

### 3.3 Results

#### 3.3.1 PLIF results

The results of the PLIF study are presented in Figure 3.6. This figure shows the evolution of the rhodamine B concentration over time for each patient. Five runs were recorded for each patient and the three runs presenting the most consistent initial conditions for the concentration at the beginning of the experimental measurements were analyzed.

The quality of the data was impacted by the size and the location of the aneurysm and the laser plane chosen. The impact of the size can be easily identified when analyzing the data in Figure 3.6: Patients E and F present the clearest signal while being the smaller aneurysms. It is more difficult to visualize the dye fluorescence in larger aneurysms because it is harder for the laser plane to penetrate the larger coil mass and illuminate the complete aneurysm volume. This can be visualized in Figure 3.7. The green plane shows the area that was visualized in the camera and where the concentration was calculated. For small patients as E and F, the totality of the aneurysm was illuminated, whereas for bigger aneurysms only a part of the aneurysm filled with rhodamine was visualized.

The quality of the model (clarity of the silicone walls) also impacts the quality of the data but is minor when looking at the impact of the location of the aneurysm in the anatomy. Placing the model in the setup is highly difficult due to the limitations of the plane size and to the positioning of the needle used to inject the rhodamine. The model was set up to avoid that the parent vessel would intercept the laser plane, or in the camera view while avoiding visualizing the needle to avoid image artifacts due to the metallic composition of the needle. However, for some models as for Patient D, the laser light goes through the parent vessel resulting in poor image quality as it was impossible to place in a different position (see Figure 3.7D).

The laser plane is chosen to influence the analysis of the evolution of rhodamine B concentration in the aneurysm over time. For Patient G, the evolution of rhodamine concentration is studied in the area located on the opposite side of the neck (see Figure 3.7G). That region corresponds to the lower velocities in the aneurysm filled with coils, and the coils create artifacts due to the reflection. This will create a very noisy signal which explains Figure 3.6G. The laser plane is conditioned by the two previous factors: the size of the aneurysm and the anatomy of the parent vessel and

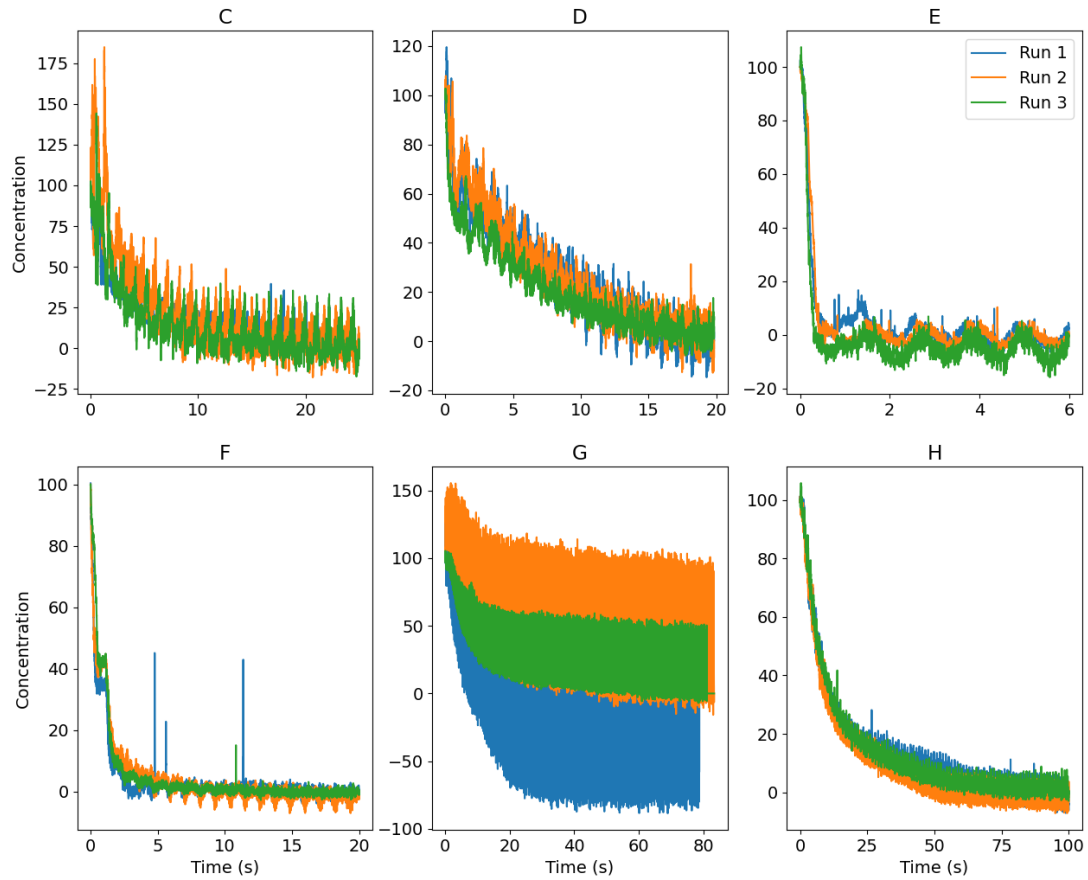


Figure 3.6: Evolution of the concentration during time for each patient over three runs for the PLIF analysis.

aneurysm.

The cardiac cycle (systole and diastole) also has an impact on the quality of the data. When analyzing Patient E (Figure 3.6E), even when the washout is complete there is still some variation in the concentration. Indeed, when the laser reaches the coils it created artifacts due to reflection. The coils move during the cardiac cycle which leads to a variation in the light intensity perceived with the camera during the cardiac cycle, creating this variation in the pixel values even when the washout is complete. Patients C and D present more variation in the results than patients E and F because they were recorded for a longer time as their aneurysm volume was larger. Nevertheless, those patients present a clear evolution of rhodamine concentration over time.

Figure 3.8 presents the evolution of the rhodamine concentration in the aneurysm over time normalized by the aneurysm volume for each patient. The concentration

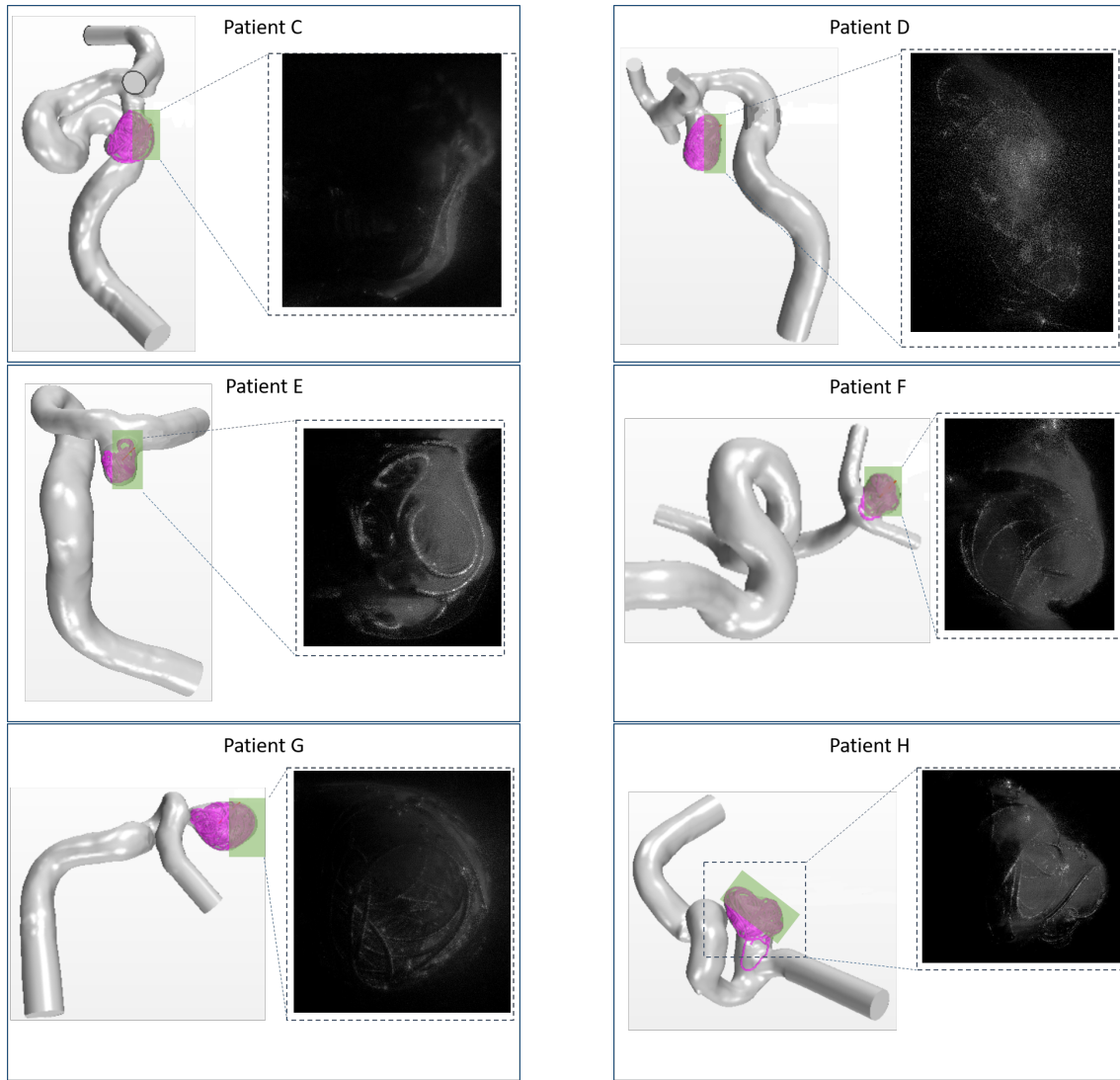


Figure 3.7: 3D numerical model vs image obtained through PLIF technique for each patient. In each numerical model, the green plane shows region observed in the images obtained through PLIF techniques, which correspond to the area illuminated with the laser. The PLIF image used is when the rhodamine concentration in the aneurysm is at 100%. The 3D models are positioned as they were in front of the camera.

is the mean of the concentration over the three runs for each patient. Patient G was excluded from this comparison due to the impact of the noise in the results visualization. The results show that all the patient present the same trend: the concentration of rhodamine decrease rapidly until at least 50% of the rhodamine is cleared away. Then the concentration decreases at a slower pace until complete washout. This phenomenon is amplified for the smaller aneurysms. Indeed Patient E presents a decrease of the rhodamine concentration very fast until its concentration is around 5% in the aneurysm, and then slowly decreases until full washout.

Table 3.2 presents the washout time for the six patients for three case scenarios:

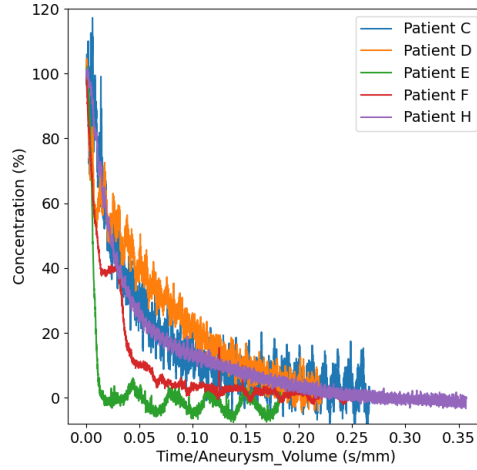


Figure 3.8: Evolution of the concentration over time normalized by the aneurysm volume for each patient. Patient G was excluded from this figure as the high variations of the concentration over time made it impossible to compare with the other patients (Figure 3.6G).

when the rhodamine concentration is 75%, 25%, and the residence time ( $c=0\%$ ). The results show that the residence time (RT) is lower for smaller volumes. However, the residence time is not only defined by the size of the aneurysm, indeed the anatomy of the aneurysm (shape and location) seems to have an impact in RT too. Patients D and H present smaller aneurysm volumes than patients C and G respectively, but, patients D and H present larger residence times than patients C and G respectively. This might be because when looking at the location of the aneurysm in Figure 3.2, both aneurysms (D and H) are located in bifurcation. Therefore the location and the anatomy of the aneurysm might also have an impact on the residence time.

Patient	$V_{aneurysm}$ (mm <sup>3</sup> )	$T_{c=0\%} = \text{RT}$ (s)	$T_{c=25\%}$ (s)	$T_{c=75\%}$ (s)
C	93.8	11.16	4.47	0.948
D	90.0	15.09	6.50	0.29
E	32.9	0.43	0.27	0.14
F	38.2	3.88	1.33	0.148
G	413.3	26.67	13.83	2.48
H	279.9	53.77	13.14	2.98

Table 3.2: Residence time where the washout is complete at  $c=75\%$ ,  $c=25\%$  and when the washout is finished ( $c=0\%$ ) for the six patients for the experimental values. The values presented are the mean values of the three runs. The residence time where the washout is complete at  $c=75\%$  for the coil-resolved simulations. The volume of each aneurysm for each patient.

### 3.3.2 Comparison with coil-resolved simulations results

To compare the CFD results with the PLIF results, the mean temperature in the aneurysm of the coil-resolved was converted into concentration (see equation (3.2)). At  $t = 0$  s (when  $T = 400$  K), the concentration was considered 100%, and when  $T=100$ K the concentration was 0 %, which is the temperature in the parent vessel and at the inlet. The evolution of concentration over time cannot be used to compare experimental and simulation results because the boundary conditions are not the same. Indeed, the flow rate is fixed for all the patients experimentally (see section 3.2.2.1) whereas the simulation uses patient-specific data (see section 3.2.3.2). Therefore, to compare numerical and experimental results, the concentration over a pushed volume at the inlet normalized by the pore volume was analyzed. The pore volume was defined as the volume of the empty spaces in the aneurysm: the volume of the aneurysm without the volume of the coils (see Table 3.1). Table 3.3 reproduces details the different flow rates in the experiment flow rate and the simulations, with the time of the simulations and time at the end of the recording, and the total volume pushed divided by the pore volume at the end of the experiment and the simulations.

Patient	Experimental			Simulation		
	Mean flow rate at the inlet (mL/s)	Record washout time (s)	$V_{pushed}/V_{pore}$ at the end of the experiment	Mean flow rate at the inlet (mL/s)	Time simulation (s)	$V_{pushed}/V_{pore}$ at the end of the simulation
C	3.83	24.99	1343	4.71	3.48	80
D	3.83	19.83	1199	4.27	3.03	100
E	3.83	5.99	1035	3.27	3.03	214
F	3.83	19.99	2816	4.81	3.03	264
G	3.83	78.80	920	2.17	2.68	17.8
H	3.83	99.99	1739	2.27	3.00	31.4

Table 3.3: Comparison between simulation and experimental results: mean flow rate, total simulation vs experimental time and volume pushed divided by the pore volume

The results of the CFD analysis compared with the PLIF results are shown in Figure 3.9. The results of the PLIF study are shown as the mean concentration for the three runs for each patient.

The evolution of concentration for the simulations results show the same pattern as it did for the experimental results: the concentration decrease in the first cardiac cycle very fast and then slowly decreases until full washout. The explanation is shown by the captions of the rhodamine distribution at different instants in the

simulations. Indeed, at the end of the first cycle, all the area near the neck is clear out of rhodamine, which corresponds to the areas where the velocities are higher. The caption at the end of the third cardiac cycle explains the impact of the size of the aneurysm in residence time: when the aneurysms are bigger, the aneurysm presents areas with lower velocities due to the coils and the size of the aneurysm, and those areas, which are located in the aneurysm in the opposite side of the neck need more time to washout.

For patients C, E, F, and G, the numerical models reproduce the experimental results. The small differences that exist between the experimental model and the coil-resolved model might essentially due to the hypothesis of the coils rigidity in the numerical model. In the experimental setup, the coils are affected by the flow rate and move during the cardiac cycle (little displacements). This allows to move the rhodamine in some areas in the aneurysm where the blood velocities are very small, which impacts residence time. This can be particularly perceived for patient E, where the evolution of the concentration vs the pushed volume is the same until  $c=20\%$ , and then the concentration decreases slower for the coil-resolved model than for the experimental setup. Since Patient G presents a very large aneurysm volume, therefore the residence time is very high (see Table 3.2), which makes difficult the comparison between the experimental and the numerical work. Indeed after only three cardiac cycles the rhodamine concentration has only decrease to 80%. However, when comparing the numerical and the experimental results, they both present the same trend, therefore we can expect that the numerical model would match the experimental.

Patients D and H present a larger deviation between the experimental and the numerical results (see Figure 3.9). For both patients the residence time is lower in the numerical than in the experimental model.

For Patient D, the origin of this deviation might be the quality of the image. As previously said, the data analysis and therefore the residence time is impacted by the quality of the data and Patient D presents a poor quality image due to the arguments previously developed (see Figure 3.7). The origin of this problem might also be linked with the laser plane chosen to analyze the concentration over time. Patients C and D have aneurysms presenting similar volumes (93.8 and 90.0 mm<sup>3</sup> respectively). When analyzing Figure 3.9, at the end of the third cardiac cycle, the concentration of rhodamine in the aneurysm is 60% and 25% for patients C and D respectively. These results are consistent with the captions in Figure 3.9. Indeed, Patient C, at the end of the third cardiac cycle is still filled with rhodamine (in red in the caption), due to its complex anatomy. However, the captions of Figure 3.9D show that at the end of the cardiac cycle the washout is almost complete for Patient D. This is coherent with the hemodynamic analysis: the mean velocities over one cardiac cycle in the aneurysm are 2.54 and 6.83 mm/s respectively for patients

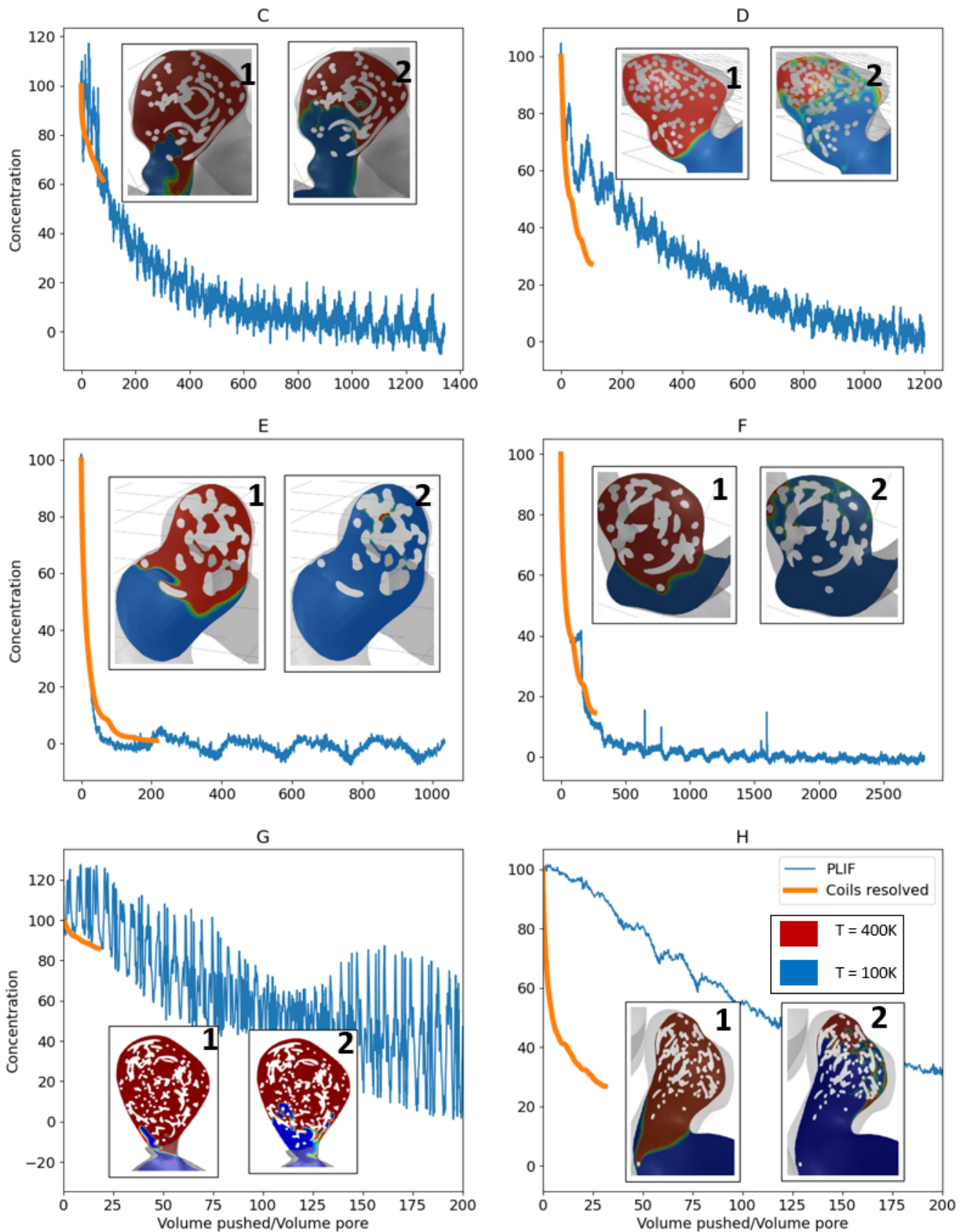


Figure 3.9: Comparison between the CFD and the PLIF study: evolution of the concentration of rhodamine B for the CFD model in orange and the experimental model in blue over pushed volume normalized by the pore volume. The results are shown for each patient. For each patients two captions of the evolution of concentration over time are shown: at the beginning of the washout (1), and at the end of the three cardiac cycles (2).

C and D. Therefore the coil-resolved model seems to be accurate. However, when analyzing Figure 3.8, the residence time is higher for patient D than for patient C, which is not coherent with the hemodynamic results. This difference can be due to the image quality and in particular the fact that the laser plane does not illuminate a representative part of the aneurysm. Indeed, the plane chosen for patient D does illuminate the neck area as much as it does for Patient C (see Figure 3.7), and the plane visualized is very different from the captions in Figure 3.9. This particular area, the neck, is where the washout starts (see captions in Figure 3.9), and this area is not visualized with the camera as it wasn't properly illuminated. Therefore the difference of the experimental and the numerical model might arise from the poor illumination of aneurysm D in the experimental model, and the coil-resolved model should be considered as the accurate result.

For Patient H, the origin of the deviation between the experimental and the numerical model comes from the definition of the aneurysm volume. Indeed, for this patients a part of the coils is in the parent vessel as we can see in Figure 3.2 and Figure 3.9. In the numerical model, the aneurysm is described as a envelop of the coils which includes the part of the coils in the parent vessel. This explains the quick decrease of rhodamine concentration in the numerical model, as the velocities in the parent vessel are larger than in the aneurysm and the washout is faster. In the experimental model, the aneurysm is described as the visible part in the laser plane (see Figure 3.7). Therefore, the only rhodamine concentration considered is visible in the aneurysm's dome. Therefore the experiment is not matching the numerical model due to the difference of the aneurysm definition. For this case, the plane wasn't lighting the neck therefore the rhodamine in the parent vessel was visible in the camera and couldn't be included in the calculation of rhodamine concentration in the aneurysm.

Overall the coil-resolved simulation seems to be reproducing the same evolution of concentration observed in the experimental study however to compare the experimental and the simulation results the laser plane needs to be adjusted so that all the regions of the aneurysm (near the neck and opposite to the neck) are used in the concentration analysis.

### 3.4 Discussion

This study presents an innovative experimental setup to measure residence time in cerebral aneurysms treated with endovascular coiling. Studying hemodynamics experimentally in treated aneurysms presents a challenge since the coils cannot be seen in a clinical exam. Most of the studies in the literature focus on measuring hemodynamics *in vivo* of the parent vessel for treated aneurysms [Levitt *et al.*, 2012]. Other studies have done PIV on idealized models treated with coils, however, the

hemodynamics were only measured in the parent vessel [*Nair et al.*, 2016]. This study presents a novel methodology for the analysis of hemodynamics in the coiled aneurysm. In particular, the residence time is an interesting parameter to be used to assess the success of the treatment. Indeed, blood coagulation is mainly related to the blood velocity in the aneurysm therefore residence time might be related to the coagulation and the success of the thrombus formation.

The experimental results have shown that residence time is related to the size of the aneurysm (lower for small aneurysms). Indeed most of the areas of the aneurysm near the neck, with the highest blood velocities, get washed out very fast in the first cardiac cycle, and then the rest of the aneurysm gets washout at a slower pace. The larger the aneurysm is, the longer the washout lasts. This has been also validated numerically with the coil-resolved simulations. Other factors might be related to residence time, as the location of the aneurysm and its anatomy, but needs further analysis to conclude on this.

The main advantage of the experimental setup method over the coil-resolved simulation is the time. Of course the experimentation needs time to be set up however each run only needs about 10 minutes per patient. The time needed to measure residence time in the aneurysm vary with the size of the aneurysm, however for big aneurysms, like patients G and H, the simulations could take up to several months.

The coil-resolved study results are consistent with the PLIF analysis: the rhodamine concentration decreases fast in the first cycle and then slowly decreases until full washout. The coil-resolved model allows to study at a high temporal resolution the evolution of concentration and to study the local areas where there might be stagnation and where thrombus would start creating. From the results (see Figure 3.9), the areas on the opposite side of the neck are the ones where the rhodamine stays longer, and therefore where the thrombus might start being formed. This results are coherent with previous numerical studies where the aneurysm with coils was modeled as a porous media [*Mitsos et al.*, 2008].

There are some differences between the experimental and the numerical methods linked with the boundary conditions of the model. For example, the coils are considered rigid in the numerical model whereas in the experimental setup there were small displacements. Also, the noise from the data collection of the PLIF analysis impacts this comparison.

Overall, the coil-resolved model has been validated with the experimental model and therefore can be used as a biofidelic model to study blood flow in cerebral aneurysms treated with coils.

There are some limitations related to this study. First, there is very little information that can be extracted from the PLIF analysis: only the concentration of rhodamine in the aneurysm. The analysis is done in a plane and therefore there

cannot be any local analysis of rhodamine distribution. The quality of the data is very sensitive to the size of the aneurysm and to the laser plane chosen. It doesn't seem to be necessary that to visualize in the camera the totality of the aneurysm volume. Indeed, Patient C's experimental results are coherent with the coil-resolved ones even if only a small section of the aneurysm was illuminated (see Figure 3.7). However, a representative part of the aneurysm needs to be illuminated, in particular, a plane illuminating from the top of the aneurysm to the neck seems is important to study residence time in a coiled aneurysm. However, this limitations could be improved by complexifying the optical setup: adding another laser to illuminate another part of the aneurysm or using mirrors to redirect the light of the laser.

The concentration being analyzed in the plane is also an issue for the comparison with the CFD results. Indeed we compared the mean concentration over the aneurysm volume in the coil-resolved model and the mean concentration of rhodamine in a plane. This difference might also explain the difference in some patients between the PLIF and the CFD results (example for patient D and H). Another aspect that might impact the difference between the CFD and the PLIF results is that the aneurysm volume was defined manually for the PLIF analysis. Indeed, for the CFD study, the neck was defined as the convex hull envelope of the coils numerically (see section 3.2.1). In the PLIF analysis, the neck was defined as the coils envelop manually. The two aneurysms compared might not be exactly the same and that might be impacting the results of the comparison between coil-resolved and PLIF analysis.

The CFD simulations only ran for three cardiac cycles due to simulation resources. Three cardiac cycles are enough for the smaller patients, and for the larger aneurysms, it can give the trend of the evolution of concentration over time. Having more computational improvement would improve the analysis.

Overall, this is an innovative study that includes an experimental and CFD comparison of residence time in intracranial aneurysms treated with coils. The coil-resolved model used in previous studies [*Levitt et al.*, 2016; *Barbour*, 2018] was validated experimentally and can be used as a realistic model of the cerebral aneurysm treated with coils to study hemodynamics in the treated aneurysm. This analysis was done for a small sample of patients (six) and we cannot deduce from the results obtained a relation between residence time and treatment success. However, this work presents a methodology to analyze, either numerically or experimentally, residence time in a larger cohort of patients, and to establish, in the future, hemodynamic parameters related to treatment success.

### 3.5 Conclusion

In this work, residence time was determined experimentally and numerically in six cerebral aneurysms treated with endovascular coiling. Planar laser-induced

fluorescence technique was used to measure residence time in phantom artery models where the aneurysms were treated with coils. The results showed that residence time in the treated aneurysm is influenced by the size of the aneurysm and its anatomy. Passive scalar simulations were done in the coil-resolved model developed in previous studies to compute residence time in the CFD numerical model. When comparing CFD and experimental studies, the results of the numerical simulations are coherent with the experimental results. Therefore the coil-resolved model seems to be an accurate model to measure resident time. In the future, this biofidelic numerical model can be used in a larger cohort of patients to investigate the hemodynamic parameters related to treatment success.



---

## Modeling flow in cerebral aneurysm after coils embolization treatment: A realistic patient-specific porous model approach

### Contents

---

4.1	Introduction . . . . .	65
4.2	Method . . . . .	67
4.2.1	Image acquisition . . . . .	67
4.2.2	Porosity distribution . . . . .	69
4.2.3	Flow through the porous medium . . . . .	71
4.2.4	CFD validation . . . . .	72
4.3	Results . . . . .	76
4.3.1	Porosity distribution . . . . .	76
4.3.2	Permeability and inertial factor . . . . .	77
4.3.3	CFD simulations . . . . .	80
4.4	Discussion . . . . .	83
4.5	Conclusion . . . . .	85

---

### Abstract

Computational fluid dynamics (CFD) has been used to evaluate the efficiency of endovascular treatment in coiled cerebral aneurysms. The explicit geometry of the coil mass cannot typically be incorporated into CFD simulations since the coil mass cannot be reconstructed from clinical images due to beam hardening artifacts caused by the coils' small diameter, high packing density, material X-ray scattering. Existing methods use imprecise porous medium representations. We propose a new porous model taking into account the porosity heterogeneity of the coils deployed in the aneurysm. The porosity

heterogeneity of the coil mass deployed inside two patients' cerebral aneurysm phantoms is first quantified based on 3D x-ray synchrotron images. These images are also used to compute the permeability and the inertial factor arising in porous models. A new homogeneous porous model (porous crown model), considering the coils' heterogeneity, is proposed to recreate the flow within the coiled aneurysm. Finally, the validity of the model is assessed through comparisons with coil-resolved simulations. The strong porosity gradient of the coil mass, measured close to the aneurysmal wall is well captured by the porous crown model. The permeability and the inertial factor values involved in this model are closed to the optimal homogeneous porous model leading to a mean velocity in the aneurysmal sac similar to the value in the coil-resolved model. The porous crown model allows for an accurate description of the mean flow within the coiled cerebral aneurysm.

## 4.1 Introduction

Endovascular coiling is a common technique to treat cerebral aneurysms before rupture to slow down blood flow in the aneurysm and to promote thrombus formation inside the aneurysmal sac. Subsequently, this relieves the hemodynamics stimuli on the vascular wall and leads to aneurysmal stability or healing [Guglielmi *et al.*, 1991]. There is, however, a risk of recurrence [Crobeddu *et al.*, 2013], and being able to evaluate the efficiency of coil embolization treatment would help in the prediction of outcomes. Hemodynamics in the aneurysm can provide information on the growth and rupture of the aneurysm [Meng *et al.*, 2007], in particular when employing patient-specific data [McGah *et al.*, 2014; Venugopal *et al.*, 2007; Karmonik *et al.*, 2009]. The study of the hemodynamics of flow in the aneurysmal sac through CFD, and computing metrics linked to thrombus formation have shown the impact of hemodynamics on aneurysm recurrence after treatment [Damiano *et al.*, 2015].

Computational modeling of the blood flow inside an aneurysm treated with coils presents several challenges. First, the geometry of the coil mass cannot be reconstructed from clinical images, due to scatter artifacts of computed tomography (CT) or insufficient spatial resolution to capture the coils on magnetic resonance imaging (MRI). To approach coil modeling in CFD, we used a high-energy scan of 3D-printed aneurysmal silicone phantoms treated with real coils. This high-energy narrow-bandwidth scan, available in a Synchrotron, is necessary to reconstruct the coil configuration as deployed inside the aneurysmal sac [Levitt *et al.*, 2016]. These studies that reproduce the exact configuration of the coils can serve as a reference to understand the hemodynamics features in coil-treated aneurysms, but cannot be used *in vivo*, and therefore are not translational to patient-care in a clinical setting. Additionally, these coil-resolved basic fluid mechanics studies carry a very high computational cost, an obstacle that also needs to be overcome to translate

CFD to clinically relevant time frames for treatment planning or outcome assessment [Augsburger *et al.*, 2011]. Modeling the coil configuration in the aneurysmal sac *in vivo*, rather than obtaining the coil-resolved geometry, can reduce the computational cost and, if it captures the hemodynamics in sufficient level of detail to produce accurate metrics for treatment prediction, bridge the gap between basic and translational studies.

Modeling coils as porous medium has shown promise [Levitt *et al.*, 2016], even if the homogeneous isotropic porous medium assumptions are well-known to oversimplify the coil configuration. Early porous models in the literature considered the coil mass as a homogeneous and isotropic medium [Kakalis *et al.*, 2008; Mitsos *et al.*, 2008; Levitt *et al.*, 2016]. The material parameters involved in describing the coil mass, such as the permeability and the inertial factor, were estimated using the mean porosity of the aneurysm after coiling. The geometry of the coils, however, is well-known to be heterogeneous and have preferential directionality due to the deployment method and the memory-shape alloys used in the coils. The need for these more complex models, and higher accuracy in simulating the hemodynamics in coil-treated cerebral aneurysms was demonstrated by comparing predictions from homogeneous isotropic porous medium computations, where the permeability is calculated from the mean porosity in the aneurysm, and those from synchrotron coil-resolved simulations [Levitt *et al.*, 2016]. The results of this study showed that the mean velocities and wall shear stresses in the aneurysm are overestimated and not fully representative of blood flow in the aneurysm with coils.

Experimental work has been done to determine the equivalent permeability of the coil mass [C.Sadasivan *et al.*, 2018; Chueh *et al.*, 2015]. These have provided evidence of how, at the same packing density, the permeability varies significantly. Therefore, there is a need to consider the heterogeneity of coil distribution to determine the permeability. As the previous study do not consider the complexity of the geometry, the models are not sufficiently accurate for clinical predictions. Yadollahi-Farsani *et al.* [2019] studied a porous model that considered the heterogeneous distribution of the porosity and permeability. The method consisted of creating a heterogeneous porous medium model within a grid and defining for each element the porosity and permeability in that space, and varying the discretizing grid elements. The prediction of hemodynamics metrics improves with a more complex porous model, as it provides a more accurate reconstruction of the blood flow in the aneurysmal sac after being treated with coils. However, the heterogeneous models proposed to date need the actual configuration of the coils to compute the heterogeneous porosity and permeability and, therefore, cannot be used for prediction of treatment outcomes in patient-specific cases [Yadollahi-Farsani *et al.*, 2019].

There is a well-established need to define the porous parameters (porosity, permeability, and inertial factor) by considering the heterogeneity of the media, but also

creating a model that can be used for prediction, therefore not reliant on detailed knowledge of the coil configuration inside the aneurysmal sac. The purpose of this study is to present an accurate porous medium model after coil deployment and to validate this model against coil-resolved hemodynamics in two *in vitro* reproductions of treated aneurysm patients, using patient-specific boundary conditions in the CFD model. This is done in three steps: (i) characterizing the heterogeneity of the porous medium (coils in the cerebral aneurysm) through image analysis of the *in vitro* aneurysmal vasculature models; (ii) formulating a porous model that allows for the description of the flow inside the aneurysm; and (iii) validating this model against the gold standard coil-resolved geometry obtained through synchrotron microtomography.

## 4.2 Method

### 4.2.1 Image acquisition

Two patients (A and B) with a cerebral aneurysms treated with endovascular coils (Stryker Endovascular, Kalamazoo, Michigan, USA), with diameters 240 – 250  $\mu\text{m}$  and lengths 2 – 30 cm, were enrolled at the University of Washington’s Harborview Medical Center in Seattle, WA, USA. Figure 4.1 shows the anatomy of both patients and Table 4.1 presents the volume of the aneurysm and the characteristic length  $L$ , with  $L$  being the longest inertial axis. Three-dimensional rotational angiography of the carotid artery and aneurysm were obtained before each patient’s aneurysm treatment. After image segmentation of those scans, a 3D model of the aneurysm and parent vessel was created. Briefly, a 1:1 scale positive mold was 3D printed in acrylonitrile butadiene styrene, then, casted in a clear polyester resin (PDMA, Clear-Lite; TAP plastics, San Leandro, California, USA) [Venkat *et al.*, 2019]. The same neurosurgeon who performed the endovascular surgery in the patient, treated the *in vitro* model with the same procedure: the same commercially-available coils were inserted and in the same order. This ensures consistency between the *in vivo* and *in vitro* techniques.

Coils cannot be reconstructed from the clinical CT scans, but can be imaged *in vitro* with synchrotron tomography, with high resolution and without beam hardening artifacts. To create the coil geometry reconstructions, the *in vitro* aneurysmal models were imaged at beamline ID19 of the European Synchrotron Radiation Facility (<http://www.esrf.eu>) in Grenoble (France), before and after coil placement. The company Novitom in Grenoble (France) performed the tomography on the two models and provided the images segmented. The image resolution was 12.92  $\mu\text{m}$  and 15.58  $\mu\text{m}$  for patient A and B respectively. The use of monochromatic radiation avoids artifacts, and beam hardening effects. The scans of the coils were segmented and, to

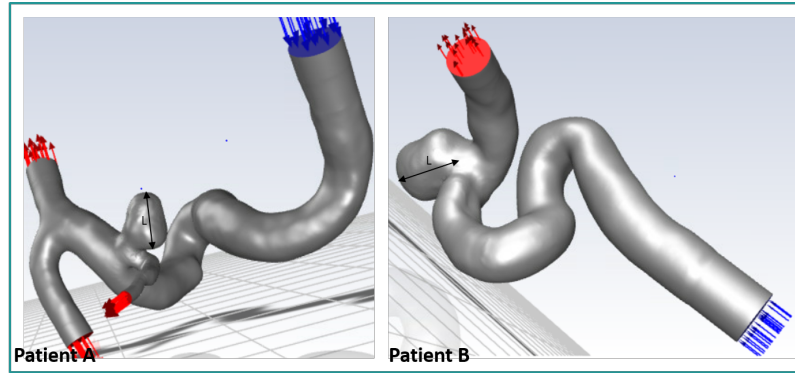


Figure 4.1: Aneurysmal anatomy: Patient A (left) and B (right). The arrows present the direction of flow: blue is the inlet and red the outlet.  $L$  is a characteristic length, defined as the length of the longest inertial axis (Table 4.1).

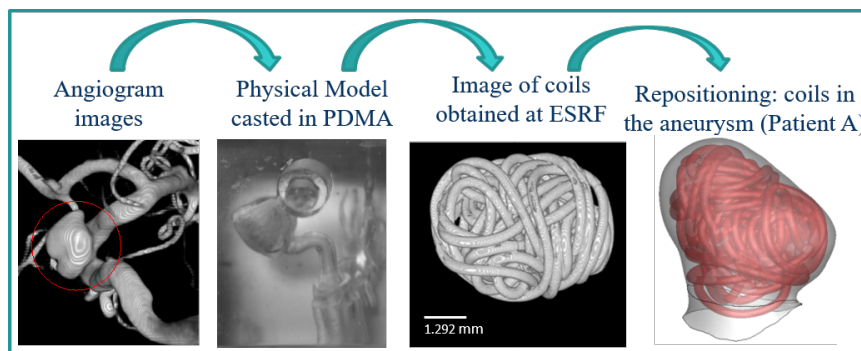


Figure 4.2: Main steps of the image acquisition: from the angiographic image on the left, to the positioning of the coils in the aneurysm. The results of this process is shown for Patient A.

validate the segmentation, the volume of the coils based on the image reconstruction was compared to the volume calculated from the characteristics of the real coils provided by the manufacturer.

The geometry of the coils was positioned in the 3D model of the aneurysm reconstructed from the patient CT scans. The centerlines from the patient’s parent vessel (from the clinical scan) and from the model (synchrotron microtomography) were extracted using Vascular Modeling Toolkit software (<http://www.vmtk.org>) and matched by an iterative closest point method [Wilm, 2020]. This provided the transformation matrices (rotation and translation matrix) that were then applied to the geometry of the coils, using MATLAB (MathWorks, Inc., Natick, Massachusetts, USA), to reposition the coils onto the patient vasculature. This entire process is summarized in Figure 4.2.

Patient	Aneurysm volume (mm <sup>3</sup> )	$L$ (mm)
A	45.7	5.2
B	107.1	6.6

Table 4.1: Volume of the aneurysm and characteristic length  $L$  for patient A and B.

## 4.2.2 Porosity distribution

### 4.2.2.1 Definition of the porous medium

The neck surface was defined as the intersection between the coil mass envelope and the aneurysm's parent vessel geometry. The envelope was created using MATLAB and the geometry adjustments to create the neck interface were done using StarCCM+ (CD-adapco, Melville, New-York, USA). The volume of the aneurysm with coils was transformed into image format using ImageJ [Schindelin *et al.*, 2012] and the porosity was calculated by voxel counting (white for coils and grey for blood filling the aneurysmal sac, see Figure 4.3). The mean porosity  $\phi_m$  of the coil is 0.697 and 0.825 for patients A and B, respectively. Two methods were then developed to analyze the porosity distribution of the coils within the aneurysmal sac: the cube porosity map and crown porosity map.

#### 4.2.2.2 Cube porosity map

The first method to analyze the porosity distribution consisted of creating a porosity map of the aneurysm using a cube discretization. The volume of the coil and aneurysm was divided into cubes and the porosity of each cube was calculated counting the white and grey voxels inside each cube, as explained above. Only the cubes fully enclosed inside the aneurysmal sac were analyzed, to avoid edge effects (Figure 4.3). Two cube sizes were defined: small cube with a size of  $2d$  (where  $d$  is the diameter of the coil, 250  $\mu\text{m}$ ), and large cubes with size equal to  $4d$ . In both cases,  $4d$  and  $2d$  were very small compared to  $L$ , and having two different sizes allows for evaluation of the impact of the element size. Figure 4.3 shows, for example, the cube porosity map of the patient A. All the image analysis was performed using MATLAB.

#### 4.2.2.3 Crowns porosity map

The objective of the second method is to determine a porosity profile, that is, the porosity gradient along the radius of the aneurysm, induced by the presence of the aneurysm wall. Through image treatment, the crowns were defined by eroding consecutively the cerebral aneurysm with coils defined using MATLAB, where the erode region is a crown. The porosity was calculated for each crown. This method

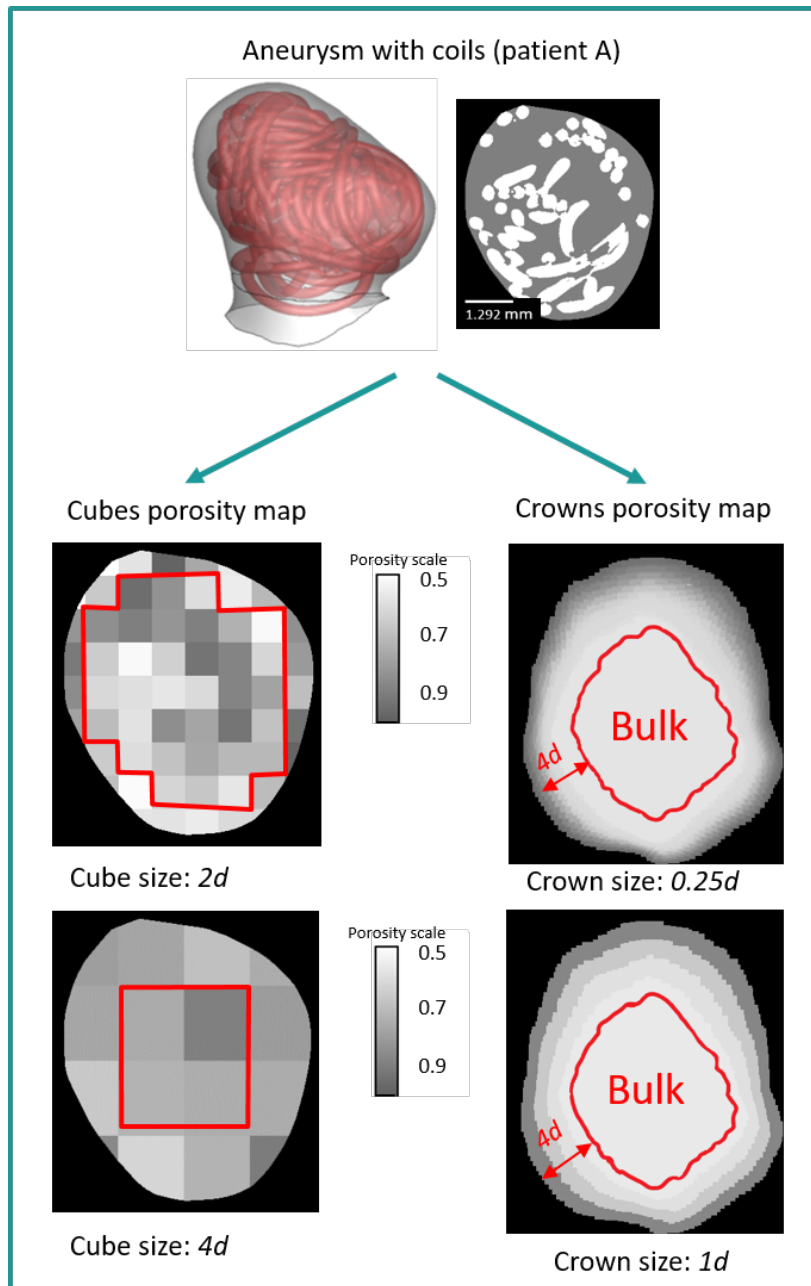


Figure 4.3: Definition of the porous medium for patient A: The aneurysm containing the exact coil geometry as obtained from synchrotron microtomography (top left). Cross-section of the aneurysm with coils (top right). Cube porosity map with the 2 cube sizes:  $2d$  (middle left) and  $4d$  (bottom left), and in red the centered cubes. The crown porosity model, with two different crown sizes  $0.25d$  (middle right) and  $1d$  (bottom right). The colors vary with the porosity, as seen in the color bar.

allows us to characterize the porosity gradient near the walls and at the neck, represented in the external crowns. This is the key to define the flow in the rest of the aneurysm treated with coils, as will be shown in the Results section. Four sizes of crowns were used:  $0.25d$ ,  $0.5d$ ,  $1d$ , and  $2d$  and a total radial thickness to fill (spherical shells) within the aneurysmal sac of  $4d$ , for all crown sizes. As in the cube porosity map, these four crown sizes allow us to evaluate the discretization impact on the results. For example, Figure 4.3 shows a section of the crown porosity map, sharing the same representation as the cube map, for two different crown sizes.

### 4.2.3 Flow through the porous medium

Flow in the coil-filled aneurysm is modeled as in a homogeneous and isotropic porous medium by the Darcy-Forchheimer equation (4.1), as it has been done extensively for cerebral aneurysms in the literature [*Levitt et al.*, 2016; *Kakalis et al.*, 2008; *Mitsos et al.*, 2008]:

$$\nabla p = -\frac{\mu}{K}\mathbf{u} - \frac{1}{2}\rho C_2|\mathbf{u}|\mathbf{u} \quad (4.1)$$

where  $\rho$  is the fluid density ( $\text{kg/m}^3$ ),  $\nabla p$  is the pressure gradient ( $\text{Pa/m}$ ),  $\mu$  the fluid viscosity ( $\text{Pa}\cdot\text{s}$ ),  $\mathbf{u}$  is Darcy's velocity ( $\text{m/s}$ ) and  $K$  ( $\text{m}^2$ ) and  $C_2$  ( $1/\text{m}$ ) are the permeability and inertial factor coefficient, respectively. These two parameters mainly depend on the porosity at the first order.

#### 4.2.3.1 Permeability of the coil

In order to determine the evolution of the permeability of the coil mass as a function of its porosity, the permeability tensor  $\mathbf{K}$  of the  $4d$  centered cubes used in Section 4.2.2.2 was computed using Geodict2019 (Math2Market) by solving a specific boundary-value problem arising from homogenization [*Auriault et al.*, 2009]. In the following, the non-diagonal terms of the tensor  $\mathbf{K}$ , about 50 times lower than the diagonal terms ( $K_x$ ,  $K_y$  and  $K_z$ ), are not presented. These non-zero permeability components were then compared with the self-consistent estimates (SCE) established by Boutin [*Boutin*, 2000], for parallel ( $K_L$ ) and perpendicular ( $K_T$ ) flow through cylindrical bundles, given by the equations (4.2) and (4.3) respectively, with  $a = d/2$ .

$$K_L = \frac{a^2}{4(1-\phi)} \left( -\ln(1-\phi) - \frac{(1-(1-\phi))(3-(1-\phi))}{2} \right) \quad (4.2)$$

$$K_T = \frac{a^2}{8(1-\phi)} \left( -\ln(1-\phi) - \frac{(1-(1-\phi)^2)}{(1+(1-\phi)^2)} \right) \quad (4.3)$$

#### 4.2.3.2 Inertial factor

The inertial factor of the  $4d$  centered cubes was calculated using Geodict2019 (Math2Market) by solving a specific boundary-value problem arising from the homog-

enization [Auriault *et al.*, 2009]. More precisely, Navier-Stokes equations were solved in the  $x$ ,  $y$ , and  $z$  direction with periodic boundary conditions, the flow was induced by an imposed pressure drop (Pa) which varies to have pore Reynolds numbers (using  $d$  the characteristic length) between 0.001 and 100. It is important to note that, according to Barbour [Barbour, 2018], the pore Reynolds number of the flow in the coil-treated aneurysm is approximately 10 at peak systole. The inertial factor was calculated based on equation (4.1) for the highest pressure drop imposed, with the permeability value calculated with the previous study. The calculations were done using water as the working fluid (density=1000 kg/m<sup>3</sup>, viscosity=0.001 Pa.s) but the value of the form factor is not affected by whether the working fluid is water or blood. The inertial factor results were then fitted by the following equation,

$$C_2(\phi) = \frac{2}{\sqrt{K_T(\phi)}} 3(1 - \phi)^2 \quad (4.4)$$

where  $K_T$  is the permeability given by equation (4.3).

#### 4.2.4 CFD validation

##### 4.2.4.1 Reference model (coil-resolved)

To be able to determine through CFD the success or failure of treatment, it is necessary to have patient-specific models with realistic boundary conditions as the gold standard. This reference model uses the 3D model of coiled aneurysm described in section 2.1 [Levitt *et al.*, 2016]. The meshing of the aneurysmal domain was done using StarCCM+, using tetrahedral elements. The size of the mesh was 200  $\mu\text{m}$  for the parent vessel and 20 – 40  $\mu\text{m}$  at the surface of the coils [Levitt *et al.*, 2016]. Finite volume fluid simulations were performed using Fluent (ANSYS, Release 17.1; ANSYS, Canonsburg, Pennsylvania, USA). Blood flow was modeled as a Newtonian and incompressible fluid, with a viscosity of 0.0035 Pa.s and a density of 1050 kg/m<sup>3</sup>, consistent with previous studies in the literature [McGah *et al.*, 2011]. The Navier-Stokes equations were solved:

$$\rho \left( \frac{\partial \mathbf{u}}{\partial t} + \mathbf{u} \nabla \mathbf{u} \right) = -\nabla p + \mu \nabla^2 \mathbf{u} \quad \text{and} \quad \nabla \cdot \mathbf{u} = 0 \quad (4.5)$$

Patient-specific boundary conditions were obtained by using a dual-sensor Doppler guidewire (ComboWire and ComboMap; Volcano Corp, San Diego, California, USA), with the measurements obtained during the surgical procedure [Levitt *et al.*, 2014]. These measurements were converted into a pulsatile Womersley velocity profile at the inlet, and a Resistance Capacitance (RC) condition was used at the outlets for Patient A to match mean and peak flow rate splits (see Figure 4.1). Since Patient B only has one outlet (see Figure 4.1), the boundary condition at the outlet was set to constant pressure. The artery wall was considered rigid, with a non-slip

boundary condition. The simulations ran for three cardiac cycles and the values of the hemodynamics parameters were taken from the last cycle, discarding the first two as influenced by transient effects from the simulation initialization. Multiple parameters such as mean velocity in the aneurysmal sac and at the neck, wall shear stress along the aneurysmal wall (WSS), oscillatory shear index (OSI), etc. can be used to describe blood flow in the aneurysm.

This coil-resolved model provides data that could be used to understand the hemodynamics factors that play a role in the efficacy of the endovascular treatment. However, it cannot be used for prediction in the clinical setting. A porous model that reproduces the flow in the coil-resolved simulation but without requiring the exact coil configuration after deployment is sought. This technique would allow the prediction of the treatment outcome in a patient-specific manner, just based on the clinical imaging (rather than the creation of 3D printed models and subsequent treatment and synchrotron scanning), with low computational and time to solution requirements.

#### 4.2.4.2 Porous models

This paper shows the methodology to create patient-specific CFD simulations where a porous medium replaces the exact coil mass geometry, and the flow can be described by Darcy-Forchheimer's equation (4.1). Modeling coils as a homogeneous and isotropic porous medium (see equation 4.1) can potentially take into account the heterogeneity of the coil mass, without adding the complexity of the fully homogenized anisotropic and inhomogeneous volumes filling the aneurysmal sac. In order to evaluate the improvement of the proposed modelling, three different cases have been considered:

- Case 1 - Porous model based on the mean porosity -  $K_m$  and  $C_{2m}$ : As the first porous model analyzed in the literature [Levitt *et al.*, 2016], a homogeneous isotropic porous medium based on the mean porosity  $\phi_m$  of the aneurysm with coils, is studied for reference. The variables defining the porous medium,  $K_m$  and  $C_{2m}$ , were calculated with equation (4.3) for the permeability and (4.4) for the inertial factor, where  $\phi = \phi_m$  as the mean porosity in the aneurysm with coils for each patient.
- Case 2 - Optimal porous model -  $K_{op}$  and  $C_{2op}$ : The second model is created with the purpose of defining the optimal permeability and inertial factor ( $K_{op}$  and  $C_{2op}$ ), to obtain the same mean velocities in the aneurysm as for the coil-resolved model (where the percentage of error was below 1%, see Table 4.5). The optimal parameters have been determined by first running Stokes flow simulations varying the permeability value to determine  $K_{op}$ , and then complete model simulations varying the inertial term only, to determine  $C_{2op}$ .

- Case 3 - Porous crown model -  $K_p$  and  $C_{2p}$ : The porous crown model developed in section 4.2.2.3 is used at this stage to define a homogeneous isotropic porous model that would match the optimal porous model (case 2). Modeling the flow using the crown model, there are two main possible directions in which the flow propagates in the aneurysm: predominantly tangential to the crowns as shown by the red arrow on Figure 4.4, or perpendicular to the crowns as shown by the blue arrow. The model for permeability and inertial factor in the crown model is defined in equations (4.6) and (4.7), based on published data from a model arising from homogenization [Auriault *et al.*, 2007]. The permeability and inertial factor for the parallel model (the flow along the crowns) are expressed in equation (4.6) and in equation (4.7) for the serial model (flow perpendicular to the crowns):

$$K_p = \sum_1^N f_i K_i + f_b K_b \quad C_{2p} = \left( \sum_1^N \frac{f_i}{\sqrt{C_{2i}}} + \frac{f_b}{\sqrt{C_{2b}}} \right)^{-2} \quad (4.6)$$

$$K_s = \left( \sum_1^N \frac{f_i}{K_i} + \frac{f_b}{K_b} \right)^{-1} \quad C_{2s} = \sum_1^N f_i C_{2i} + f_b C_{2b} \quad (4.7)$$

where  $K_i$ ,  $C_{2i}$  and  $f_i$  are the permeability, the inertial factor and the volume fraction for the  $i$ th crown and  $N$  is the number of crowns.  $K_b$ ,  $C_{2b}$  and  $f_b$  are the permeability, the inertial factor and the volume fraction for the homogeneous center (bulk). Permeabilities  $K_i$  and  $K_b$  are calculated based on the self-consistent estimate concerning the transversal flow (4.3), inertial factors  $C_{2i}$  and  $C_{2b}$  are computed from the equation (4.4). The values of  $K_p$ ,  $K_s$ ,  $C_{2p}$  and  $C_{2s}$  for patients A and B for a crown size of  $0.25d$  are in Tables 4.3 and 4.4. This crown size was chosen because the smallest crown better reflects the heterogeneity of the porosity distribution close to the aneurysm's wall, i.e. where the porosity and consequently the permeability are very large. The number of layers  $N$  was defined as 16 crowns (Figure 4.4). The parallel model seems to represent better the flow model propagation since the values of  $K_p$  and  $C_{2p}$  are very close to  $K_{op}$  and  $C_{op}$ . This hypothesis was also validated numerically.

To analyze the accuracy of each porous model, we compared it with the coil-resolved CFD simulations, which used the synchrotron microtomographic scans of the coil mass as the ground truth. The fluid properties and the meshing were defined above (section 4.2.4.1). Fluid flow in the porous medium was described by Navier Stokes-Brinkman equations:

$$-\rho \left( \frac{\partial \mathbf{u}}{\partial t} + \mathbf{u} \nabla \mathbf{u} \right) - \nabla p + \mu_e \nabla^2 \mathbf{u} = \frac{\mu}{K} \mathbf{u} + C_2 \frac{1}{2} \rho |\mathbf{u}| \mathbf{u} \quad \text{and} \quad \nabla \cdot \mathbf{u} = 0 \quad (4.8)$$

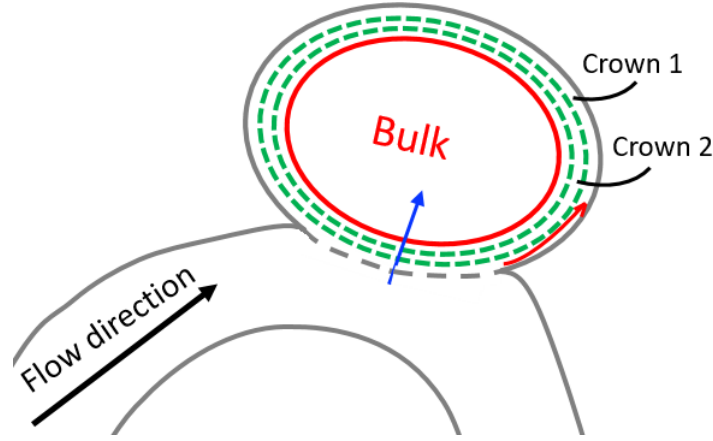


Figure 4.4: Modeling aneurysms with coils as a homogeneous porous media, demonstrating blood flow through the crown model: red arrow shows flow moving along the crowns and the blue arrow shows the blood flow perpendicular to the crowns.

where  $\nabla p$  is the pressure gradient (Pa/m),  $\mathbf{u}$  is the fluid velocity,  $K$  ( $\text{m}^2$ ) the permeability,  $C_2$  (1/m) is the inertial factor and  $\mu_e$  is an effective viscosity given by  $\mu_e = \mu_r \mu$ , where  $\mu_r$  is the relative viscosity and  $\mu$  is the blood's viscosity. Equation (4.8) can be simply viewed as a superposition of Navier-Stokes (4.5) and Darcy-Forchheimer (4.1) equations. The term  $\mu_e \nabla^2 \mathbf{u}$  is often referred as the Brinkman term. If we neglect inertial effects ( $C_2 = 0$ ), equation (4.8) reduces to Darcy's law for low values of the permeability  $K$  and to the Navier-Stokes equation for high values of  $K$ . The transition between these two regimes occurs when the Brinkman's term  $\mu_e \nabla^2 \mathbf{u}$  is of the same order of magnitude as  $\mu \mathbf{u}/K$  [Brinkman, 1947]. The value of the relative viscosity is not well known and several values can be found in the literature. In our case, the relative viscosity was taken as 1, as has been determined by comparing 2D numerical simulations and analytical solutions recently proposed for simple configurations Zaripov et al. [2019].

The values of the permeability and the inertial coefficient used in the three porous models are summarized in Tables 4.3 and 4.4. The accuracy of each porous model has been evaluated in two steps. First, a Stokes flow simulation was performed to assess the accuracy of the linear part of the equation (4.8), i.e. assuming that  $C_2 = 0$ . In that case, the flow was steady with an inlet velocity equal to 0.001 m/s ( $Re \ll 1$ , Stokes flow) and the pressure outlets equal to 0 Pa. Second, to validate the non-linear part of the Darcy-Forchheimer equation, the Navier-Stokes-Brinkman equations were solved. The boundary conditions were the same as described in section 4.2.4.1. The summary of these two sets of simulations is given in Table 4.2 and are noted  $S0_\alpha$ , and  $S1_{\alpha\beta}$  respectively, where  $\alpha$  or  $\beta = m$  (case 1),  $op$  (case 2),  $p$  (case 3). For both patients A and B, the accuracy of each porous model has been evaluated by comparing the mean velocity values in the aneurysm with the corresponding coil-resolved model.

Model	Simulation name	Boundary conditions	Porous model definition
Coil-resolved	S0 S1	Stokes Pulsatile	
Homogeneous isotropic porous media based on $\phi_m$	S0 <sub>m</sub> S1 <sub>mm</sub>	Stokes Pulsatile	$\phi_m$ , $K_m$ $\phi_m$ , $K_m$ , $C_{2m}$
Homogeneous isotropic porous media optimal values	S0 <sub>op</sub> S1 <sub>opop</sub>	Stokes Pulsatile	$\phi_m$ , $K_{op}$ $\phi_m$ , $K_{op}$ , $C_{2op}$
Homogeneous isotropic porous media taking into account the heterogeneity	S0 <sub>p</sub> S1 <sub>pm</sub> S1 <sub>pp</sub>	Stokes Pulsatile Pulsatile	$\phi_m$ , $K_p$ $\phi_m$ , $K_p$ , $C_{2m}$ $\phi_m$ , $K_p$ , $C_{2p}$

Table 4.2: Summary of the simulations for patients A and B

Pt	$\phi_m$	$K_m$ (m <sup>2</sup> )	$K_p$ (m <sup>2</sup> )	$K_s$ (m <sup>2</sup> )	$K_{op}$ (m <sup>2</sup> )
A	0.697	2.81.10 <sup>-9</sup>	1.42.10 <sup>-8</sup>	8.66.10 <sup>-9</sup>	1.30.10 <sup>-8</sup>
B	0.825	1.09.10 <sup>-8</sup>	5.28.10 <sup>-8</sup>	6.72.10 <sup>-9</sup>	5.00.10 <sup>-8</sup>

Table 4.3: Summary of the permeability values for patients A and B for the porous media models, used in Stokes (and pulsatile) flow simulations.

Pt	$\phi_m$	$C_{2m}$ (1/m)	$C_{2p}$ (1/m)	$C_{op}$ (1/m)
A	0.697	1.23.10 <sup>4</sup>	1.23.10 <sup>3</sup>	2.10 <sup>3</sup>
B	0.825	3.34.10 <sup>3</sup>	1.11.10 <sup>2</sup>	4.10 <sup>2</sup>

Table 4.4: Summary of the inertial factor values for patients A and B for the porous media models, used in pulsatile flow simulations.

## 4.3 Results

### 4.3.1 Porosity distribution

#### 4.3.1.1 Cube porosity map

The results for the analysis of the porosity distribution with the cube method are presented in Figure 4.5 for Patient A. The bar size represents the number of cubes with the same porosity for the two cube sizes:  $2d$  (a) and  $4d$  (b). Patient A and B show similar results: for a cube size equal to  $2d$  the porosity varies between 0.52 and 1. This latter value suggests that the size of some pores are larger than  $2d$ , and this cube size is too small to be representative of this as a porous medium. For a cube size equal to  $4d$ , the porosity varies between 0.72 and 0.9. This cube size seems more appropriate to capture the heterogeneity of the porous medium and has been then used to compute the permeability and the inertial factor.

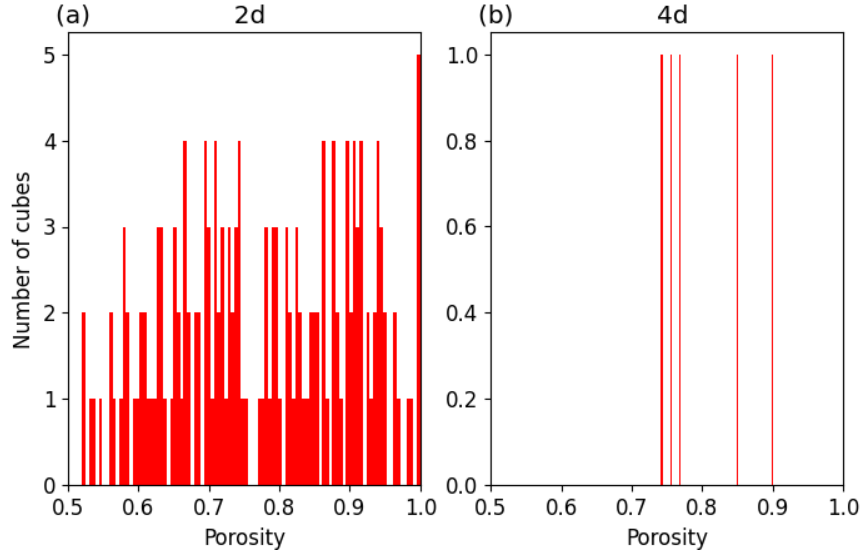


Figure 4.5: Histogram of the porosity of the cubes for two sizes of cube's side:  $2d$  (left) and  $4d$  (right) for patient A.

#### 4.3.1.2 Crowns porosity map

Figure 4.6 shows the porosity profile along the radius of the aneurysm for patients A and B, where each curve reflects the porosity for each crown size (from  $0.25d$  to  $2d$ ). The x-axis reflects the radial center of the crown and  $x = 0$  mm is the wall of the aneurysm. The two patients show similar distribution: the porosity near the walls is close to 1 and decreases until a plateau around the mean porosity for  $x > 0.75$  or 1 mm (i.e. for  $x > 3d$  or  $4d$ ). The homogeneous center part (the bulk) represents around 50% of the total volume of the aneurysm for both patients. Even if the different crown sizes give similar results, the smallest one ( $0.25d$ ) seems most appropriate to capture the strong variations of the porosity close to the aneurysm wall, which have a strong impact on the modeling since the porosity, and consequently the permeability, are very large.

### 4.3.2 Permeability and inertial factor

#### 4.3.2.1 Permeability

The results of the permeability study for patient A and B are presented in Figure 4.7. The black circles, the yellow squares, and the green triangles represent respectively the dimensionless permeability along the  $x$ ,  $y$ , and  $z$  axis of the cubes. These directions are arbitrary. The large circle represents the mean permeability and porosity for the largest volume that fits in the aneurysm geometry. The blue line and the red line represent the estimates (SCE) given by equations (4.2) and (4.3) respectively. This figure shows that (i) numerical results of the permeability for  $4d$  cubes and

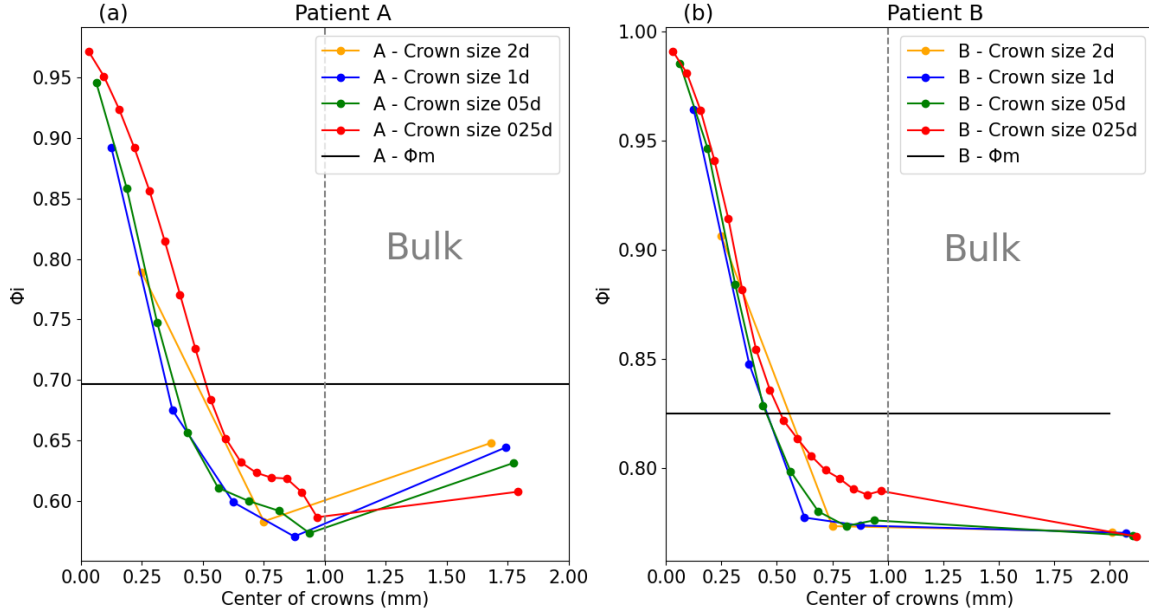


Figure 4.6: Porosity along the crowns for the two patients studied (patient A in the left and patient B in the right). The x-axis represents the center point of the crown, with  $x = 0$  mm being the aneurysm’s wall.

the largest volume are consistent with these estimates and (ii) the permeability anisotropy of each cube is small in comparison with permeability variation (around two decades) within the porosity range  $0.6 - 1$  of the coils (Figure 4.6). In this approximation, this anisotropy is neglected in the following. Overall, Figure 4.7 shows that the permeability of the coils can be well-fitted by the transverse estimate (4.3) with a coefficient of determination of  $R^2 = 0.75$ .

#### 4.3.2.2 Inertial factor

Figure 4.8 (a) presents, for Patient A (Patient B showed similar results), the evolution of the ratio between the mean velocity in each cube and the pressure gradient between inlet and outlet along  $x$ , depending on the value of the Reynolds number at the pore scale. The Reynolds number at the pore scale is calculated using the coil diameter as the characteristic length. Non-linear effects appear when the pore Reynolds number is larger than 1. According to *Barbour* [2018], the Reynolds number of the flow in the coil-treated aneurysm is around 10 at peak systole, therefore non-linear effects need to be considered. Numerical results on each cube (symbols) have been adjusted by the Darcy-Forchheimer (dashed line) equation in order to determine the inertial factor. Figure 4.8 (b) presents the evolution of the inertial factor with the porosity. Each symbol is the value of the inertial factor in one direction ( $x$ ,  $y$  or  $z$ ) for each cube and both patients, and the line represents the expression (4.4) adjusted on the

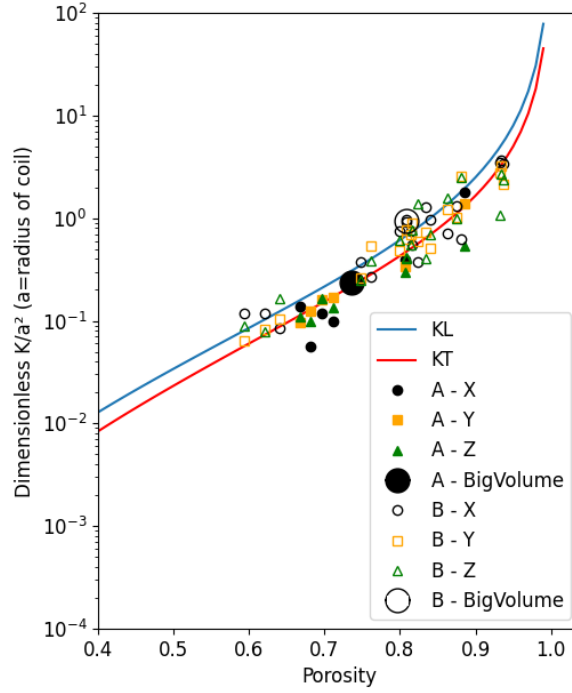


Figure 4.7: Dimensionless permeability results versus porosity on each cube for a  $4d$  cube size for patient A and B. The blue line and the red line represent the estimates (SCE) given by equations (4.2) and (4.3) respectively.

numerical data. As for the permeability, the anisotropy can be neglected in first approximation.

### 4.3.2.3 Permeability and inertial factor profile

Figure 4.9 shows the permeability and inertial factor profile along the crowns for Patients A and B. These profiles were computed from the crown porosity profiles (crown size is  $0.25d$ ) using equations (4.3) and (4.4). This figure shows that for both patient the permeability and inertial factor are strongly heterogeneous: the permeability typically varies over almost three order of magnitude, as does the inertial factor (from 0 to 30000 [1/m]). The horizontal dashed lines represent the permeability values  $K_m$ ,  $K_{op}$  and  $K_p$ ; and the inertial factor values  $C_{2m}$ ,  $C_{2op}$ ,  $C_{2p}$  of the three different porous models. As already mentioned, the classical porous model defined by  $K_m$  and  $C_{2m}$  based on the mean porosity is very far from the optimal values  $K_{op}$  and  $C_{2op}$ . The permeability is underestimated whereas the inertial factor is overestimated. By contrast, the values predicted by the crown porous model,  $K_p$  and  $C_{2p}$  are very close to the optimal values, therefore this model seems to be very accurate to represent the porosity heterogeneity of the coil mass in the aneurysm.

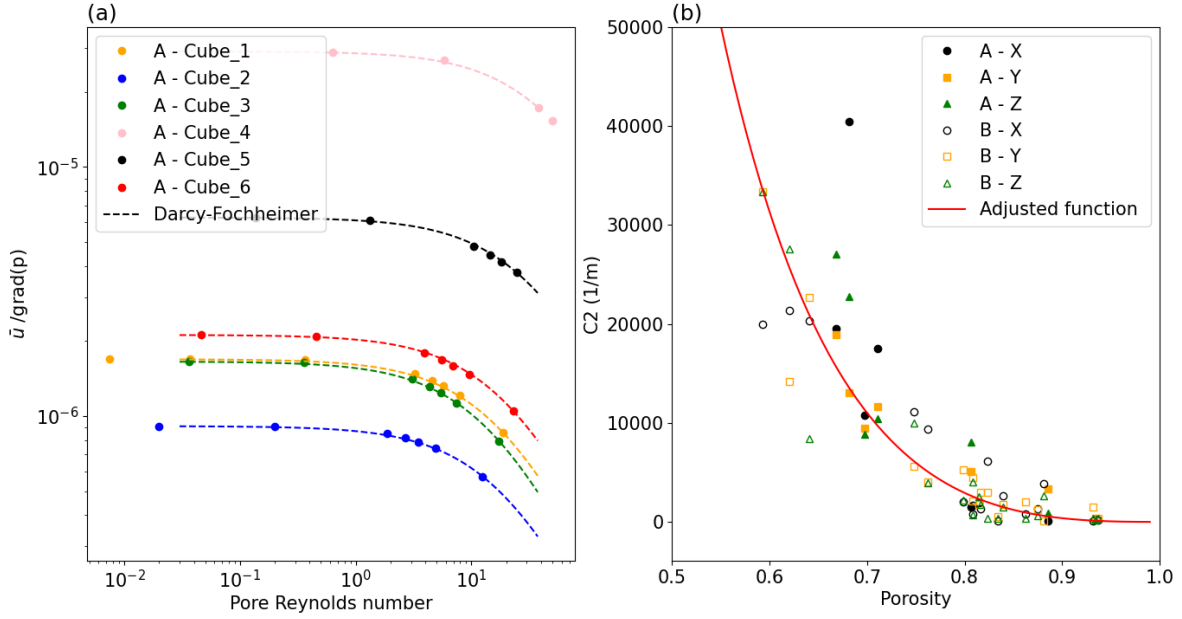


Figure 4.8: Figure (a) shows the evolution of the ratio between the mean velocity in the  $x$  direction and the gradient of pressure for each cube with the pore Reynolds number for Patient A. Dashed lines represent the Darcy-Forchheimer equation (4.1) adjusted on the numerical results (symbols). Figure (b) shows, for Patients A and B, the evolution of the inertial factor with the porosity deduced from the computations on each cube. The continuous line represents the adjusted equation (4.4)

### 4.3.3 CFD simulations

Table (4.5) presents the results of the CFD simulations for patients A and B: the percentage of error of the mean velocity in the aneurysm, with the coil-resolved values serving as gold standard.

- Case 1 - Porous model based on the mean porosity -  $K_m$  and  $C_{2m}$ : The results of the simulations for the porous medium based on the mean porosity are  $S0_m$  and  $S1_{mm}$  in Table (4.5). Both patients show similar results: the results of the Stokes flow simulations show 65% difference, and for the complete models for Patients A and B, the errors are 46 and 58% respectively. These results are consistent with the uncertainty reported in the literature [Levitt *et al.*, 2016] and confirm that the permeability and inertial factor based on the mean porosity are not sufficient to reproduce the mean blood velocity within coiled aneurysms.
- Case 2 - Optimal porous model -  $K_{op}$  and  $C_{2op}$ : The results for the optimal porous model simulations are  $S0_{op}$  and  $S1_{opop}$  in Table (4.5). The values of  $K_{op}$  and  $C_{2op}$  allow to reproduce the mean blood velocity within coiled

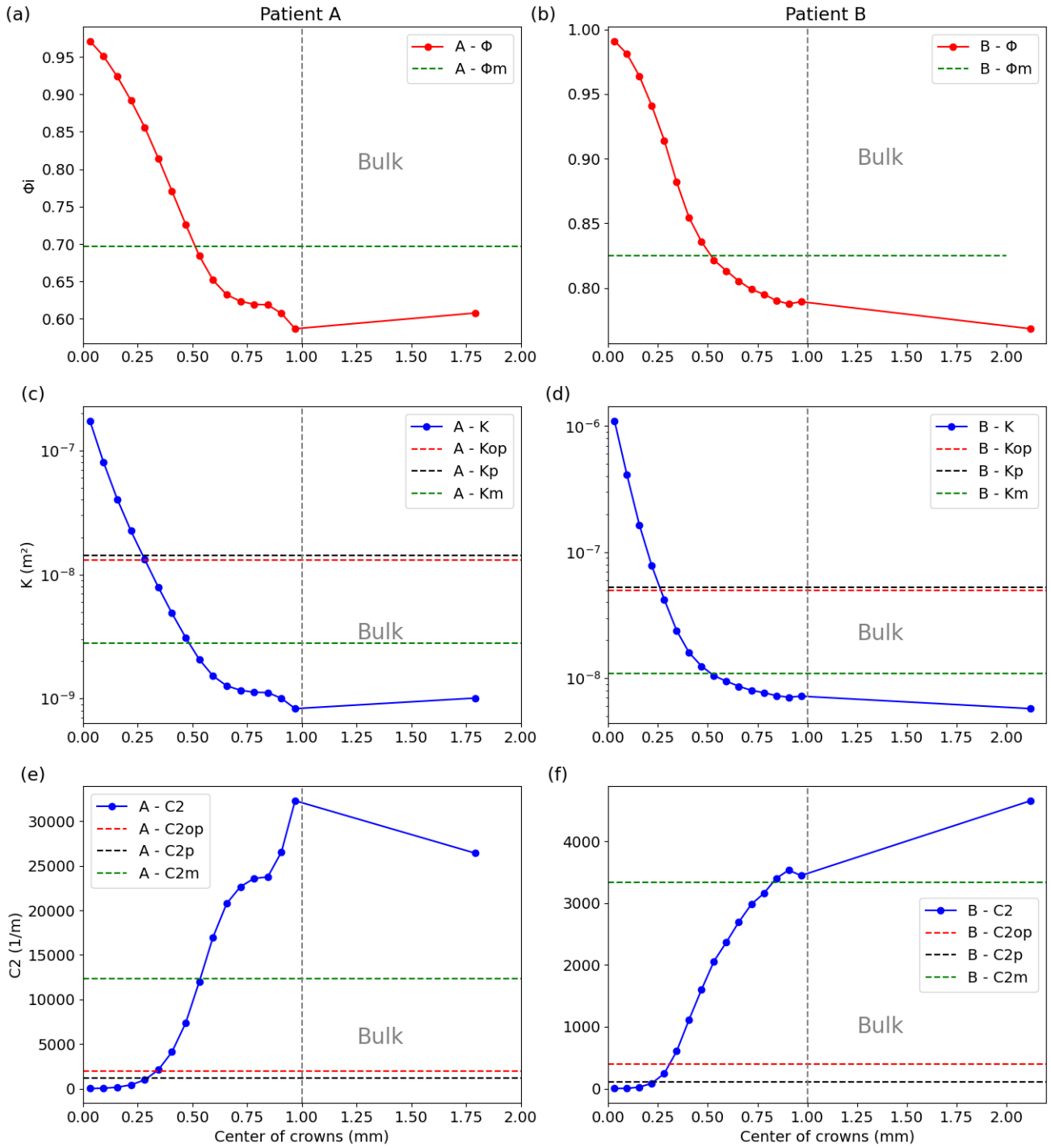


Figure 4.9: (a, b): Porosity profiles for the two patients (Number of crowns = 16, crown's size =  $0.25d$ ), corresponding permeability (c,d) and inertial factor (e,f) profiles given by equations (4.3) and (4.4) respectively. The bulk is separated from the crowns by a grey vertical dashed line. The horizontal dashed lines represent the permeability values  $K_m$ ,  $K_{op}$  and  $K_p$ ; and the inertial factor values  $C_{2m}$ ,  $C_{2op}$ ,  $C_{2p}$  of the three different porous models.

aneurysms with an error below 1%. Therefore, they can be considered as the best achievable simplified porous model (that uses the detailed information about the coil mass available only from synchrotron scans).

Stokes flow				
Patient	Model	Simulation name	Mean velocity in the aneurysm (m/s)	% of change mean velocity in the aneurysm
A	Coil-resolved	S0	$7.63 \cdot 10^{-7}$	
		$S0_m$	$2.57 \cdot 10^{-7}$	66.4
	Porous media	$S0_{op}$	$7.70 \cdot 10^{-7}$	-0.8
		$S0_p$	$7.82 \cdot 10^{-7}$	-2.4
B	Coil-resolved	S0	$4.61 \cdot 10^{-5}$	
		$S0_m$	$1.63 \cdot 10^{-5}$	65.6
	Porous media	$S0_{op}$	$4.60 \cdot 10^{-5}$	0.2
		$S0_p$	$4.74 \cdot 10^{-5}$	-2.9
Complete model				
A	Coil-resolved	S1	$2.12 \cdot 10^{-2}$	
		$S1_{mm}$	$8.82 \cdot 10^{-3}$	58.4
	Porous media	$S1_{opop}$	$2.11 \cdot 10^{-2}$	0.4
		$S1_{pm}$	$1.46 \cdot 10^{-2}$	31.2
	$S1_{pp}$	$2.25 \cdot 10^{-2}$	-5.9	
B	Coil-resolved	S1	$4.43 \cdot 10^{-2}$	
		$S1_{mm}$	$2.37 \cdot 10^{-2}$	46.4
	Porous media	$S1_{opop}$	$4.41 \cdot 10^{-2}$	0.3
		$S1_{pm}$	$3.14 \cdot 10^{-2}$	29.2
	$S1_{pp}$	$5.13 \cdot 10^{-2}$	-15.9	

Table 4.5: Summary of CFD results for patients A and B: Mean velocities in the aneurysm and percentage of change of the mean velocity. Coil-resolved simulations are used as references

- Case 3 - Porous crown model -  $K_p$  and  $C_{2p}$ : Focusing on the Stokes flow simulation (simulations  $S0_p$ ), the porous crown model for the permeability shows errors below 3% for both patients. From these results, we can confirm the accuracy of the porous crown model to define the permeability. These results are also supported by the complete model simulations (simulations  $S1_{pm}$ ) as they show that, when modifying only the permeability value, the mean velocity values in the aneurysm approximate the coil-resolved gold standard, decreasing the errors from  $\approx 65\%$  to  $\approx 30\%$  for both patients. However, this error is still significant, therefore it is also important to consider the heterogeneity of the

porous medium when defining the inertial factor. When the porous crown model is also used to define the inertial factor (simulations S1<sub>pp</sub>), the error decreases to 6% and 16% for patients A and B, respectively. Overall, these results clearly show that the porous crown model enables the simulation, with high accuracy, of the mean blood velocity within coiled aneurysms, even if it might need continuous improvements to further capture non-linear effects.

## 4.4 Discussion

A new porous model (the porous crown model) is proposed to describe the flow in cerebral aneurysms treated with embolic coils. We have shown, starting from 3D X-ray synchrotron images of coiled aneurysms to CFD simulations, that this model allows to capture the porosity heterogeneity of the coil within the aneurysmal sac and to predict with accuracy the mean blood velocity in the treated cerebral aneurysms.

This study is based on the combination between *in vivo* and *in vitro* models that contain realistic coiled aneurysm geometries from two patients. The error that is created during the 3D model creation process (clinical image segmentation, model making, etc.) has no impact on the results presented in this study [Chivukula *et al.*, 2019], since we are comparing results from *in silico* models (coil-resolved versus porous models) based on the same geometry. However, it would be interesting to validate the coil-resolved flow simulations against experimental measurements in the *in vitro* coiled-treated aneurysm.

One limitation concerning this part of the project, is the repeatability of the coil deployment in the aneurysm (inter-operator variability). The coil deployment may vary even for the same coils placed in the same order, and this variability would result in certain variations in the heterogeneous porosity distribution. For both Patients A and B, the same neurosurgeon performed the endovascular procedure. The inter-operator variability, between surgeons, is expected to be negligible as long as the treatment strategy is standardized in terms of how many coils are placed, which sizes, and the order of insertion. Thus, inter-operator variability is not expected to affect the outcome of this study. However, it is important to ensure that the same number of coils are deployed in the same order and that they occupy the volume inside the aneurysmal sac in the same way, to ensure that the porosity distribution does not fundamentally change among patients.

As it has been already underlined in previous studies [Yadollahi-Farsani *et al.*, 2019; C.Sadasivan *et al.*, 2018], the present work confirms that the heterogeneous distribution of the porosity must be included in porous models. As it is not possible to characterize the coils used in treatment of cerebral aneurysms from the clinical imaging scans, our method is based on 3D X-ray synchrotron images. This presents

a significant step towards understanding blood flow inside treated aneurysms as we have a realistic coil geometry.

Using the crown method, we have shown that the porosity gradient is very high in the first millimeter (equivalent to 3 or 4 coil diameters) near the wall and the neck, and the porosity is homogeneous in the rest of the aneurysm (bulk) for both patients. The bulk region represents around 50% of the total volume of the aneurysm. As in *Levitt et al.* [2016]; *Kakalis et al.* [2008]; *Mitsos et al.* [2008], the homogeneous isotropic porous medium model based on the mean porosity leads to large errors (around 50%) in terms of the mean velocity in comparison with the coil-resolved results (Table 4.5). Indeed, the blood flow within the aneurysm is highly impacted by the porosity heterogeneity near the wall and at the neck, i.e. where the porosity and the permeability are large, and the inertial factor is small. At the neck, this heterogeneity plays an important role on the fluid velocity at the inlet of the aneurysm, and consequently in the whole aneurysmal sac. The permeability and inertial factor defined in the porous crown model assume that the flow predominantly moves tangential to the crown (parallel flow). From the physical point of view, the blood penetrates in the aneurysmal sac through the neck, maintaining the same direction it had in the parent artery, and moves predominantly tangentially to the crowns, not normal to them, along the wall where the porosity is highest.

The evolution of the permeability and the inertial factor as function of the porosity have been determined numerically on representative elementary volumes of  $4d$  size extracted from the 3D X-ray images. The obtained results showed that the permeability of the coils, and thus of each crown, can be well estimated by the self consistent estimate (4.3) [*Boutin*, 2000], when the anisotropy is neglected in first approximation. This has been confirmed by the CFD simulations (Stokes flow) that lead to errors below 3% for both patients, instead of 60% in previous models [*Levitt et al.*, 2016]). The inertial factor expression of each crown has been estimated using the proposed relation (4.4). CFD simulations (pulsatile flow) have shown that the results are also improved when considering the heterogeneity of the porous medium, leading to an error lower than 16% (Table 4.5).

In the CFD simulations, the only hemodynamics metric used in the comparison between models was the mean velocity within the aneurysm. In porous models, it can be shown using upscaling methods [*Auriault et al.*, 2009] that this mean velocity is by definition equal to the volume average of the fluid velocity at the pore scale, i.e. the fluid velocity computed in coil-resolved simulations. This metric, also used in *Yadollahi-Farsani et al.* [2019], is thus relevant to validate porous models. This metric is also relevant to assess coil treatment outcomes and, more precisely, to predict thrombus formation (blood coagulation) which is linked to blood stagnation [*Luo et al.*, 2011]. Other hemodynamics metrics, such as residence time, shear integrated over the entire trajectory of platelets in the domain, and other

hemodynamics quantities linked with thrombosis are necessary to validate advanced porous models.

Overall, the proposed porous crown model represents a step forward towards clinical prediction of treatment outcomes, but only the results for two patients are presented in this work. More patients must be considered to further evaluate and analyze its robustness.

## 4.5 Conclusion

This study presents a novel homogeneous isotropic porous medium model to simulate coil-treated aneurysms, by defining the permeability and inertial factor based on a porous crown map. By considering the heterogeneity of the porosity distribution in these crowns, and the patient-specific boundary conditions, the mean velocity of the blood in the porous model is predicted with high accuracy, when compared with the gold-standard coil-resolved simulations. This model could eventually be employed in future CFD studies of coiled cerebral aneurysms for treatment planning and outcome prediction.

---

## Towards prediction of blood flow in coiled aneurysms before treatment

---

### Contents

5.1	Introduction . . . . .	87
5.2	Methods . . . . .	89
5.2.1	Model creation . . . . .	89
5.2.2	Definition of the porous model . . . . .	90
5.2.3	Computational fluid dynamics: comparison of the coil-resolved and porous medium models . . . . .	97
5.3	Results . . . . .	105
5.4	Discussion . . . . .	111
5.5	Conclusion . . . . .	115

---

### Abstract

Modeling blood flow in aneurysms treated with coils could be used to understand the parameters involved in a complete embolization of the aneurysm, through thrombus formation that fills the entire sac. Porous medium modeling of the endovascular coil mass is a technique to solve this problem, as it could allow for the study of the hemodynamics in the aneurysm and be used for patient-specific treatment outcome prediction. The porous models developed up to date in the literature are only based on the mean porosity of the aneurysmal volume filled with coils and have proven not to be accurate enough. In Chapter 4, we have presented a methodology to create a porous model (porous crown models), considering the heterogeneous distribution of the coils. The objectives of this study are (i) to validate the porous crown model for a larger cohort (eight patients), and (ii) to propose a porous media model that could

be used in clinical practice to evaluate the treatment before surgery. Following the methodology of Chapter 4, we calculate the permeability and inertial factor for each patient to define the crown’s porous model. We propose a new porous model, the bilinear model, that uses the same flow hypothesis as in the porous crown model. However, the permeability and inertial factor can be defined from basic information available in the neuro-suite, i.e. the size of the aneurysmal sac and the target porosity given by the surgeon. These two models are validated by comparing them to the coil-resolved model simulations, which is considered the gold standard. The results show that both the porous crown model and the bilinear model seems to be accurate to simulate blood flow in the aneurysm. Some adjustments need to be done but the bilinear model seems promising to better evaluate treatment outcomes at the neuro-suite.

## 5.1 Introduction

Endovascular coiling is one of the most common, safe and effective techniques to treat the cerebral aneurysm. It consists of deploying platinum coils inside the aneurysmal sac. These coils are introduced in the neurovasculature through a catheter inserted in the femoral artery and navigated through a guide wire under fluoroscopy guidance until the tip reaches the Circle of Willis artery where the aneurysm is located. The purpose of the coils is to slow down blood flow inside the aneurysmal sac, promoting the formation of a stable thrombus that fills the entire aneurysm volume. The aneurysm is thus isolated from blood flow circulation and the corresponding hemodynamics stresses. This stops aneurysm growth and prevents rupture and internal hemorrhage [Guglielmi *et al.*, 1991]. This technique is commonly used as it is non-invasive and typically associated with fast patient recovery after treatment. However, there is a 20% risk of recanalization after treatment [Etminan and Rinkel, 2016; Seibert *et al.*, 2011]. Insufficient packing density was studied as a possible cause of recurrence. Studies have shown that 20-30% should be the target packing density to ensure stable thrombus formation, while avoiding disturbing the flow in the parent vessel. At that packing density, recanalization is still a risk [Crobeddu *et al.*, 2013].

Hemodynamics has been implicated in cerebral aneurysm growth and rupture [Meng *et al.*, 2007]. Studying hemodynamics in coiled aneurysms can determine the hemodynamics parameters related to recanalization. A computational model of aneurysms treated with endovascular coiling can be used to determine the relationship between hemodynamics and recanalization, and to predict treatment outcomes before treatment in the neuro-suite.

The first challenge when modeling blood flow in cerebral aneurysms treated with coils is to create an accurate numerical model that represents the anatomy

and physiology. The coils' geometry cannot be reproduced from clinical CT scans. There are two approaches in the literature for creating numerical models of the coils exact geometry. The first one consists of using Finite Element Modeling software to deploy virtually an endovascular coil in the aneurysm geometry segmented from patient medical imaging [Yadollahi-Farsani *et al.*, 2019]. The second method consists of obtaining the geometry of the coils through high-energy scans (synchrotron microtomography) of 3D printed aneurysmal phantoms treated with real clinical coils and creating a numerical coil-resolved model [Levitt *et al.*, 2016]. Both models reproduce the anatomy of the patient numerically. In the second method, the surgeon placing the coils in the aneurysm during surgery also deploys the same coil sequence in the phantom artery, ensuring that the numerical model reproduces the coils configuration in the patient. The two types of accurate physiological numerical model require the geometry of the coils, as well as high computational power to model blood flow in the aneurysm at that level of spatial resolution, therefore, they cannot be used for clinical predictions. Modeling the aneurysm treated with coils as a porous medium is a promising alternative to perform simulations in a clinically-relevant time and to predict blood flow within the aneurysmal sac before treatment.

Previous studies have developed a porous media model for blood flow in coiled aneurysms. In those studies, the aneurysm was considered as a homogeneous isotropic porous medium, where the parameters characterizing the medium (permeability and inertial factor) depend only on the mean porosity in the aneurysm [Kakalis *et al.*, 2008; Mitsos *et al.*, 2008; Levitt *et al.*, 2016]. In Levitt *et al.* [2016], the coil-resolved model was compared against the standard porous model. The results show that the standard homogeneous, isotropic porous model is not accurate in representing blood flow inside coiled aneurysms. The heterogeneous porosity distribution of the coils, resulting from the random deployment of the coils and the porosity gradient close to the aneurysm wall, are neglected in the standard model, which explains the deviation from the coil-resolved model that is physiologically and anatomically accurate.

Yadollahi-Farsani *et al.* [2019] developed a porous medium model that considers the heterogeneous porosity distribution of the coils. They defined the porous medium with a spatial discretization, where each element was defined by a porosity and permeability value. The size of the elements vary and the results of that study showed that including the heterogeneity improved the flow prediction when compared to the coil-resolved numerical model. In particular, for a smaller element sizes, the approximation of the flow characteristics became more accurate. However, this porous approach requires knowledge of the exact geometry of the coils to establish the porosity and permeability values, and therefore cannot be used for clinical prediction.

In the previous chapter (see Chapter 4), we developed a porous model to reproduce blood flow in an aneurysm with coils: the porous crown model. This model is a

homogeneous isotropic porous medium, which includes the heterogeneity of the porosity distribution in the permeability and inertial factor definition. This model was validated only for two patients and cannot be used for prediction as it also requires knowledge of the exact geometry of the coils deployed in the aneurysm, to define the properties of the porous medium model. The purpose of this study is (i) to validate the porous crown model for a larger cohort of patients and (ii) to propose a porous model that could be used for the prediction of the treatment outcome in the neuro-suite. In the neuro-suite, the CT scans provide the segmentation for the aneurysm and parent vessel wall anatomy, and the dimensions of the aneurysm (volume, depth, neck area, curvature, etc). The surgeon chooses the number of coils to deployed in the aneurysm to aim a certain volume fraction ( $\sim 0.7$ ) inside the aneurysmal sac. The objective is to use these available metrics to define a porous model for simulation of blood flow in coiled aneurysms.

## 5.2 Methods

### 5.2.1 Model creation

Eight patients participated in this study. They enrolled at the University of Washington Harborview Medical Center in Seattle (WA, USA) all of them presenting cerebral aneurysms with diameters above 5 mm measured in the neuro-suite. Patients' anthropometrics can be found in Table 5.1. The patients' aneurysms were treated with endovascular coiling (Stryker Endovascular, Kalamazoo, Michigan, USA). Each patient received a different treatment (number of coils varied as well as their dimensions), which was decided by the surgeon adapting it to each pathology. The lengths of the coils varied from 2 to 30 cm and the diameters varied from 240 to 250  $\mu\text{m}$ .

Coils' geometry cannot be reconstructed from CT scans available clinically after being deployed in the patient's aneurysm. Following the previous work at the University of Washington [Levitt *et al.*, 2016; Barbour, 2018], we created a physical silicone model of the patients' anatomy, treated this flow phantom with the exact same coil as the patient received in clinical treatment, and scan it in the ESRF (Grenoble, France) synchrotron.

The three-dimensional angiography scans of the aneurysm and parent vessel for each patient were segmented. A 1:1 scale positive mold was 3D printed in acrylonitrile butadiene styrene, and cast in a transparent polyester resin (PDMA, Clear-Lite, TAP plastics, San Leandro, California, USA), creating an accurate model of the patient's anatomy. The *in vitro* model was treated with the same treatment that the patient and following the same technique: the same number of coils was deployed and in the same order.

The treated models were then scanned at beamline ID19 of the European Synchrotron Radiation Facility (<http://www.esrf.eu>) in Grenoble (France). The image resolution of the eight scans was approximately 13  $\mu\text{m}$ . After performing image segmentation of the aneurysm model scans, the geometry of the coils was reconstructed and positioned in the 3D numerical model. To achieve these, the centerlines of the parent vessel in the 3D numerical model and in the treated model scans were extracted using Vascular Modeling Toolkit software (<http://www.vmtk.org>). Transformation matrices between the two centerlines were found using the Iterative Closest Point method in MATLAB [Wilm, 2020] (MathWorks, Inc., Natick, Massachusetts, USA) and were applied to the geometry of the coils, repositioning the coils onto the aneurysm. The complete 3D numerical models after coil repositioning for the 8 patients are presented in Figure 5.1.

Patient	Measurements from the CT scans				Model
	Aneurysm volume ( $\text{mm}^3$ )	$\phi_m$	$a_1(\text{mm})$	$a_2(\text{mm})$	Ellipsoid volume ( $\text{mm}^3$ )
A	45.7	0.697	5.2	4.0	44.6
B	107.1	0.825	6.6	5.9	121.3
C	93.7	0.772	6.8	5.2	94.9
D	90.0	0.715	6.2	5.8	107.5
E	32.9	0.678	4.5	3.8	34.5
F	38.2	0.720	4.8	3.9	38.2
G	413.3	0.795	11.4	8.7	454.1
H	279.9	0.788	11.7	6.8	283.8

Table 5.1: Anthropometrics of the aneurysm for Patients A to H: aneurysm volume, mean porosity in the aneurysm  $\phi_m$ , ellipsoid volume ( $4/3\pi a_1 a_2^2$ ),  $a_1$  being the length of the major axis of the aneurysm, and  $a_2$  being the length of the minor axis of the aneurysm.

## 5.2.2 Definition of the porous model

### 5.2.2.1 Porosity profile

To define the porous model, we analyzed first the porosity distribution radially. The porous media was defined as the intersection between the coil mass envelope and the aneurysm's parent vessel geometry. That envelope was defined using MATLAB and implemented in the 3D numerical model using StarCCM+ (Siemens, Melville, New-York, USA). The aneurysm with coils was transformed into image stack format using ImageJ, as the porosity analysis was done via image treatment techniques. The mean porosity  $\phi_m$  values can be found on Table 5.1 and were calculated by counting the number of voxels filled with coils (white) or with blood (grey) (see Figure 5.2).

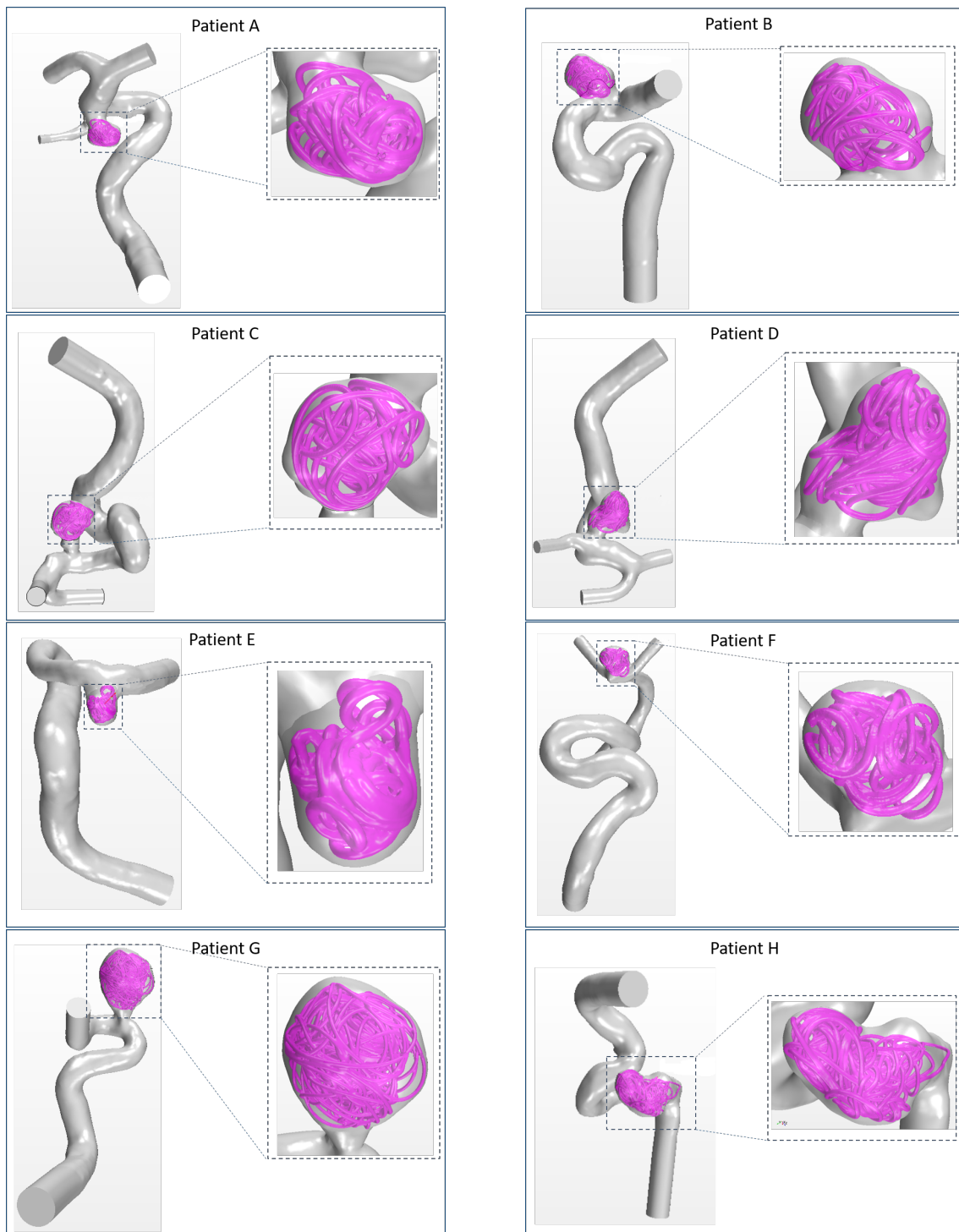


Figure 5.1: 3D models of the patients after coils positioning. For each patient, the longest side of the parent vessel is the inlet, and the shorter side the outlet. The number of outlets vary from one patient to the other depending on the original location of the aneurysm.

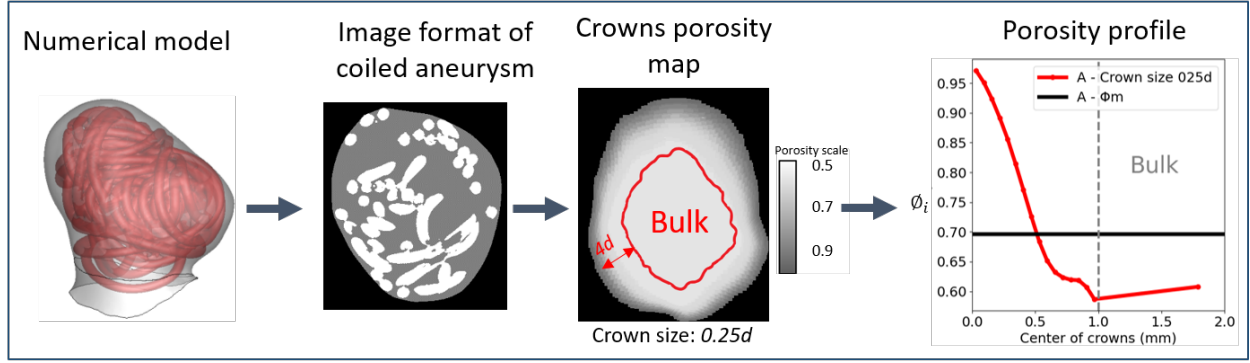


Figure 5.2: Porosity analysis process for patient A: from the 3D numerical model to the porosity profile.

The porosity was analyzed radially with a crown's porosity map. The crowns were defined by eroding the porous medium (aneurysm with coils) using MATLAB, with recursive homothetic transformations of the aneurysmal wall. The eroded region was a crown, and four different crown sizes were analyzed:  $0.25d$ ,  $0.5d$ ,  $1d$ ,  $2d$ , where  $d$  is the diameter of the coils ( $250 \mu\text{m}$ ). The thickness of all the crowns was  $4d$  ( $1 \text{ mm}$ ) and the bulk was considered homogeneous. The porosity was calculated for each of the crowns and the bulk. Figure 5.2 illustrates the crown porosity map and the corresponding porosity profile for patient A.

The porosity profiles of the crown porous maps for a crown size of  $0.25d$  of the patients are plotted on Figure 5.3. All the patients show a similar trend: the porosity is high near the wall and decreases almost linearly until stabilized between  $0.5$  and  $1 \text{ mm}$ . The decision of characterizing the porosity with this method was discussed in Chapter 4, and is used to define the porous flow parameters (permeability and inertial factor), as explained in the following section.

### 5.2.2.2 Porous crown model

Flow through coiled aneurysms modeled as a porous medium can be approached with Darcy-Forchheimer equation (5.1) for homogeneous isotropic porous medium as it has previously been done in the literature [Levitt *et al.*, 2016; Mitsos *et al.*, 2008; Kakalis *et al.*, 2008]:

$$\nabla p = -\frac{\mu}{K}\mathbf{u} - \frac{1}{2}\rho C_2|\mathbf{u}|\mathbf{u} \quad (5.1)$$

where  $\rho$  is the fluid density ( $\text{kg/m}^3$ ),  $\nabla p$  is the pressure gradient ( $\text{Pa/m}$ ),  $\mu$  the fluid viscosity ( $\text{Pa}\cdot\text{s}$ ),  $\mathbf{u}$  is the fluid velocity (Darcy's velocity, in  $\text{m/s}$ ) and  $K$  ( $\text{m}^2$ ) and  $C_2$  ( $1/\text{m}$ ) are the permeability and inertial factor coefficient, respectively.

To define the aneurysm with coils as a porous medium, we need to define the permeability and the inertial factor. The porous models available in the literature

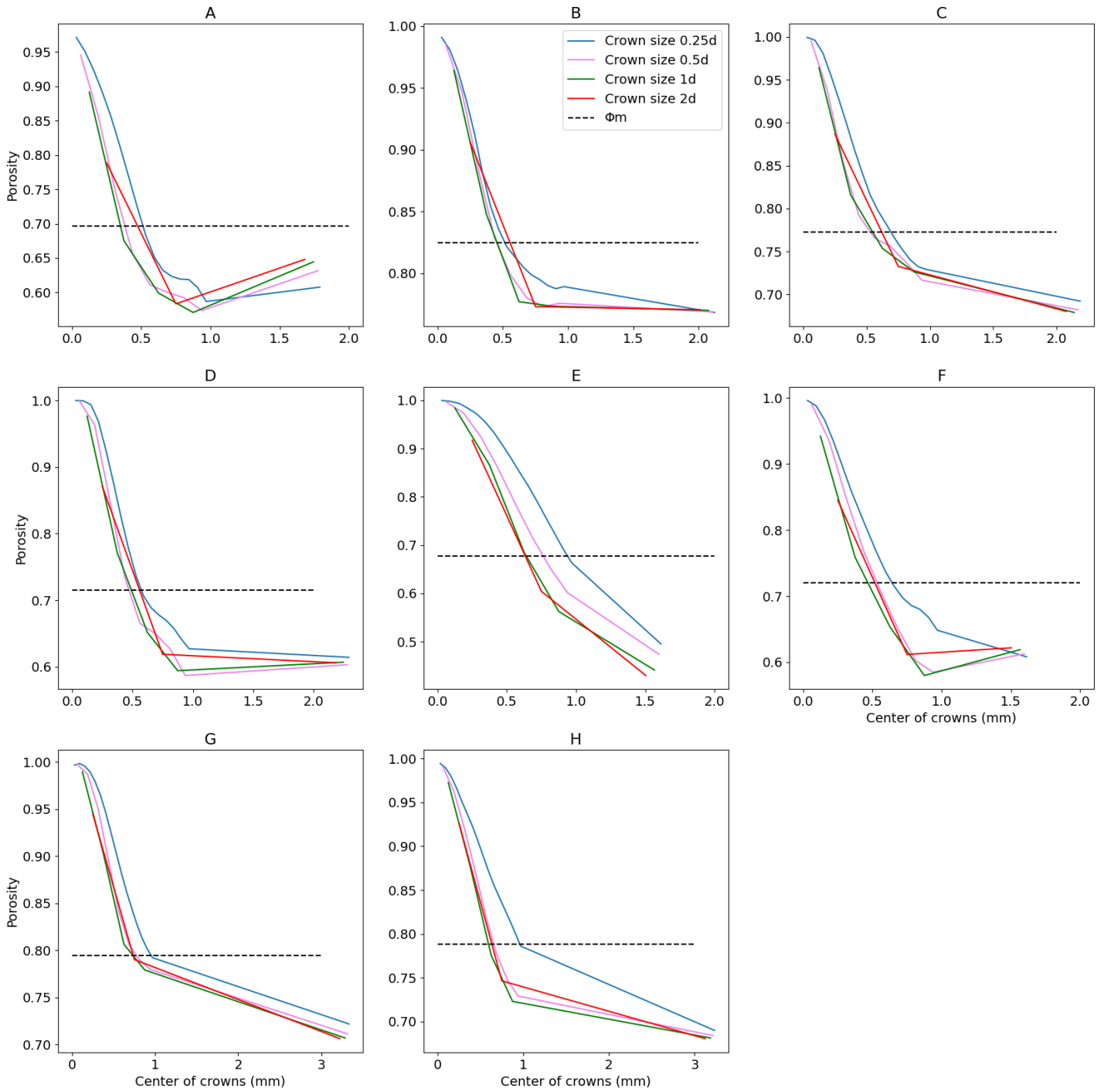


Figure 5.3: Porosity along the crowns for eight patients. The x-axis represents the center point of the crown, with  $x = 0$  mm being the aneurysm's wall. The four crown sizes are presented  $0.25d$ ,  $0.5d$ ,  $1d$  and  $2d$ .

used permeability and inertial factor values based on the mean porosity ( $\phi_m$ ) only. However, these models did not include the heterogeneity of the porosity distribution and therefore the computational fluid dynamics (CFD) comparison to the coil-resolved model was not satisfactory. In the preceding Chapter 4, we presented the porous crown model that allows the cerebral aneurysm treated with coils to be modeled as a homogeneous isotropic porous medium while considering the heterogeneity of the porosity distribution. The model was validated only for two patients. The objective is to analyze the porous crown model for a larger number of patients, providing higher anatomical, physiological and treatment variability. The method to calculate the permeability and inertial factor of the crown porosity model developed in Chapter 4 is as follows.

The model establishes that the flow propagates predominantly tangential to the crowns, defined in the previous section (see Figure 5.2). The permeability and the inertial factor in this model can be calculated following equation (5.2) based on published data from a model arising from homogenization [Auriault *et al.*, 2007].

$$K_p = \sum_1^N f_i K_i + f_b K_b \quad C_{2p} = \left( \sum_1^N \frac{f_i}{\sqrt{C_{2i}}} + \frac{f_b}{\sqrt{C_{2b}}} \right)^{-2} \quad (5.2)$$

where  $K_i$ ,  $C_{2i}$  and  $f_i$  are the permeability, the inertial factor, and the volume fraction for the  $i$ th crown and  $N$  is the number of crowns.  $K_b$ ,  $C_{2b}$  and  $f_b$  are the permeability, the inertial factor, and the volume fraction for the homogeneous center (bulk).

The permeability  $K_i$  and  $K_b$  are calculated based on the self-consistent estimate established by *Boutin* [2000] for perpendicular flow through cylindrical bundles, as in equation (5.3), where  $a = d/2$ . The inertial factors  $C_{2i}$  and  $C_{2b}$  are computed from the equation (5.4), where the permeability  $K_T$  is given by the equation (5.3).

$$K_T = \frac{a^2}{8(1-\phi)} \left( -\ln(1-\phi) - \frac{(1-(1-\phi)^2)}{(1+(1-\phi)^2)} \right) \quad (5.3)$$

$$C_2(\phi) = \frac{2}{\sqrt{K_T(\phi)}} 3(1-\phi)^2 \quad (5.4)$$

If the flow hadn't been considered tangential to the crowns and would have been perpendicular to the crowns, the permeability and inertial factor would have been defined as follows:

$$K_s = \left( \sum_1^N \frac{f_i}{K_i} + \frac{f_b}{K_b} \right)^{-1} \quad C_{2s} = \sum_1^N f_i C_{2i} + f_b C_{2b} \quad (5.5)$$

To define the permeability and inertial factor, we need to define the crown size. In Chapter 4, the crown size that optimally represented blood flow in the aneurysm for Patients A and B was  $0.25d$ . However, it can vary from one patient to another. Indeed, if we analyze the porosity profiles for the patients in Figure 5.3 plotted for

a crown size of  $0.25d$ , we observe that the porosity decrease almost linearly from the first crown to the bulk of the aneurysm, for Patient A, B and H. However, the other patients present a different pattern. Indeed, for those patients, in the first crowns, there seems to be a plateau of the porosity values near 1 and then a linear decrease until reaching the bulk. The size of this plateau varies from one patient to another and it is due to the empty space inside the aneurysmal sac due to its anatomy, and to the space due to the coil positioning. Indeed, in the construction of the mesh, the coil geometry and the wall of the aneurysm are not always in contact, therefore, "artificial" space that is not representative of the aneurysm with coils are created. This effect is amplified for small crown sizes ( $0.25d$ ), as seen in Figure 5.3. In those cases, the porosity near the wall is very high, which affects the calculation of the permeability resulting in very high values (see equation 5.3). This is not representative of blood flow in the aneurysm with coils. For this reason, the crown size defined for each patient to calculate the permeability and the inertial factor is the size that eliminates the plateau (when  $\phi \rightarrow 1$ ). The details of the crown size chosen and the permeability values for each crown size can be found in Table 5.2.

Figures 5.7 and 5.8 show the permeability and inertial profiles calculated from the crown porosity profile using equations (5.3) and (5.4). In the same figures, the permeability and inertial factor of the porous crown model are plotted for each patient ( $K_p$  and  $C_{2p}$ ).

Patient	Porosity	$K_{p0.25d}$ (m <sup>2</sup> )	$K_{p0.5d}$ (m <sup>2</sup> )	$K_{p1d}$ (m <sup>2</sup> )	$K_{p2d}$ (m <sup>2</sup> )	Crown size
A	0.70	<b>1.42</b> 10 <sup>-8</sup>	9.64 10 <sup>-9</sup>	6.06 10 <sup>-9</sup>	3.17 10 <sup>-9</sup>	0.25d
B	0.83	<b>5.28</b> 10 <sup>-8</sup>	4.74 10 <sup>-8</sup>	2.74 10 <sup>-8</sup>	1.31 10 <sup>-8</sup>	0.25d
C	0.77	7.72 10 <sup>-7</sup>	1.51 10 <sup>-7</sup>	<b>2.49</b> 10 <sup>-8</sup>	8.78 10 <sup>-9</sup>	1d
D	0.72	1.45 10 <sup>-5</sup>	1.0 10 <sup>-6</sup>	<b>4.25</b> 10 <sup>-8</sup>	6.51 10 <sup>-9</sup>	1d
E	0.68	1.31 10 <sup>-6</sup>	3.01 10 <sup>-7</sup>	8.79 10 <sup>-8</sup>	<b>1.61</b> 10 <sup>-8</sup>	2d
F	0.72	1.23 10 <sup>-7</sup>	7.31 10 <sup>-8</sup>	<b>1.51</b> 10 <sup>-8</sup>	5.64 10 <sup>-9</sup>	1d
G	0.79	2.31 10 <sup>-7</sup>	2.24 10 <sup>-7</sup>	<b>8.04</b> 10 <sup>-8</sup>	1.76 10 <sup>-8</sup>	1d
H	0.79	<b>7.46</b> 10 <sup>-8</sup>	6.70 10 <sup>-8</sup>	3.29 10 <sup>-8</sup>	1.45 10 <sup>-8</sup>	0.25d

Table 5.2: Permeability calculated for each crown size (from  $0.25d$  to  $2d$ ) with the porous crown model equations 5.2. The last column is the crown size chosen for each patient.

### 5.2.2.3 Bilinear porous approximation

The CFD validation done in the previous chapter shows that the porous crown model allows modeling the aneurysm with coils as a homogeneous, isotropic porous medium model while considering the heterogeneous distribution of the porous media. However, to define the flow parameters of the porous model (permeability and

inertial factor), the geometry of the coils is needed and therefore cannot be used for prediction of the treatment outcomes before the coils are deployed in the aneurysm.

The objective is to create a porous medium model based on the crown model that can be used for treatment outcome prediction: where the permeability and the inertial factor can be defined without the need for the geometry of the coils. When studying the crown porosity map, as previously discussed, all the patients present the same trend. The porosity is high near the wall and, for most of the patients, decreases almost linearly until stabilizing around a porosity value at a distance  $t$  from the aneurysm wall, where  $t$  value oscillates between 0.5 mm and 1 mm.

The goal was to define a bilinear porous model that reproduces the crown porosity profile where; for a  $t$  fixed value, the porosity in the crowns linearly decreases and then stabilizes at its minimum value  $\phi_{min}$  in the homogeneous bulk (see Figure 5.6). The permeability and inertial factor of the equivalent homogeneous isotropic porous model are then calculated following equations (5.3) and (5.4) respectively. In this porous model, the permeability and inertial factor are patient-specific and can be defined with data available in the neuro-suite, which allows to use it for treatment outcomes prediction. The full process to define the bilinear porous model is shown in Figure 5.4. The hypotheses to define the bilinear porous model are the following:

- The aneurysm volume is approximated as an ellipsoid of revolution, where the major axis corresponds to the longest dimension of the aneurysmal sac (principal inertial axis of the aneurysm), and that the minor axes of the ellipsoid corresponds to the smallest inertial axis of the aneurysm. The dimensions of the aneurysm can be measured in the neuro-suite therefore this approximation will allow to estimate the volume fraction of each crown ( $f_i$  and  $f_b$  in equation (5.2)). The measures can be found in Table 5.1. Figure 5.5 shows the comparison between the aneurysm volume and the ellipsoidal approximation. For the small aneurysms' volumes, the approximation seems accurate, however, there is a larger difference when looking at higher volumes. When increasing the aneurysm and the ellipsoid volume, the absolute difference increases due to the fact that the values are higher, however the relative error between the aneurysm volume and the ellipsoid volume is constant over all the patients. Therefore, the ellipsoid volume approximation seems to be well suited to model the aneurysm anatomy in the creation of this porous medium model.
- The mean porosity is known as it is the value targeted by the surgeon, which is considered as the true value in first approximation. For this study, we will consider that the mean porosity  $\phi_m$  measured is the target porosity.
- $t$ , the region where the porosity linearly decreases, is fixed.  $t$  will be defined below.

- The number of crowns ( $N$ ) is fixed, therefore, the porosity decreases linearly for  $N$  crowns and stabilizes in the bulk.
- The porosity  $\phi_{wall}$  at the wall is supposed to be 1.
- The crowns in the ellipsoid model are defined by doing homothetic transformations of the ellipsoid volume with a displacement from the original equal to the crown thickness of  $0.25d$ . In the bilinear porous model, the border effects due to the positioning of the coils in the aneurysm are not considered. Therefore, we chose the smallest crown size to increase the accuracy in the calculations of the permeability and inertial factor.

Considering these hypotheses, the porosity in the bulk  $\phi_{min}$  is defined as:

$$\phi_{min} = \frac{\phi_m + \sum_0^N f_i \frac{2i+1}{2N} - \sum_0^N f_i}{f_b + \sum_0^N f_i \frac{2i+1}{2N}} \quad (5.6)$$

where  $N$  is the number of crowns,  $f_i$  is the volume fraction of the  $i$ th crown of the ellipsoidal volume,  $i$  is the crown number and  $f_b$  is the volume fraction of the bulk. To define  $t$ , the bilinear porosity profile was calculated for  $t=0.5$  mm,  $t=0.75$  mm and  $t=1$  mm. The results of the comparison between the bilinear porous model and the measured porosity profile are shown in Figure 5.6. The bilinear porous model that seems to reproduce the porosity profile model is the one with  $t=0.5$  mm, therefore for the rest of the study, we considered that the bilinear model is defined for  $t=0.5$  mm.

As for the porous crown model, the coiled aneurysm is considered as a homogeneous isotropic porous medium model, where the blood flow can be described with the Darcy-Forchheimer equation (5.1). The permeability and inertial factor of the bilinear model,  $K_{bi}$  and  $C_{2bi}$  respectively, were defined as it was previously done in the crown model, with equations (5.2), (5.3) and (5.4). Figure 5.7 shows the permeability profile, as well as the bilinear permeability profile, calculated for  $t=0.5$  mm for the eight patients. This figure also shows the permeability of the bilinear model  $K_{bi}$  associated with each patient. Figure 5.8 shows the inertial factor profile calculated in the images and the bilinear inertial factor profile calculated for  $t=0.5$  mm. It also presents the value  $C_{2bi}$  associated with each patient.

### 5.2.3 Computational fluid dynamics: comparison of the coil-resolved and porous medium models

#### 5.2.3.1 Reference model: Coil-resolved

The purpose of the study is to model the aneurysm with coils as a porous medium. However, an anatomically and physiologically accurate model was used as a reference

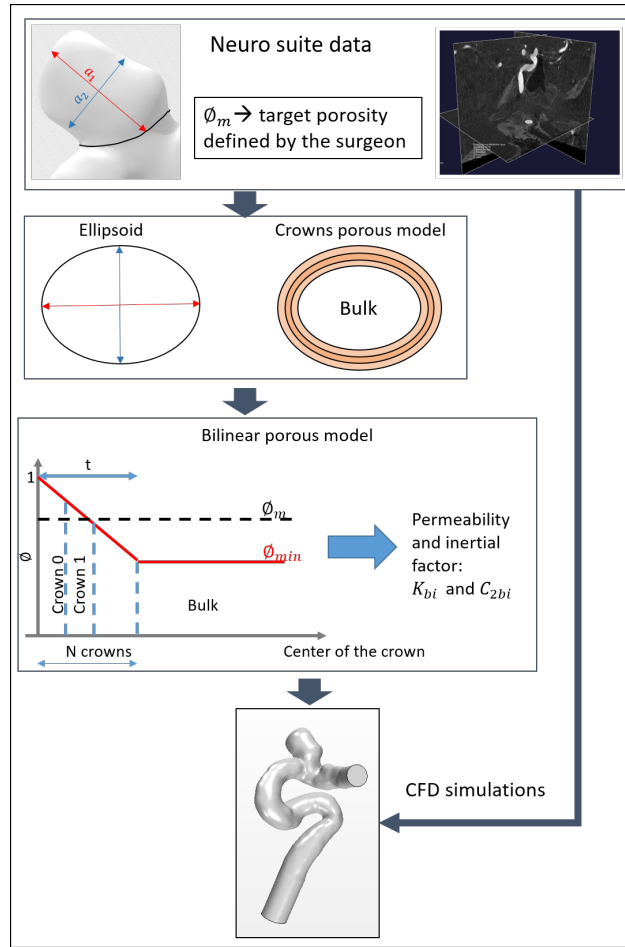


Figure 5.4: Full process to build the bilinear porous model: from the data available in the neuro-suite to the numerical model.

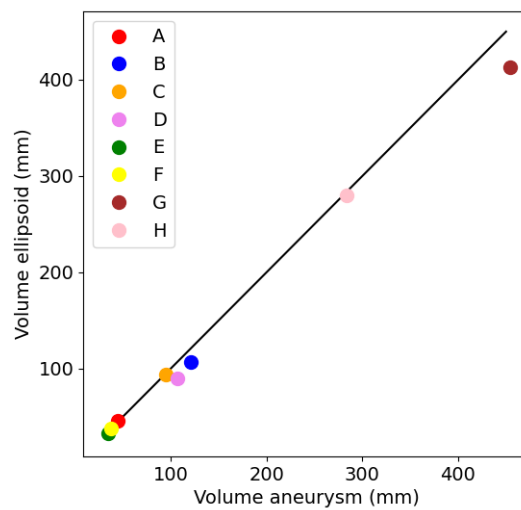


Figure 5.5: Comparison between the aneurysm volume and the ellipsoid volume approximation for the eight patients.

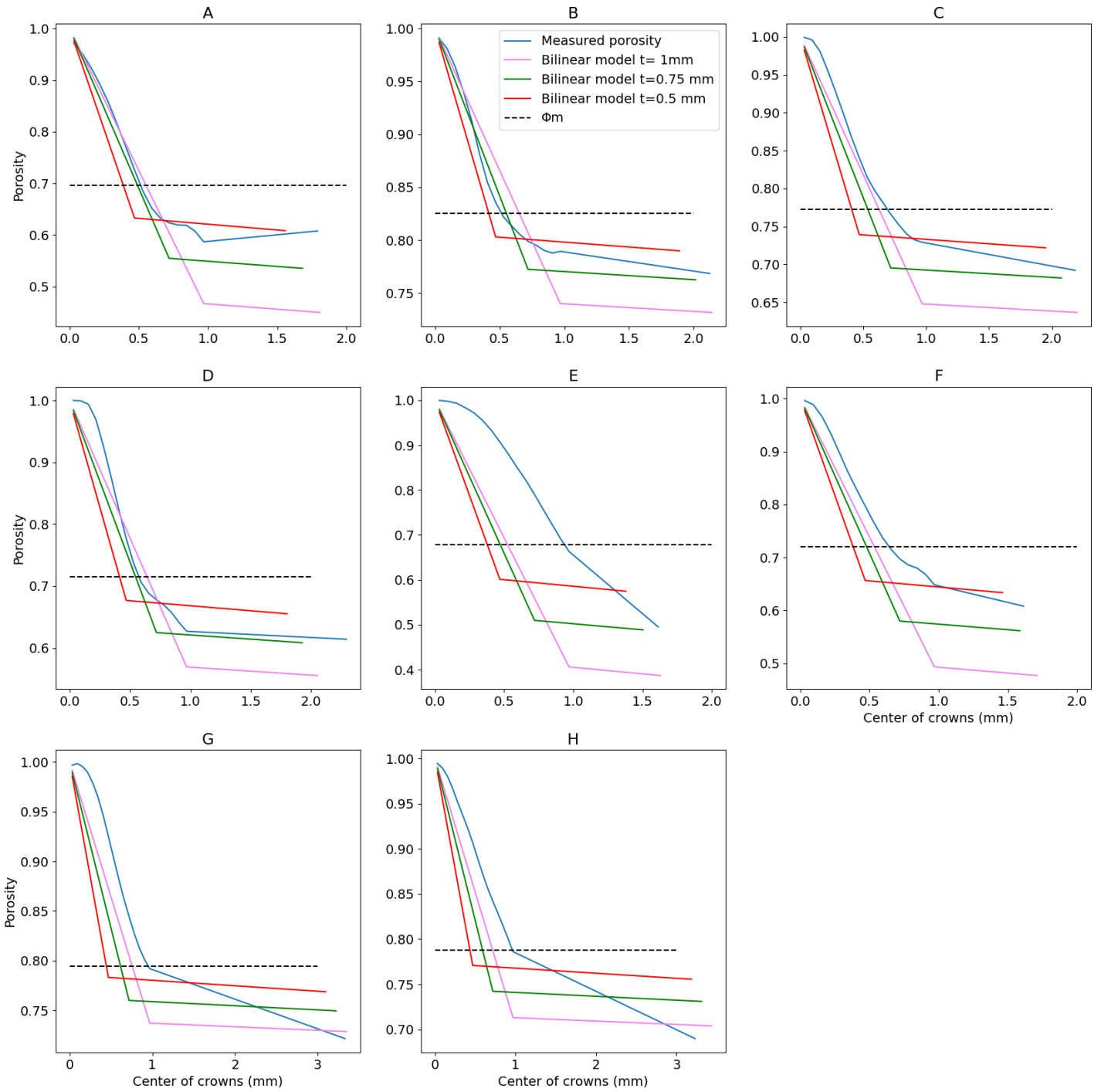


Figure 5.6: Radial porosity profile for the eight patients. The porosity is measured along the crowns, when the crown size is  $0.25d$  ( $d$  is the diameter of the coil). The bilinear porosity profiles for  $t=0.5\text{mm}$ ,  $t=0.75\text{mm}$ ,  $t=1\text{mm}$ .

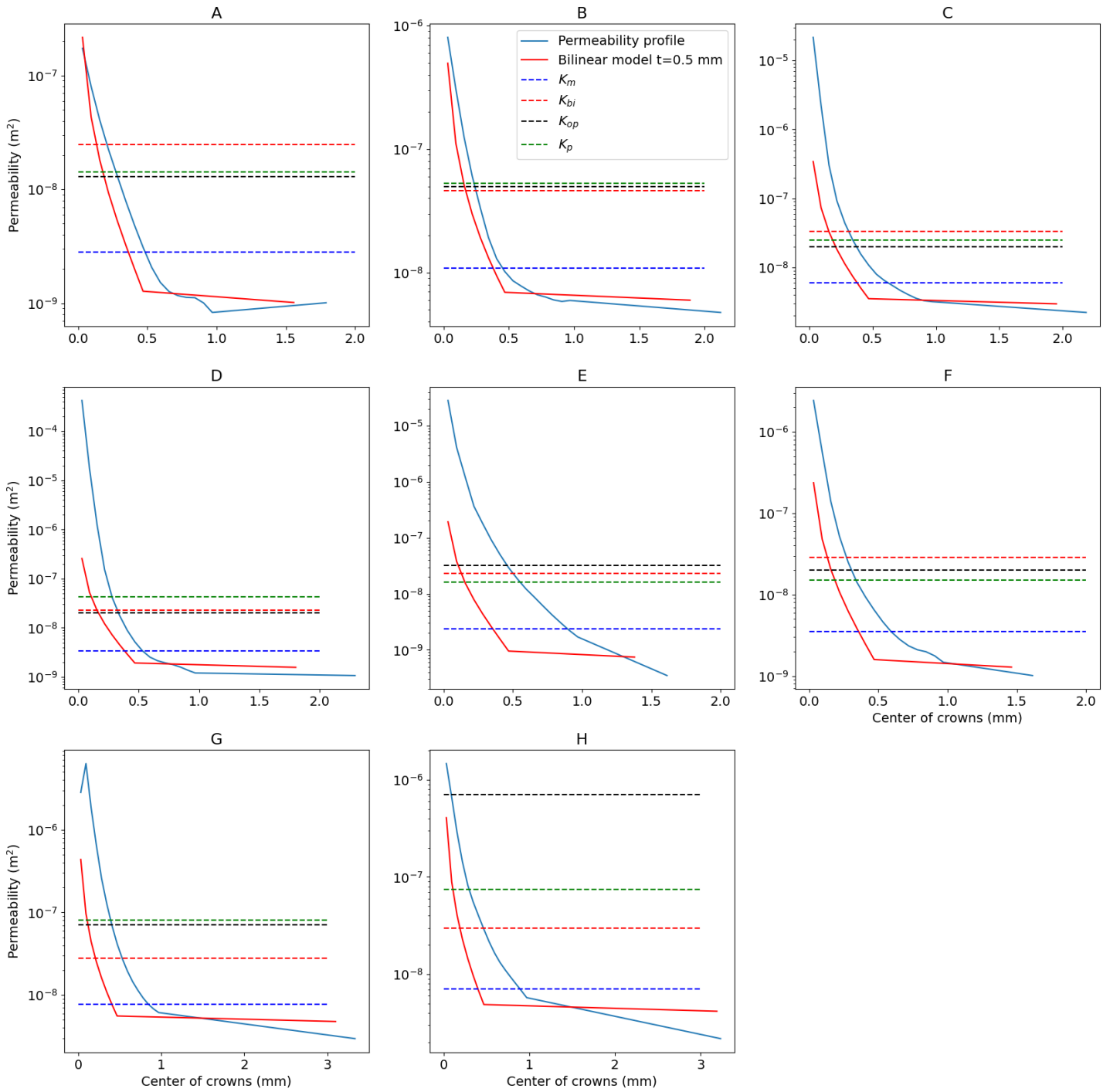


Figure 5.7: Permeability profile for each patient: crown and bilinear model. The equivalent permeability models are plotted in dotted line: mean ( $K_m$ ), optimal ( $K_{op}$ ), crowns ( $K_p$ ) and bilinear model ( $K_{bi}$ ).

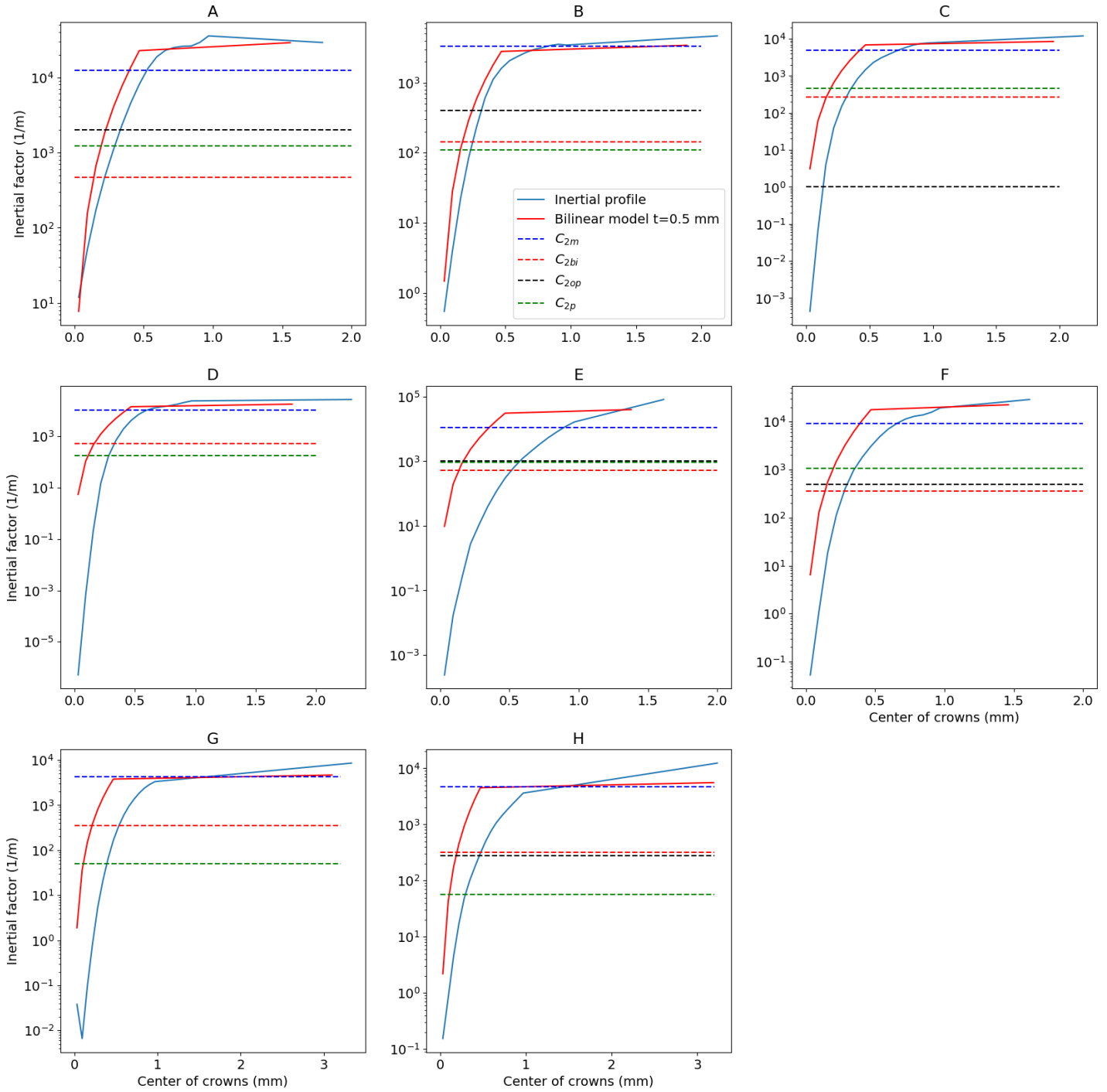


Figure 5.8: Inertial factor profile for each patient: crown and bilinear model. The equivalent inertial models are plotted in dotted line: mean ( $C_{2m}$ ), optimal ( $C_{2op}$ ), crowns ( $C_{2p}$ ) and bilinear model ( $C_{2bi}$ ).

to validate the porous models: the coil-resolved model. This model was developed in previous work [Barbour, 2018; Levitt *et al.*, 2016] at the University of Washington and consists of constructing a realistic numerical model of the coiled aneurysm with patient-specific boundary conditions.

For each patient, the geometry of the coil-resolved model was the 3D numerical model after coils positioning (see section 5.2.1). The hemodynamics analysis of the blood flow in the coiled aneurysm was done with finite volume fluid simulations using Fluent (ANSYS, Release 17.1; ANSYS, Canonsburg, Pennsylvania, USA). For each patient, the volume of the coiled aneurysm was meshed with a tetrahedral grid, and the element size of the mesh was  $200 \mu\text{m}$  for the parent vessel and  $20 - 40 \mu\text{m}$  at the surface of the coils [Levitt *et al.*, 2016]. The mesh was created with StarCCM+.

The blood was considered to be a Newtonian and incompressible fluid, with a viscosity of  $0.0035 \text{ Pa}\cdot\text{s}$  and a density of  $1050 \text{ kg}/\text{m}^3$ , consistent with previous studies in the literature [McGah *et al.*, 2011]. Patient-specific boundary conditions were defined at the inlet and outlet. During the endovascular coiling surgery, the surgeon used a dual-sensor Doppler guidewire (ComboWire and ComboMap; Volcano Corp, San Diego, California, USA) to measure blood velocities at several locations in the parent vessel. From those measurements, a pulsatile Womersley inlet profile was defined for each patient. In the outlet, a resistance-capacitance (RC) condition was applied for the patients having more than one outlet, and a zero-pressure condition outlet was applied for patients having only one outlet. The artery wall and the wall of the coil were considered rigid, with a non-slip boundary condition.

The Navier-Stokes equations were solved in the full anatomy of the patient (parent vessel and aneurysm):

$$\rho \left( \frac{\partial \mathbf{u}}{\partial t} + \mathbf{u} \nabla \mathbf{u} \right) = -\nabla p + \mu \nabla^2 \mathbf{u} \quad \text{and} \quad \nabla \cdot \mathbf{u} = 0 \quad (5.7)$$

Blood flow was simulated for 3 cardiac cycles, however, only the last cardiac cycle was kept for the analysis, to avoid transient effects after the simulation initialization during the first two cycles. The mean velocity in the aneurysm during the last cardiac cycle were analyzed for comparison with the results of the simulations of the porous models.

The coil-resolved model is an anatomical and physiologically accurate model that has been validated experimentally (see the Chapter 3), and could be used to establish parameters related to recanalization.

### 5.2.3.2 Porous models

The 3D numerical model for the porous simulation was constructed as for the coil-resolved model but without the coil geometries. The parent vessel was considered to be a fluid region and the aneurysm a porous region (section 5.2.2.1). The mesh of the

patient's anatomy was created with StarCCM+, with the same characteristics as for the coil-resolved model (section 5.2.3.1). The patient-specific boundary conditions and fluid characteristics used for the porous models were the same as in the coil-resolved model

The blood flow in the coiled aneurysms modeled as a porous medium can be described with the following Navier-Stokes-Brinkman equations, using the one domain approach for the porous and fluid domains:

$$-\rho \left( \frac{\partial \mathbf{u}}{\partial t} + \mathbf{u} \nabla \mathbf{u} \right) - \nabla p + \mu_e \nabla^2 \mathbf{u} = \frac{\mu}{K} \mathbf{u} + C_2 \frac{1}{2} \rho |\mathbf{u}| \mathbf{u} \quad \text{and} \quad \nabla \cdot \mathbf{u} = 0 \quad (5.8)$$

where  $\nabla p$  is the pressure gradient ( $Pa/m$ ),  $\mathbf{u}$  is the fluids velocity,  $K$  ( $m^2$ ) the permeability,  $C_2$  ( $1/m$ ) is the inertial factor and  $\mu_e$  is an effective viscosity given by  $\mu_e = \mu_r \mu$ , where  $\mu_r$  is the relative viscosity, which was taken as 1 (see Chapter 4), and  $\mu$  is the blood's viscosity. Equation (5.8) is solved in the whole domain: parent vessel and the porous media. In the parent vessel,  $C_2 = 0$  and  $K \rightarrow \infty$ , therefore this equation is equivalent to equation (5.7). In the porous media,  $K$  and  $C_2$  have finite values and (5.8) is equivalent to equation (5.1). In this later case  $\mathbf{u}$  is Darcy's velocity. Different porous models were studied and  $K$  and  $C_2$  varied accordingly. For each patient we simulated four homogeneous isotropic porous model cases:

- Case 1 - Optimal porous model -  $K_{op}$  and  $C_{2op}$ : This is the homogeneous isotropic porous model with the optimal values of permeability and inertial factor, respectively  $K_{op}$  and  $C_{2op}$ , to find the same mean velocities (error < 2%) over one cardiac cycle that in the coil-resolved model. The optimal values were defined empirically. The permeability  $K_{op}$  was established by running Stokes simulations, avoiding inertial effects. The inertial factor,  $C_{2op}$ , was established by running transient simulations with the same patient-specific boundary conditions as for the coil-resolved model, fixing the permeability at the  $K_{op}$  value found in the Stokes simulations, only varying  $C_2$ .
- Case 2 - Porous model based on the mean porosity -  $K_m$  and  $C_{2m}$ : This is the homogeneous isotropic porous model based on the mean porosity  $\phi_m$ . The permeability and inertial factor parameters,  $K_m$  and  $C_{2m}$ , defining the porous model were calculated with equation (5.3) and (5.4) respectively, where  $\phi = \phi_m$ . This model has been used for the majority of the studies in the literature when modeling the aneurysm as a porous media model [Levitt *et al.*, 2016; Mitsos *et al.*, 2008; Kakalis *et al.*, 2008]. However, this model is not representative of the blood flow in the aneurysm. Figure 5.7 and Figure 5.8 present the permeability and inertial profile, respectively, as well as the  $K_m$  and  $K_{op}$ , and the  $C_{2m}$  and  $C_{2op}$ , respectively.  $K_m$  and  $C_{2m}$  are very different

from the optimal values, which explains the difference from the coil-resolved model in CFD simulation in previous studies.

- Case 3 - Porous crown model -  $K_p$  and  $C_{2p}$ : This is the homogeneous isotropic porous crown model developed in section 5.2.2.2. In Figure 5.7 and Figure 5.8, both the optimal values and the porous crown model values are plotted for each patient. The crown model seems to be more accurate than the model based on the mean porosity, and the permeability seems to be close to the optimal model for most of the patients. Patient H porous crown model seems to be very far from the optimal model as  $K_{op} \gg K_p$ , therefore it might not be representative of the blood flow in the coiled aneurysm for this patient.
- Case 4 - Bilinear porous model -  $K_{bi}$  and  $C_{2bi}$ : This is the homogeneous isotropic bilinear model described in section 5.2.2.3. As for the previous models, the objective is for the permeability and inertial factor values of the bilinear porous model to match the ones obtained in the optimal porous model. As for the previous models, the permeability and inertial factor values are plotted in Figure 5.7 and 5.8, respectively. This model seems to be representing the optimal model as well as the porous crown models, for most of the patients. Patient H also presents the highest difference against the optimal model (factor 10).

The permeability and inertial factor values for the four porous models are summarized in table 5.3 and 5.4. The summary of the simulations run for each patient can be found in Table 5.5 and are noted  $S_{\alpha\alpha}$  for each model, where  $\alpha = op$  (case 1),  $m$  (case 2),  $p$  (case 3),  $bi$  (case 4).

Patient	$\phi_m$	$K_m$ (m <sup>2</sup> )	$K_{op}$ (m <sup>2</sup> )	$K_p$ (m <sup>2</sup> )	$K_{bi}$ (m <sup>2</sup> )
A	0.697	2.81 10 <sup>-9</sup>	1.30 10 <sup>-8</sup>	1.42 10 <sup>-8</sup>	2.46 10 <sup>-8</sup>
B	0.825	1.09 10 <sup>-8</sup>	5.00 10 <sup>-8</sup>	5.28 10 <sup>-8</sup>	4.63 10 <sup>-8</sup>
C	0.772	5.98 10 <sup>-9</sup>	2.00 10 <sup>-8</sup>	2.49 10 <sup>-8</sup>	3.30 10 <sup>-8</sup>
D	0.715	3.35 10 <sup>-9</sup>	2.00 10 <sup>-8</sup>	4.25 10 <sup>-8</sup>	2.28 10 <sup>-8</sup>
E	0.678	2.34 10 <sup>-9</sup>	3.25 10 <sup>-8</sup>	1.61 10 <sup>-8</sup>	2.34 10 <sup>-8</sup>
F	0.720	3.51 10 <sup>-9</sup>	2.00 10 <sup>-8</sup>	1.51 10 <sup>-8</sup>	2.85 10 <sup>-8</sup>
G	0.795	7.66 10 <sup>-9</sup>	7.10 10 <sup>-8</sup>	8.04 10 <sup>-8</sup>	2.82 10 <sup>-8</sup>
H	0.788	7.10 10 <sup>-9</sup>	7.00 10 <sup>-7</sup>	7.46 10 <sup>-8</sup>	3.00 10 <sup>-8</sup>

Table 5.3: Summary of the permeability values for patients for the porous medium models.

Patient	$\phi_m$	$C_{2m}$ (1/m)	$C_{2op}$ (1/m)	$C_{2p}$ (1/m)	$C_{2bi}$ (1/m)
A	0.697	$1.23 \cdot 10^4$	$2.00 \cdot 10^3$	$1.23 \cdot 10^3$	$4.71 \cdot 10^2$
B	0.825	$3.34 \cdot 10^3$	$4.00 \cdot 10^2$	$1.11 \cdot 10^2$	$1.41 \cdot 10^2$
C	0.772	$4.90 \cdot 10^3$	$1.00 \cdot 10^0$	$4.53 \cdot 10^2$	$2.69 \cdot 10^2$
D	0.715	$9.65 \cdot 10^3$	$0.00 \cdot 10^0$	$1.80 \cdot 10^2$	$5.32 \cdot 10^2$
E	0.678	$1.10 \cdot 10^4$	$1.00 \cdot 10^3$	$9.48 \cdot 10^2$	$5.20 \cdot 10^2$
F	0.720	$9.12 \cdot 10^3$	$5.00 \cdot 10^2$	$1.07 \cdot 10^3$	$3.59 \cdot 10^2$
G	0.795	$4.25 \cdot 10^3$	$0.00 \cdot 10^0$	$5.07 \cdot 10^1$	$3.50 \cdot 10^2$
H	0.788	$4.68 \cdot 10^3$	$2.80 \cdot 10^2$	$5.69 \cdot 10^1$	$3.15 \cdot 10^2$

Table 5.4: Summary of the inertial factor values for all the patients for the porous medium models.

Model	Simulation name	Porous model definition
Coil-resolved	S	
Porous media based on $\phi_m$	$S_{mm}$	$\phi_m, K_m, C_{2m}$
Optimal porous model	$S_{opop}$	$\phi_m, K_{op}, C_{2op}$
Porous crown model	$S_{pp}$	$\phi_m, K_p, C_{2p}$
Bilinear porous model	$S_{bibi}$	$\phi_m, K_{bi}, C_{2bi}$

Table 5.5: Summary of the simulations for all the patients

### 5.3 Results

The results of the numerical simulations can be found in Table 5.6. The table shows the mean velocity in the aneurysm over one cardiac cycle for the coil-resolved and the porous medium models for each patient. To compare the results, the percentage change for the mean velocities was calculated for each one of the porous models (see Table 5.6), where the coil-resolved model was considered as the gold standard. The differences are plotted in Figure 5.9. If we analyze each porous model, the results show that:

- Optimal porous model ( $S_{opop}$ ): The error varies between -2.3% and 0.4%. The mean velocity error is  $-0.9 \pm 1.3\%$ . This model was empirically defined to match the blood flow results of the reference model. One can note that, for patients C, D, and G, the values of  $C_{2op}$  are almost zero, i.e. inertial effects are negligible. This model can be used as a comparison with the other porous medium models, to study the ideal permeability and inertial values of the porous medium model.
- Porous model based on the mean porosity ( $S_{mm}$ ): The error varies between 46.4% and 88.7%. The mean velocity error for all patients is  $66.5 \pm 14.5\%$ . The model is inaccurate and systematically underestimates the blood velocities in the aneurysm. This is mainly linked to the permeability values  $K_m$  which

are much lower than the optimal permeability  $K_{op}$  and the  $C_{2m}$  coefficients which are overestimated. Indeed, the mean ratio  $K_m/K_{op}$  is  $0.2 \pm 0.1$  for all patients, and the mean ratio  $C_{2m}/C_{2op}$  is  $12.1 \pm 5.2$  for patients A, B, E, F, and H. For patients, C, D, and G, the inertial factor  $C_{2m}$  is much larger than  $C_{2op}$ , which is almost zero.

- Porous crown model ( $S_{pp}$ ): The error varies between -3.5% and 37.1%. The mean velocity error for all the patients is  $16.6 \pm 12.0\%$ . As expected the results of this model are better than the model based in the mean porosity since this model considers the heterogeneous distribution of the porosity within the porous media. The permeability and inertial factor approximation are very accurate for most patients. Indeed, the mean ratio  $K_p/K_{op}$  is  $1.0 \pm 0.6$  for all patients, and the mean ratio  $C_{2p}/C_{2op}$  is  $0.84 \pm 0.78$  for patients A, B, E, F and H. As for the mean porosity model, for patients C, D, and G, the inertial factor remains too high in comparison to  $C_{2op}$ .
- Bilinear porous model ( $S_{bibi}$ ): The error varies between 0.9% and 60.1%. The mean velocity error is  $26.0 \pm 20.1\%$ . The results for the bilinear model are consistent with the results of the porous crown model, despite the bilinear model's approximations (shape and volume of the aneurysm, and bilinear distribution of the porosity). The permeability and inertial factor approximation are very accurate for most patients. Indeed, the mean ratio  $K_{bi}/K_{op}$  is  $1.1 \pm 0.6$  for all patients, and the mean ratio  $C_{2bi}/C_{2op}$  is  $0.59 \pm 0.35$  for patients A, B, E, F, and H. As for the mean porosity model and the porous crown model, for patients C, D, and G the inertial factor is still overestimated.

The bilinear and the porous crown models seem to be adequate to simulate blood flow in coiled aneurysms accurately. The porous crown model is more accurate than the bilinear model, as expected due to the bilinear model multiple approximations. Different factors can be invoked to explain the deviation between these two porous models and the coil-resolved model:

First, the anatomy of the aneurysm and the positioning of the coils can be the origin of the deviation from the coil-resolved model. For example, the bilinear model is more accurate for Patient B, D, and E, with differences below 11%, and less so for patients A, C, F, and G, with errors reaching between 27 and 45% (see Table 5.6). These differences might be due to the location of the aneurysms: A, C, D, and F's developed in a bifurcation, which influences the blood flow (see Figure 5.1). Also, the anatomies of Patients C and G are very complex (long neck, big volume), which might impact the results. Patient H is an exception from all the other patients as the bilinear model is not at all suited for this patient (error of 60.1%). This is because there is a portion of the coils escaped into the parent vessel (see Figure 5.1). The neck

Pt	Simulation name	Mean velocity in the aneurysm (m/s)	% of change mean velocity in the aneurysm
A	S	$2.12 \cdot 10^{-2}$	
	$S_{mm}$	$8.82 \cdot 10^{-3}$	58.4
	$S_{opop}$	$2.11 \cdot 10^{-2}$	0.4
	$S_{pp}$	$2.32 \cdot 10^{-2}$	-9.3
	$S_{bibi}$	$3.08 \cdot 10^{-2}$	-45.3
B	S	$4.43 \cdot 10^{-2}$	
	$S_{mm}$	$2.37 \cdot 10^{-2}$	46.4
	$S_{opop}$	$4.41 \cdot 10^{-2}$	0.4
	$S_{pp}$	$5.24 \cdot 10^{-2}$	-18.3
	$S_{bibi}$	$4.90 \cdot 10^{-2}$	-10.7
C	S	$2.54 \cdot 10^{-3}$	
	$S_{mm}$	$1.21 \cdot 10^{-3}$	52.1
	$S_{opop}$	$2.57 \cdot 10^{-3}$	-1.4
	$S_{pp}$	$2.76 \cdot 10^{-3}$	-8.8
	$S_{bibi}$	$3.23 \cdot 10^{-3}$	-27.1
D	S	$6.83 \cdot 10^{-3}$	
	$S_{mm}$	$2.25 \cdot 10^{-3}$	67.1
	$S_{opop}$	$6.97 \cdot 10^{-3}$	-2.0
	$S_{pp}$	$9.36 \cdot 10^{-3}$	-37.1
	$S_{bibi}$	$6.77 \cdot 10^{-3}$	0.9
E	S	$3.34 \cdot 10^{-2}$	
	$S_{mm}$	$6.27 \cdot 10^{-3}$	81.2
	$S_{opop}$	$3.42 \cdot 10^{-2}$	-2.3
	$S_{pp}$	$2.69 \cdot 10^{-2}$	19.5
	$S_{bibi}$	$3.30 \cdot 10^{-2}$	-1.5
F	S	$1.33 \cdot 10^{-2}$	
	$S_{mm}$	$3.33 \cdot 10^{-3}$	74.9
	$S_{opop}$	$1.35 \cdot 10^{-2}$	-2.0
	$S_{pp}$	$1.04 \cdot 10^{-2}$	21.7
	$S_{bibi}$	$1.73 \cdot 10^{-2}$	-29.9
G	S	$8.25 \cdot 10^{-4}$	
	$S_{mm}$	$3.05 \cdot 10^{-4}$	63.1
	$S_{opop}$	$8.19 \cdot 10^{-4}$	0.7
	$S_{pp}$	$8.53 \cdot 10^{-4}$	-3.5
	$S_{bibi}$	$5.56 \cdot 10^{-4}$	32.6
H	S	$3.47 \cdot 10^{-2}$	
	$S_{mm}$	$3.92 \cdot 10^{-3}$	88.7
	$S_{opop}$	$3.40 \cdot 10^{-2}$	2.0
	$S_{pp}$	$2.73 \cdot 10^{-2}$	21.2
	$S_{bibi}$	$1.38 \cdot 10^{-2}$	60.1

Table 5.6: Summary at the results of the simulations for all patients: mean velocities in the aneurysm and percentage of change of the mean velocity.

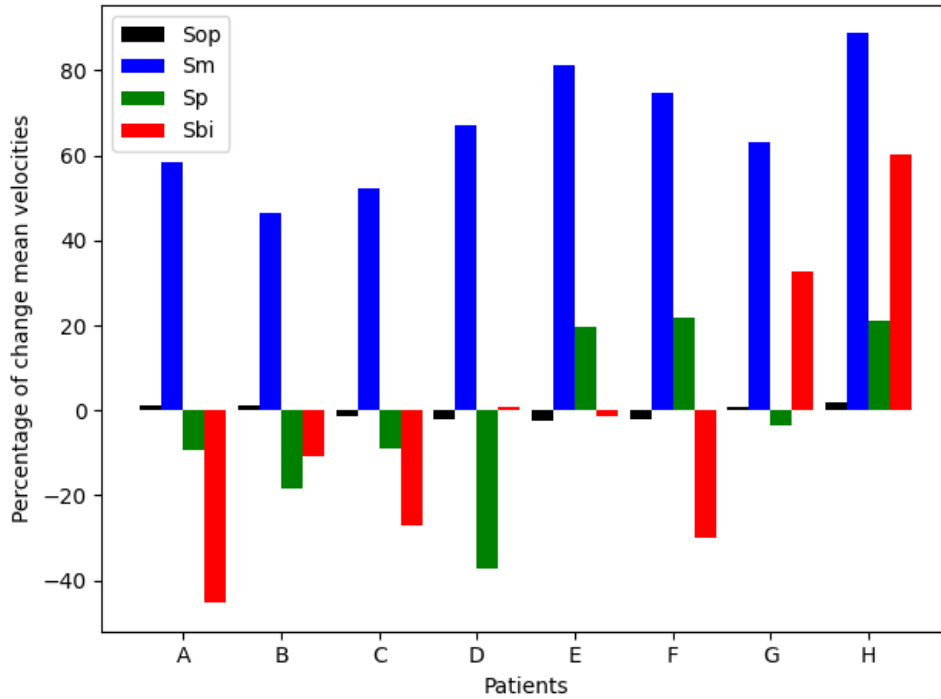


Figure 5.9: Percentage change for the mean velocities, the coil-resolved model is considered the gold standard. The error is defined as  $(\langle \mathbf{u}_{coil-resolved} \rangle - \langle \mathbf{u}_{porous} \rangle) / \langle \mathbf{u}_{coil-resolved} \rangle \times 100$ .

is defined as the envelope of the coils. This explains why, for this patient, the mean velocities in the aneurysm are very high even if this patient presents a very large aneurysm. Indeed, larger aneurysms tend to have low mean velocities (see Table 5.6). This shows that the model can only be applied for aneurysms where the coils didn't protrude into the parent vessel after being deployed inside the aneurysmal sac.

The other factor that might be responsible for the deviation between the porous crown model and the bilinear porous model away from the gold standard coil-resolved model is the hypothesis used to define the permeability and inertial factor. Indeed, the anatomy of the aneurysm has an impact on the blood flow on the blood flow was exposed previously. Therefore the hypothesis that the flow mainly moves along the crowns used to determined the permeability and inertial factor is not always verified. For this analysis, Patient H was excluded, as we considered it an outlier.

The permeability was calculated in these two porous models considering that the blood flow is predominantly tangential to the crowns inside the aneurysm (see section 5.2.2.2). Overall, this method to calculate the permeability seems accurate since the mean ratios  $K_p/K_{op}$  and  $K_{bi}/K_{op}$  are  $1.0 \pm 0.6$  and  $1.1 \pm 0.6$ , respectively. Figure 5.10 shows the comparison between the optimal permeability  $K_{op}$ , the permeability of the porous crown model  $K_p$ , and the permeability  $K_s$  calculated using equation (5.5), corresponding to the permeability value if the blood flow would have been

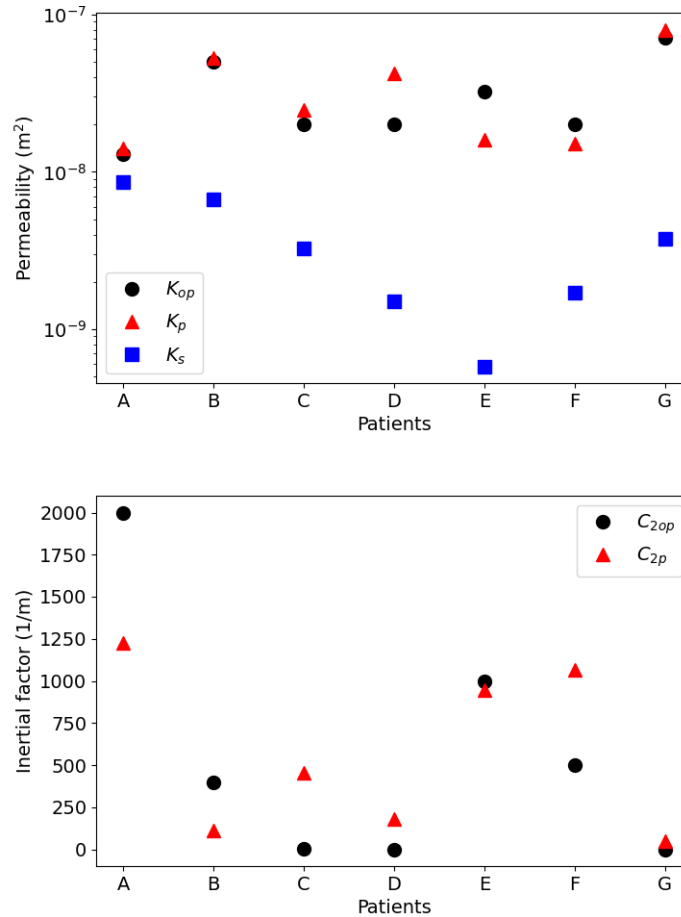


Figure 5.10: Permeability and inertial factor comparison between the optimal values and the parallel and perpendicular flow for patients A to G. Patient H was excluded for visibility of the results.

considered to be perpendicular to the crowns. The results of these comparisons show that  $K_p$  are closer to  $K_{op}$  than  $K_s$ . Therefore, the hypothesis of blood flow being tangential to the crowns is, in general, validated. However, for five out of the seven patients,  $K_s \ll K_{op} < K_p$ , which might imply that there is still a part of the flow that is perpendicular to the crowns. This could explain the error between the coil-resolved simulations and the porous crown model.

The definition of the inertial factor might also be at the origin of the deviation between the coil-resolved and the crown and bilinear porous models. Figure 5.10 shows the comparison between  $C_{2op}$  and  $C_{2p}$ . The differences are not consistent between patients: for only four out of the seven patients  $C_{2op} < C_{2p}$ . However, for the largest aneurysms, the inertial factor is systematically overestimated in the porous crown models (patients C, D, and G). Indeed, for these aneurysms, the mean velocities in the aneurysm are very slow ( $10^{-3}$  m/s) and, therefore, the inertial effects are negligible (see Table 5.4). In the porous crown model, for large aneurysms, we

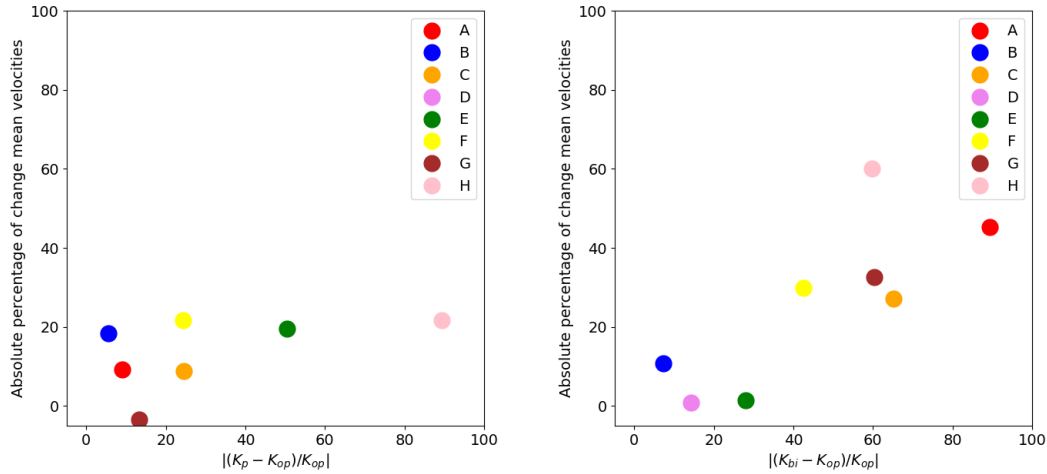


Figure 5.11: Percentage of error mean velocities versus difference between bilinear model and optimal model (right), and the porous crown model and optimal model (left), for the permeability values for patients A to H.

add "artificial" inertial effects which shouldn't exist due to the size of the aneurysm and the anatomy of the neck. Therefore, the inertial effects should be neglected for large aneurysms and small neck diameters.

In general, permeability seems to be the most important parameter impacting the accuracy of the porous model. Figure 5.11 presents the comparison of the error between the mean velocities and the difference between  $K_p$  and  $K_{op}$  (left) and between  $K_{bi}$  and  $K_{op}$  (right). If we analyze the porous crown model, the mean velocity error is consistent between patients. However, there is a small trend showing that the error of the mean velocities increases as the error of the permeability increases. For the bilinear model, the trend is more apparent. This confirms that permeability seems to be the dominant factor in the definition of the porous medium model for endovascular coils.

Finally, another purpose of modeling the coiled aneurysm as a porous medium is to significantly reduce computational cost of the simulations, bringing closer to clinically relevant times. Table 5.7 presents the computing time and the number of elements of the mesh for the coil-resolved simulations and the porous numerical models for each patient. The computational time for each patient was influenced by the mesh but also by the duration of the cardiac cycle, as it was different for each patient (patient-specific boundary conditions). The results show that the coil-resolved models need at least 195 hours to run one case (three cardiac cycles), which is between 8 days for the smaller cases and 25 days for the bigger cases on 1 core and 28 processors. The size of the flow field storage is also very high, needing large RAM memory available to run the cases. The porous medium models needs

less than 25h to run under the same conditions. Therefore, the porous models present an advantage in terms of computational time and resources needed. Also, running in only 25h, the porous models can be used to predict treatment outcomes in clinical practice for the patients in the neuro-suite, assuming access to the right computational resources.

Pt	Coil-resolved		Porous models	
	Mesh: Number of elements	Computational time (hours)	Mesh: Number of elements	Computational time (hours)
A	21807205	195	4389806	24
B	21545450	244	3173018	19
C	36307410	303	3863844	20
D	35173897	426	2782653	22
E	23815006	288	1419603	11
F	16474037	200	1718917	13
G	42370024	608	2876708	20
H	36058468	580	3678771	25

Table 5.7: Summary of the computing time for each patient and the mesh properties.

## 5.4 Discussion

This study presents a novel method to model intracranial aneurysms treated with coils as a porous medium: the bilinear porous model. It was validated on eight patients. This model is innovative as it doesn't require the geometry of the coils to establish the permeability and inertial factor while saving significant computational time in comparison with other existing anatomically and physiologically accurate models. This presents an innovation because the model can be created and solved in the neuro-suite, only based on the patient's anatomy, and the coils' specifications. Therefore, this could be used for simulations with patient-specific boundary conditions to predict the treatment outcomes in the future.

In previous studies, the porous models developed to simulate blood flow in intracranial aneurysms were homogeneous and isotropic, and the calculation of the permeability and the inertial factor was only based on the mean porosity in the aneurysmal sac volume [Levitt *et al.*, 2016; Kakalis *et al.*, 2008; Mitsos *et al.*, 2008], in which the Kozeny Carman model was used to calculate the permeability [Kakalis *et al.*, 2008]. In this work, the  $S_{mm}$  model was also analyzed, however, the permeability was calculated using a self-consistent estimate defined by Boutin [2000]. The results are consistent with the previous studies: the mean velocities in the aneurysm are systematically underestimated (the mean error is 66.5%). Indeed, the permeability is underestimated ( $K_m/K_{op} = 0.2 \pm 0.1$ ). These models are only based on the mean porosity of the aneurysm. Consequently, they are not able to

take into account the heterogeneous distribution of the porosity of the coils in the aneurysm, notably at distances close to the aneurysm wall relative to the size of the aneurysm, where the gradient of porosity is high (see Figure 5.6). The separation of scales in the porous medium is not truly guaranteed and the porous gradients are not negligible in the definition of the effective permeability [Auriault *et al.*, 2007]. Moreover, as this gradient of porosity is neglected, the mean velocities at the neck are underestimated. The blood velocities in the aneurysm are mainly defined by the blood velocities at the neck, which explains why the mean velocities in this model are underestimated.

The model chosen to calculate the permeability also impacts the accuracy of the results. Patient A was analyzed in *Levitt et al.* [2016] and an error of 90% between the porous model and the coil-resolved model was found, when comparing the flow rate through the neck. Here, for the same patient, the error of the mean velocities in the aneurysm was 58.4%. Therefore, the self-consistent estimate [Boutin, 2000] used to calculate the permeability value in the model  $S_{mm}$  seems more accurate than the Kozeny Carman model to simulate blood flow in a coiled aneurysm. Nevertheless, in this model the error is still significant and cannot be considered practical to predict hemodynamics and thrombus formation in coiled aneurysms. The heterogeneity of the coils needs to be included in the definition of the permeability and inertial factor.

In this study, two models were proposed that consider the heterogeneous distribution of the porosity in the aneurysm filled with coils: the porous crown model and the bilinear. The permeability and the inertial factor of those models are more accurate than the ones calculated based on the mean porosity ( $S_{mm}$ ). Indeed, the mean permeability ratios  $K_p/K_{op}$  and  $K_{bi}/K_{op}$  are 1 and 1.1 respectively, and the mean inertial factor ratios are  $C_{2p}/C_{2op}$  and  $C_{2bi}/C_{2op}$  are 0.84 and 0.59 respectively. The porous model based on the mean porosity presented ratios of 0.2 and 12.1 for the permeability and inertial factor respectively. Therefore these models considering the heterogeneity of coils present an important advance in the accuracy of the porous modeling. These two models can be analyzed independently.

First, the porous crown model is a homogeneous isotropic porous media where the permeability and inertial factor are defined by considering that the flow mainly moves along the crown in the aneurysm (see section 5.2.2.2). This model has proven to be very accurate as the mean error is around 16.6%, instead of 66% for the model based on the mean porosity. This is the first homogeneous isotropic porous model available in the literature that considers the heterogeneous distribution of the porosity. This model presents one main disadvantage: it cannot be used for prediction. Indeed the process to define the permeability and inertial factor are very complex, as it

requires the coils geometry and numerous steps (image treatment, definition of the crowns, porosity profile). However, with the hypothesis of the porous crown models, we could define another porous model that can be used for prediction: the bilinear porous model.

The bilinear model is also a homogeneous isotropic porous model that considers the heterogeneous distribution of the porosity in the aneurysm. This model uses the same hypothesis as in the porous crown model: that blood flow moves mainly tangential to the crowns. However, in this model, the geometry of the coils isn't required. Only the mean target porosity defined by the surgeon, the aneurysm anatomy (volume, neck area, depth, etc), and the bilinear approximation of the porosity profile are used. The simulation results show that the bilinear model is as accurate as the porous crown model, when compared to the coil-resolved model as a gold standard. The hypothesis that the flow is predominantly tangential to the crowns, considered in the bilinear porous model, was validated with the porous crown model. However, we also validated the target porosity, the ellipsoidal shape approximation for the aneurysm, and the bilinear approximation of the porosity profile.

- The mean porosity calculated from the 3D images of the coils for each case was considered as the target porosity defined in the bilinear model. If the model was to be used in the neuro-suite, the mean porosity should be the target porosity chosen by the surgeon. However, this shouldn't affect the results obtained since the mean porosity values calculated are similar to the target value chosen by the surgeon (between 0.7 and 0.8).
- The other main hypothesis considered was that the aneurysm volume could be approximated accurately by an ellipsoid. This was validated by comparing the volume of the aneurysm with the ellipsoidal volume. Figure 5.5 shows that the ellipsoidal approximation is very accurate. This validates the hypothesis invoked in formulating the bilinear model and applying it to clinical predictions in the neuro-suite.
- The bilinear approximation of the porosity seems to be accurate for these eight patients. Indeed, the ratio of permeabilities  $K_{bi}/K_{op} = 1.1 \pm 0.6$  is very low, and the mean velocity error is around 26%. However, this is the simplest model to approximate the porosity profile measured on the eight patients. More complex mathematical models can be used in the future to reproduce the porosity profile and improve the results of the porous model. Also, the parameter  $t$ , defined as the region where the porosity decreases linearly, was set at 0.5 mm. This value was established with only three iterations ( $t= 1\text{mm}$ ,

$t=0.75$  mm and  $t=0.5$ mm). The bilinear approximation of the porosity profile could also be improved by increasing the sample of  $t$  values.

Overall, the bilinear model developed here is the first proposed to simulate hemodynamics in coiled intracranial aneurysms that can be used for the prediction of treatment outcomes. It has shown very good results when compared with the coil-resolved simulations. However, this model can be improved in future studies by introducing more layers to capture the complexity of the coil mass deployed inside the intracranial aneurysm and its effects on the hemodynamics.

First, in the calculation of the permeability, the flow was considered to be only moving tangential to the crowns. In reality, the blood flow also has a component perpendicular to the crowns. Including this aspect in the calculation of permeability would improve its accuracy. The definition of permeability is crucial as it is the main parameter that dominates blood flow in coiled aneurysms as it is shown on Figure 5.11.

Second, even if the inertia factor seems to have a minor effect in comparison to the permeability in the blood flow, its estimation can be improve. Indeed, as shown in this study, for large aneurysm volumes, especially the ones with narrow necks where the blood flow is very slow, inertial effects are negligible. In the bilinear model, the inertial effects tend to be overestimated for those cases. Therefore, anatomical considerations could be included to improve the inertial factor.

Finally, the bilinear model can only be applied for aneurysms treated with coils where the coils stay inside the aneurysmal sac, and don't protrude into the parent vessel. Patient H is the canonical example for this case, as it shows very different results from the other patients. This patient was excluded from the general analysis. This also reiterates the previous discussion: there should be some anatomical considerations when defining the aneurysmal model. Indeed, in the bilinear model, the aneurysmal volume was defined as the coil envelope. However in the neuro-suite, the coils haven't been placed and a different definition of the aneurysm volume and porous model is needed. We expect that the coil envelope corresponds to the narrow side of the neck and that this can be used to define the edge of the aneurysm. However, this hypothesis needs validation in the future.

Overall this study presents promising results on modeling blood flow in intracranial aneurysms treated with endovascular coils as a porous medium. The novel porous medium model proposed can be used for clinical prediction and it was validated for eight patients. This numerical model can be constructed using only the CT scans of the anatomy of the patients obtained clinically, which opens a door to study the

hemodynamics parameters related to treatment success in a large cohort of patients, and while saving significant computational time.

## 5.5 Conclusion

In this study, the cerebral aneurysm treated with coils was modeled as a homogeneous isotropic porous medium model. The permeability and the inertial factor of the bilinear model are defined by considering the heterogeneous distribution of the coils and the complexity of the aneurysmal shape. The porous model was validated by comparing it with the coil-resolved model using patient-specific boundary conditions. This model seems to be accurate to model blood flow in intracranial aneurysms treated with coils. This opens a door to study hemodynamics in a large cohort of patients, and to establish the hemodynamics parameters related to treatment outcomes.

---

## Conclusion and perspectives

As we discussed in the state of art part (Chapter 2), there is a risk of recanalization after treating the cerebral aneurysm with coils, and studying hemodynamics in the treated aneurysms could prevent it. Up to date, the existing models that are anatomically and physiologically accurate need the geometry of the coils to study the hemodynamics and can't be used for treatment outcome prediction. For this reason, porous models have been developed to predict blood flow in cerebral aneurysms treated with endovascular coils. However, the porous models developed up to date do not capture the physiology, i.e. are too simple to reproduce the flow within coiled aneurysms with accuracy. Therefore the objectives of the present work were:

- To validate experimentally the numerical model used as a gold standard, i.e. the coil-resolved model that uses the exact geometry of the coils, placed in the patient-specific anatomy of the vessel and aneurysm, and with patient-specific boundary conditions, to develop and validate porous models.
- To define the porous medium (the coil mass in the aneurysmal sac), and to characterize its porosity distribution.
- To improve the definition of the parameters (permeability and inertial factor) involved in porous models by taking into account the heterogeneous distribution of the porosity within coiled aneurysms.
- To propose a porous model based on basic information available in the neuro-suite (CT scan of the aneurysm, target porosity defined by the surgeon), which is able to predict the flow through the coiled aneurysm before the treatment.
- To validate these models on a cohort of patients.

In the following section, the main results obtained in this study are recalled and short-term and long-term future work is presented.

## 6.1 Main results

The main results of this study are:

- **Experimental and numerical analysis of residence time in coiled aneurysms:** In order to validate coil-resolved simulations, an original experimental set-up has been developed to measure the residence time of rhodamine within coiled aneurysms using planar laser-induced fluorescence. These experiments, performed on six patient models, confirmed that residence time is impacted first by the anatomy of the patient: it is higher for larger aneurysms. The evolution of rhodamine concentration over time is consistent between patients: an important part (depending on the size of the aneurysm) of the rhodamine is cleared out in the first cycle and then slowly decreased until a complete washout. In parallel to these experiments, the six coil-resolved models have been constructed using the methodology developed by *Barbour* [2018] and the residence time has been studied by performing passive scalar transport simulations. Overall, the coil-resolved model reproduces the experimental results, with small differences due to image artifacts or some hypothesis taken in the numerical model. Therefore, the coil-resolved model can be considered as anatomically and physiologically accurate and can be used to validate the porous models (Chapter 3).
- **Determination of the porosity distribution:** The porosity distribution within the coiled aneurysm has been determined from 3D synchrotron x-ray tomography images. This distribution has been analyzed radially using crowns and by discretizing the coil mass with cubes. The results obtained by both methods show that the porosity is highly heterogeneous. In particular, when analyzing the porosity distribution radially, we found that there is a pattern for all the patients: the porosity is very high near the wall and homogeneous in the bulk. This heterogeneous zone with strong porosity gradient represents an important part of the aneurysm volume, therefore it has an impact on the blood flow. Considering the heterogeneous distribution in the calculations of the permeability and inertial factor could improve the accuracy of porous model for coiled aneurysms (Chapter 4).
- **Impact of porosity on the permeability and inertial factor definition:** The permeability and inertial factor of the coils itself have been computed from the 3D images by solving specific boundary problems arising from homogenization. The obtained results have shown that (i) the anisotropy of the permeability and the inertial factor are negligible, to first approximation, in comparison to their variation due to the porosity heterogeneity and (ii)

the evolution of the permeability with the porosity is well described by the self-consistent estimate developed by *Boutin* [2000]. Concerning the inertial factor, a curvefit from the numerical results has been proposed.

- **Porous models developed to model blood flow in aneurysm with coils:** The porous models that exist in the literature for modeling blood flow in coiled aneurysms were only based on the mean porosity. Our results show that those models systematically underestimate the mean velocities in the aneurysm. Two models were developed in this project for modeling the aneurysm with coils as a porous medium including the heterogeneous distribution of the porosity within coiled aneurysms.
  - **Porous crown model:** The blood flow in the aneurysm with coils is modeled as a homogeneous isotropic porous medium where the permeability and the inertial factor are calculated by considering that the blood flow mainly moves tangential to the crowns (parallel flow). This model was validated for eight patients and has proven to be the most accurate homogeneous isotropic porous model available in the literature up to date. Indeed, when comparing the mean velocities from this porous model with the ones from the coil-resolved, the mean velocity error is  $16.6 \pm 12\%$ , whereas the error is  $66.5 \pm 14.5\%$  in the standard model based on the mean porosity. This model, however, cannot be used for prediction as it requires the geometry of the coils to calculate its parameters (porosity profile, permeability and inertial factor). (Chapter 4 and Chapter 5).
  - **Bilinear porous model:** We defined a homogeneous isotropic porous model for the aneurysm with coils where the permeability and inertial factor can be defined by knowing only the anatomy of the patient's aneurysm and parent vessel, the packing density targeted by the surgeon, and doing a bilinear approximation of the porosity profile of the aneurysm with coils. These two pieces of information can be found in the neuro-suite, which makes this model potentially able of prediction of treatment outcome. This model was validated for eight patients and the results are very promising, as the mean velocity error is 26%. This model also presents significant savings in terms of computational time, as well as of the construction of the model. Figure 6.1 presents the process to obtain the coil-resolved model and the process to obtain the bilinear porous model, showing that the number of steps is significantly lower for the porous model. Overall this model can be used in the future for the prediction of the treatment outcomes (Chapter 5).

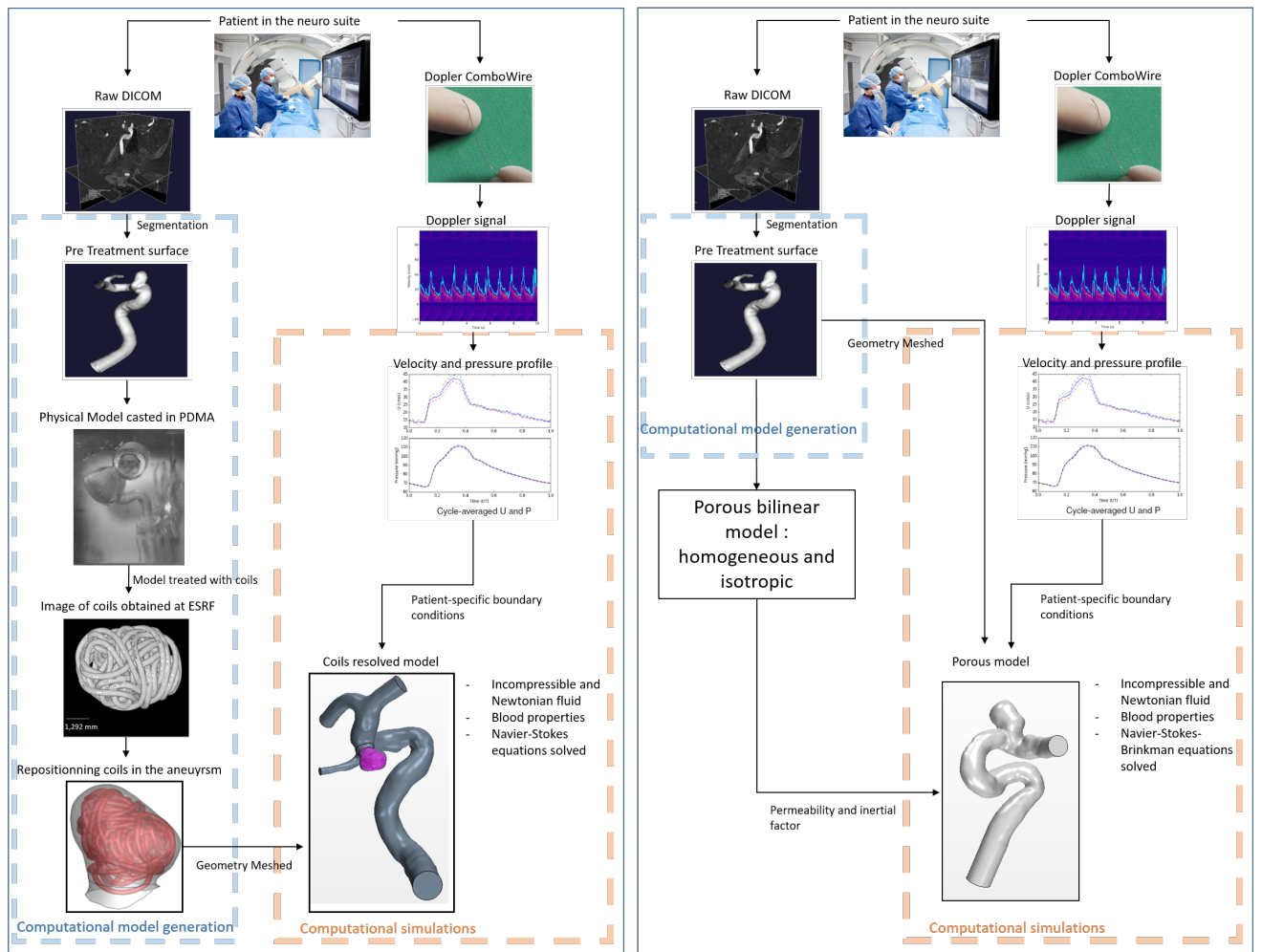


Figure 6.1: Comparison between the process to create the coil-resolved model and the bilinear porous model. On the left, the full process of the coil-resolved model: from the data acquisition to the computational model generation and finally the computational simulation. In the right, the full process to the bilinear porous model.

## 6.2 Perspectives

The results of this work open questions and other topics of research short term and long term:

- **Improving the bilinear model:** Even if the results obtained with this model are promising, the differences with the coil-resolved model are still significant in some of the cases. This model can probably be improved by (i) by including some anatomical considerations (such as the size of the aneurysm and the dimensions of the neck) in the estimation of the inertial factor, (ii) by taking into account the effect of the flow perpendicular to the crowns in the definition of the permeability or (iii) by considering more realistic porosity profile that a simple bilinear representation.

- **Study the repeatability:** The porous model has been validated for real aneurysm anatomy with coils deployed inside, however, there is a need to study the repeatability of the treatment on the determination of the permeability and inertial factor for the same model. This study is fairly simple as it requires one model to be treated several times by the same surgeon. In this study, all the models were treated by the same surgeon, studying repeatability in between surgeons would be of interest too.
- **Establishing hemodynamics factors related with recanalization:** This work opens an opportunity to study, once the bilinear model is completely defined, hemodynamics parameters related with thrombosis inside the aneurysmal sac. Since the bilinear model only requires the anatomy of the patient and the target packing density, this could be applied to a large cohort of patients, using either recruited patients or the open-access data available.
- **Related to other treatments:** This porous medium study has only been used in cerebral aneurysms treated with coils, however, there are other types of treatments. For example, stent-assisted coiling technique, that also require porous models to describe blood flow in the aneurysmal sac. Combining the bilinear porous model with other porous models developed for the stent for example would be useful for, not only predict the outcome of the treatment with coils, but also with stents and coils or other devices.
- **Patient-specific treatment prediction:** Overall, this study is a step towards personalized treatment design and prediction of outcomes for each patient, avoiding recanalization. Indeed, the bilinear porous model allows simulation of blood flow in the aneurysm by using only parameters available in the neuro-suite. This opens a door to develop a methodology in the future to use the porous model to design the treatment for each patient just before the procedure.



---

## Bibliography

- Abdihalim, M., M. Watanabe, and S. C. B. J. M. S. A. Qureshi, Are coil compaction and aneurysmal growth two distinct etiologies leading to recurrence following endovascular treatment of intracranial aneurysm?, *J Neuroimaging*, *24*(2), 171–5, 2014.
- Achenbach, E., Influence of surface roughness on the cross-flow around a circular cylinder, *Journal of Fluid Mechanics*, *46*, 321–35, 1971.
- Alastruey, J., K. Parker, J. Peiró, S. Byrd, and S. Sherwin, Modelling the circle of Willis to assess the effects of anatomical variations and occlusions on cerebral flows, *J Biomech*, *40*(8), 1794–805, 2007.
- Augsburger, L., P. Reymond, D. A. Rufenacht, and N. Stergiopoulos, Intracranial Stents Being Modeled as a Porous Medium: Flow Simulation in Stented Cerebral Aneurysms, *Annals of Biomedical Engineering*, *39*, 850—863, 2011.
- Auriault, J., Heterogeneous medium. is an equivalent macroscopic description possible?, *International Journal of Engineering Science*, *29*(7), 785–795, 1991.
- Auriault, J., C. Geindreau, and L. Orgéas, Upscaling forchheimer law, *Transport in Porous Media*, *70*, 213–29, 2007.
- Auriault, J., C. Boutin, and C. Geindreau, *Homogenization of Coupled Phenomena in Heterogenous Media*, 2009.
- Babiker, M., B. Chong, L. F. Gonzalez, S. Cheema, and D. H. Frakes, Finite element modeling of embolic coil deployment: Multifactor characterization of treatment effects on cerebral aneurysm hemodynamics, *Journal of Biomechanics*, *46*(16), 2809–2816, 2013.
- Barbour, M., *Computational and Experimental Investigation into the Hemodynamics of Endovascularly Treated Cerebral Aneurysms*, 2018.

- Barbour, M., K. Gow, and A. Aliseda, Dominated Heparin Leakage From Multiple Catheter Designs: An In Vitro Experimental Study, *ASAIO J.*, *64*(5), 94–104, 2015a.
- Barbour, M., P. McGah, C. Ng, A. Clark, K. Gow, and A. Aliseda, Convective Leakage Makes Heparin Locking of Central Venous Catheters Ineffective Within Seconds: Experimental Measurements in a Model Superior Vena Cava, *ASAIO J.*, *61*(6), 701–9, 2015b.
- Beavers, G. S., and D. D. Joseph, Boundary conditions at a naturally permeable wall, *J. Fluid Mech.*, *30*, 197–207, 1967.
- Bederson, J., et al., Guidelines for the management of aneurysmal subarachnoid hemorrhage: a statement for healthcare professionals from a special writing group of the Stroke Council, American Heart Association, *Stroke*, *40*(3), 994–1025, 2009.
- Boutin, C., Study of permeability by periodic and self-consistent homogenisation, *European Journal of Mechanics - A/Solids*, *19*(4), 603–632, 2000.
- Boutin, C., and C. Geindreau, Periodic homogenization and consistent estimates of transport parameters through sphere and polyhedron packings in the whole porosity range, *Phys. Rev. E*, *82*, 036,313, 2010.
- Brinkman, H. C., A calculation of the viscous force exerted by a flowing fluid on a dense swarm of particles, *Appl. Sci. Res.*, *1*, 27–34, 1947.
- Brisman, J., J. Song, and D. Newell, Cerebral aneurysms, *N Engl J Med*, *355*(9), 928–39, 2006.
- Castro, M. A., M. C. A. Olivares, C. M. Putman, and J. R. Cebal, Unsteady wall shear stress analysis from image-based computational fluid dynamic aneurysm models under Newtonian and Casson rheological models, *Medical and Biological Engineering and Computing*, *52*(10), 827–39, 2014.
- Chalouhi, N., M. Ali, P. Jabbour, S. Tjoumakaris, L. Gonzalez, R. Rosenwasser, W. Koch, and A. Dumont, Biology of intracranial aneurysms: role of inflammation, *J Cereb Blood Flow Metab*, *32*(9), 1659–76, 2012.
- Chandesris, M., and D. Jamet, Boundary conditions at a fluid–porous interface: An a priori estimation of the stress jump coefficients, *International Journal of Heat and Mass Transfer*, *49*(14), 2137–2150, 2006.
- Chandesris, M., and D. Jamet, Jump conditions and surface-excess quantities at a fluid/porous interface: A multi-scale approach, *Transp Porous Med*, *78*, 419–438, 2009.

- Chiu, Y., B. Drolet, M. Seefeldt, and al, *Abnormalities of the Head and Neck arteries (Cerebrovascular Abnormalities)*, 2019.
- Chivukula, V., et al., Reconstructing patient-specific cerebral aneurysm vasculature for in vitro investigations and treatment efficacy assessments., *J Clin Neurosci.*, *61*, 153–159, 2019.
- Chueh, J.-Y., S. Vedantham, A. K. Wakhloo, S. L. Carniato, A. S. Puri, C. Bzura, S. Coffin, A. A. Bogdanov, and M. J. Gounis., Aneurysm permeability following coilembolization: packing density and coil distribution, *Journal of NeuroInterventional Surgery*, *7*(9), 676–681, 2015.
- Crobeddu, E., G. Lanzino, D. Kallmes, and H. Cloft, Review of 2 decades of aneurysm-recurrence literature, part 1: reducing recurrence after endovascular coiling, *AJNR Am J Neuroradiol*, *34*(2), 266–70, 2013.
- C.Sadasivan, E. Swartwout, A. Kappel, H. Woo, D. Fiorella, and B. Lieber, In vitro measurement of the permeability of endovascular coils deployed in cerebral aneurysms, *J Neurointerv Surg*, *10*(9), 896–900, 2018.
- Damiano, R. J., D. Ma, J. Xiang, A. H.Siddiqui, K. V. Snyder, and H. Meng, Finite element modeling of endovascular coiling and flow diversion enables hemodynamic prediction of complex treatment strategies for intracranial aneurysm, *Journal of Biomechanics*, *48*(12), 3332–3340, 2015.
- Darcy, H., *Les Fontaines Publiques de la Ville de Dijon*, 1856.
- D'Souza, S., Aneurysmal Subarachnoid Hemorrhage, *J Neurosurg Anesthesiol.*, *27*(3), 222–40, 2015.
- Ergun, S., Fluid Flow Through Packed Column, *Chem. Eng*, *48*, 89–94, 1952.
- Etminan, N., and G. Rinkel, Unruptured intracranial aneurysms: development, rupture and preventive management, *Nat Rev Neurol*, *12*(12), 699–713, 2016.
- Fisher, C., and J. S. Rossmann, Effect of Non-Newtonian Behavior on Hemodynamics of Cerebral Aneurysms, *Journal of biomechanical engineering*, *131*(9), 091,004, 2009.
- Forchheimer, P., Wasserbewegung Durch Boden, *Ver. Deutsh Ing*, *45*, 125–7, 1901.
- Ford, M., N. Alperin, S. Lee, D. Holdsworth, and D. Steinman, Characterization of volumetric flow rate waveforms in the normal internal carotid and vertebral arteries, *Physiol Meas*, *26*(4), 477–88, 2005.

- Foutrakis, G., H. Yonas, and R. Sciabassi, Saccular aneurysm formation in curved and bifurcating arteries, *AJNR Am J Neuroradiol*, 20(7), 1309–17, 1999.
- Gambaruto, A. M., J. Janela, A. Moura, and A. Sequeira, Sensitivity of hemodynamics in a patient specific cerebral aneurysm to vascular geometry and blood rheology, *Mathematical biosciences and engineering : MBE*, 8(2), 2011.
- Goyeau, B., D. Lhuillier, D. Gobin, and M. Velarde, Momentum transport at a fluid-porous interface, *Int. J. Heat Mass Transfer*, 49, 4071–81, 2003.
- Grunwald, I., P. Papanagiotou, T. Struffert, M. Politi, C. Krick, G. Gül, and W. Reith, Recanalization after endovascular treatment of intracerebral aneurysms, *Neuroradiology*, 49(1), 41–7, 2007.
- Guglielmi, G., F. Viñuela, J. Dion, and G. Duckwiler, Electrothrombosis of saccular aneurysms via endovascular approach, *Journal of Neurosurgery*, 75, 1–7, 1991.
- Hahn, C., and MA.Schwartz, Mechanotransduction in vascular physiology and atherogenesis, *Nat Rev Mol Cell Biol*, 10(1), 53–62, 2009.
- Hassanizadeh, S., and W. Gray, Boundary and interface conditions in porous media, *Water Resources Research*, 25(7), 1705–1715, 1989.
- Jeon, J., Y. Cho, J. Rhim, D. Y. H. Kang, J. Kim, W. Cho, and M. Han, Extended monitoring of coiled aneurysms completely occluded at 6-month follow-up: late recanalization rate and related risk factors, *Eur Radiol*, 26(10), 3319–26, 2016.
- Johnston, S., S. S. S, and D. Gress, The burden, trends, and demographics of mortality from subarachnoid hemorrhage, *Neurology*, 50(5), 1413–8, 1998.
- Kakalis, N. M. P., A. P. Mitsos, J. V. Byrne, and Y. Ventikos, The haemodynamics of endovascular aneurysm treatment: A computational modelling approach for estimating the influence of multiple coil deployment, *IEEE Transactions on Medical Imaging*, 27(6), 814–824, 2008.
- Karmonik, C., C. Yen, R. G. Grossman, R. Klucznik, and G. Benndorf, Intra-aneurysmal flow patterns and wall shear stresses calculated with computational flow dynamics in an anterior communicating artery aneurysm depend on knowledge of patient-specific inflow rates, *Acta Neurochirurgica*, 151, 479–485, 2009.
- Khan, M., K. Valen-Sendstad, and D. Steinman, Narrowing the Expertise Gap for Predicting Intracranial Aneurysm Hemodynamics: Impact of Solver Numerics versus Mesh and Time-Step Resolution, *AJNR Am J Neuroradiol*, 36(7), 1310–6, 2015.

- Lasseux, D., A. A. Arani, and A. Ahmadi-Senichault, On the stationary macroscopic inertial effects for one phase flow in ordered and disordered porous media, *Physics of Fluids, American Institute of Physics*, 23(7), 1–19, 2011.
- Levitt, M., P. McGah, A. Aliseda, P. Mourad, J. Nerva, S. Vaidya, R. Morton, B. Ghodke, and L. Kim, Cerebral aneurysms treated with flow-diverting stents: computational models with intravascular blood flow measurements, *AJNR. American journal of neuroradiology*, 35(1), 143–148, 2014.
- Levitt, M. R., S. S. Vaidya, J. C. Mai, D. K. Hallam, L. J. Kim, and B. V. Ghodke, Balloon Test Occlusion with the Doppler Velocity Guidewire, *Journal of Stroke and Cerebrovascular Diseases*, 21(8), 909.e1–909.e4, 2012.
- Levitt, M. R., et al., Computational fluid dynamics of cerebral aneurysm coiling using high-resolution and high-energy synchrotron X-ray microtomography: comparison with the homogeneous porous medium approach, *Journal of NeuroInterventional Surgery*, 0, 1–6, 2016.
- Li, C., S. Wang, J. Chen, H. Yu, Y. Zhang, F. Jiang, S. Mu, H. Li, and X. Yang, Influence of hemodynamics on recanalization of totally occluded intracranial aneurysms: a patient-specific computational fluid dynamic simulation study, *J Neurosurg*, 117(2), 276–83, 2012.
- Luo, B., X. Yang, S. Wang, and al, High shear stress and flow velocity in partially occluded aneurysms prone to recanalization., *Stroke*, 42, 745–753, 2011.
- McGah, P., D. Leotta, K. Beach, J. Riley, and A. Aliseda, A longitudinal study of remodeling in a revised peripheral artery bypass graft using 3D ultrasound imaging and computational hemodynamics, *Journal of biomechanical engineering*, 133(4), 041,008, 2011.
- McGah, P. M., et al., Accuracy of computational cerebral aneurysm hemodynamics using patient-specific endovascular measurements, *Annals of Biomedical Engineering*, 42, 503–514, 2014.
- Mei, C., and J. L. Auriault, The Effect of Inertia on Flow Through Porous Medium, *J. Fluid. Mech*, 222, 647–63, 1991.
- Meng, H., Z. Wang, Y. Hoi, L. Gao, E. Metaxa, D. Swartz, and J. Kolega, Complex hemodynamics at the apex of an arterial bifurcation induces vascular remodeling resembling cerebral aneurysm initiation, *Stroke*, 38(6), 1924–31, 2007.
- Meng, H., V. Tutino, J. Xiang, and A. Siddiqui, High WSS or low WSS? Complex interactions of hemodynamics with intracranial aneurysm initiation, growth, and

- rupture: toward a unifying hypothesis, *AJNR Am J Neuroradiol*, *35*(7), 1254–62, 2014.
- Metaxa, E., et al., Characterization of critical hemodynamics contributing to aneurysmal remodeling at the basilar terminus in a rabbit model, *Stroke*, *41*(8), 1774–82, 2010.
- Milner, J., J. Moore, B. Rutt, and D. Steinman, Hemodynamics of human carotid artery bifurcations: computational studies with models reconstructed from magnetic resonance imaging of normal subjects, *J Vasc Surg*, *28*(1), 143–56, 1998.
- Mitsos, A., N. Kakalis, Y. Ventiko, and J. Byrne, Haemodynamic simulation of aneurysm coiling in an anatomically accurate computational fluid dynamics model: technical note, *Neuroradiology*, *50*(4), 341–347, 2008.
- Morales, H., I. Larrabide, A. Geers, L. S. Roman, J. Blasco, J. Macho, and A. Frangi, A virtual coiling technique for image-based aneurysm models by dynamic path planning, *IEEE Transactions on Medical Imaging*, *32*(1), 119–129, 2013.
- Muschenborn, A., J. Ortega, J. Szafron, D. Szafron, and D. Maitland, Porous media properties of reticulated shape memory polymer foams and mock embolic coils for aneurysm treatment, *Biomedical engineering online*, *12*, 103, 2013.
- Nair, P., B. Chong, A. Indahlastari, J. Ryan, C. Workman, M. H. Babiker, H. Y. F. Hooman, C. Baccin, and D. Frakes, Hemodynamic Characterization of Geometric Cerebral Aneurysm Templates Treated With Embolic Coils, *Journal of Biomechanical Engineering*, *138*(2), 2016.
- Ochoa-Tapia, J., and S. Whitaker, Momentum transfer at the boundary between a porous medium and a homogeneous fluid—i. theoretical development, *International Journal of Heat and Mass Transfer*, *38*(14), 2635–2646, 1995.
- Perrone, R. D., A. M. Malek, and T. Watnick, Vascular complications in autosomal dominant polycystic kidney disease, *Nature Reviews Nephrology*, *11*(10), 589–98, 2015.
- Piotin, M., L. Spelle, C. Mounayer, M. S.-R. D. Giansante-Abud, R. Vanzin-Santos, and J. Moret, Intracranial aneurysms: treatment with bare platinum coils—aneurysm packing, complex coils, and angiographic recurrence, *Radiology*, *243*(2), 500–8, 2007.
- Rosenzweig, R., and U. Shavit, The laminar flow field at the interface of a Sierpinski carpet configuration, *Water Resour. Res*, *43*, 2007.

- Rybak, I., *Mathematical modeling of coupled free flow and porous medium systems*, 2016.
- Saffman, P. G., On the boundary condition at the surface of a porous medium, *Stud. Appl. Math.*, 50, 93–101, 1971.
- Sanchez, M., D. Ambard, V. Costalat, S. Mendez, F. Jourdan, and F. Nicoud, Biomechanical assessment of the individual risk of rupture of cerebral aneurysms: A proof of concept., *Ann Biomed Eng*, 41, 28–40, 2013.
- Satoh, K., S. Matsubara, H. Hondoh, and S. Nagahiro, Intracranial Aneurysm Embolization Using Interlocking Detachable Coils. Correlation between Volume Embolization Rate and Coil Compaction. Correlation between Volume Embolization Rate and Coil Compaction, *Interv Neuroradiol*, 3(2), 125–8, 1997.
- Schievink, W., Intracranial aneurysms, *N Engl J Med.*, 336(1), 28–40, 1997.
- Schindelin, J., I. Arganda-Carreras, E. Frise, V. Kaynig, M. Longair, T. Pietzsch, and A. Cardona, Fiji: an open-source platform for biological-image analysis, *Nature Methods*, 9(7), 676–82, 2012.
- Seibert, B., R. Tumala, R. Chow, A. Farida, S. Mousavi, and A. Divani, Intracranial aneurysms: review of current treatment options and outcomes, *Front Neurol.*, 2011(12), 2:45, 2011.
- Sforza, D., C. Putman, and J. Cebral, Hemodynamics of Cerebral Aneurysms, *Annu Rev Fluid Mech*, 41, 91–107, 2009.
- Skjetne, E., and J.-L. Auriault, New Insights on Steady, Non-Linear Flow in Porous Media, *Eur. J. Mech. B/Fluids*, 18, 131–5, 1999.
- Sluzewski, M., W. van Rooij, M. S. J. Bescós, C. Slump, and D. Wijnalda, Relation between aneurysm volume, packing, and compaction in 145 cerebral aneurysms treated with coils, *Radiology*, 231(3), 653–8, 2004.
- Tamatani, S., Y. Ito, H. A. T. K. S. Takeuchi, and R. Tanaka, Evaluation of the stability of aneurysms after embolization using detachable coils: correlation between stability of aneurysms and embolized volume of aneurysms, *AJNR Am J Neuroradiol*, 23(5), 762–7, 2002.
- Tamayol, A., K. .Wong, and M. Bahrami, Effects of microstructure on flow properties of fibrous porous media at moderate reynolds number, *Phys. Rev. E*, 85, 026,318, 2012.

- Valen-Sendstad, K., and D. Steinman, Mind the gap: impact of computational fluid dynamics solution strategy on prediction of intracranial aneurysm hemodynamics and rupture status indicators, *AJNR Am J Neuroradiol*, *35*(3), 536–43, 2014.
- Venkat, K., M. Levitt, A. Clark, S. R. du Roscoat, L. Kim, and A. Aliseda, Reconstructing patient-specific cerebral aneurysm vasculature for in vitro investigations and treatment efficacy assessments, *Journal of Clinical Neuroscience*, *61*, 153–59, 2019.
- Venugopal, P., D. Valentino, H. Schmitt, J. P. Villablanca, F. Viñuela, and G. Duckwiler, Sensitivity of patient-specific numerical simulation of cerebral aneurysm hemodynamics to inflow boundary conditions , *Journal of Neurosurgery*, *106*(6), 1051—1060, 2007.
- Vlak, M., A. Algra, R. Brandenburg, and G. Rinkel, Prevalence of unruptured intracranial aneurysms, with emphasis on sex, age, comorbidity, country, and time period: a systematic review and meta-analysis, *Lancet Neurol.*, *10*(7), 626–36, 2011.
- Wilm, J., Iterative closest point, matlab central file exchange, 2020.
- Womersley, J., Method for the calculation of velocity, rate of flow and viscous drag in arteries when the pressure gradient is known, *J Physiol*, *127*(3), 553–63, 1955.
- Wootton, D., and D. Ku, Fluid mechanics of vascular systems, diseases, and thrombosis, *Annu Rev Biomed Eng*, *1*, 299–329, 1999.
- Yadollahi-Farsani, H., M. Herrmann, D. Frakes, and et al., A New Method for Simulating Embolic Coils as Heterogeneous Porous Media, *Cardiovasc Eng Tech*, *10*, 32—45, 2019.
- Zaripov, S., R. Mardanov, and V. Sharafutdinov, Determination of Brinkman Model Parameters Using Stokes Flow Model , *Transport in Porous Media volume*, *130*, 529–557, 2019.